

Incorporating unsteady flow-field effects in flamelet-generated manifolds

Citation for published version (APA):

Delhaye, S. (2009). *Incorporating unsteady flow-field effects in flamelet-generated manifolds*. [Phd Thesis 1 (Research TU/e / Graduation TU/e), Mechanical Engineering]. Technische Universiteit Eindhoven.
<https://doi.org/10.6100/IR642962>

DOI:

[10.6100/IR642962](https://doi.org/10.6100/IR642962)

Document status and date:

Published: 01/01/2009

Document Version:

Publisher's PDF, also known as Version of Record (includes final page, issue and volume numbers)

Please check the document version of this publication:

- A submitted manuscript is the version of the article upon submission and before peer-review. There can be important differences between the submitted version and the official published version of record. People interested in the research are advised to contact the author for the final version of the publication, or visit the DOI to the publisher's website.
- The final author version and the galley proof are versions of the publication after peer review.
- The final published version features the final layout of the paper including the volume, issue and page numbers.

[Link to publication](#)

General rights

Copyright and moral rights for the publications made accessible in the public portal are retained by the authors and/or other copyright owners and it is a condition of accessing publications that users recognise and abide by the legal requirements associated with these rights.

- Users may download and print one copy of any publication from the public portal for the purpose of private study or research.
- You may not further distribute the material or use it for any profit-making activity or commercial gain
- You may freely distribute the URL identifying the publication in the public portal.

If the publication is distributed under the terms of Article 25fa of the Dutch Copyright Act, indicated by the "Taverne" license above, please follow below link for the End User Agreement:

www.tue.nl/taverne

Take down policy

If you believe that this document breaches copyright please contact us at:

openaccess@tue.nl

providing details and we will investigate your claim.

Incorporating unsteady flow-field effects in Flamelet-Generated Manifolds

PROEFSCHRIFT

ter verkrijging van de graad van doctor aan de
Technische Universiteit Eindhoven, op gezag van de
rector magnificus, prof.dr.ir. C.J. van Duijn, voor een
commissie aangewezen door het College voor
Promoties in het openbaar te verdedigen
op dinsdag 16 juni 2009 om 16.00 uur

door

Stanley Delhaye

geboren te Helmond

Dit proefschrift is goedgekeurd door de promotor:

prof.dr. L.P.H. de Goeij

Copromotoren:

dr.ir. J.A. van Oijen

en

dr.ir. L.M.T. Somers

Copyright © 2009 by S. Delhaye

All rights reserved. No part of this publication may be reproduced, stored in a retrieval system, or transmitted, in any form, or by any means, electronic, mechanical, photocopying, recording, or otherwise, without the prior permission of the author.

Delhaye, Stanley

Incorporating unsteady flow-field effects in Flamelet-Generated Manifolds /
by Stanley Delhaye. - Eindhoven: Technische Universiteit Eindhoven, 2009
A catalogue record is available from the Eindhoven University of Technology Library
Proefschrift. - ISBN: 978-90-386-1876-0
NUR 978

Reproduction: University Press Facilities, Eindhoven, The Netherlands
Cover design: Stanley Delhaye

Subject headings: combustion modeling / reduced chemistry / Flamelet-Generated Manifolds /
flamelets / premixed flamelets / non-premixed flamelets / steady flamelets / unsteady flamelets
/ oscillating strain-rate

Contents

Summary	ix
Samenvatting	xi
1 Introduction	1
1.1 General introduction	1
1.1.1 Historical background	3
1.1.2 Introduction to combustion	4
1.2 Mathematical combustion model	5
1.2.1 Conservation laws	6
1.2.2 State equations	7
1.2.3 Transport and chemistry models	8
1.2.4 Combustion equations	11
1.3 Reduction of computational demand	11
1.4 Purpose of this study	14
1.5 Outline of this thesis	15

2	Towards a Unified Flamelet-Generated Manifolds Approach	17
2.1	Unified flamelet model	20
2.1.1	Flame front dynamics	20
2.1.2	Internal flame dynamics	23
2.2	Flamelet-Generated Manifolds	29
2.2.1	Flame front and internal flame structure (de)coupling	30
2.2.2	Generating manifolds	36
2.3	Concluding remarks	40
3	Numerical evaluation of the flamelet assumptions	41
3.1	Postprocessing procedure	42
3.2	Numerical simulations	45
3.2.1	Freely expanding two-dimensional premixed flame	45
3.2.2	Non-premixed reacting mixing Layer	51
3.2.3	Steady non-premixed co-flow flame	54
3.3	Discussion and conclusions	58
4	Incorporating unsteady flow-effects in Flamelet-Generated Manifolds	63
4.1	Introduction	63
4.2	Governing equations	65
4.3	Steady flamelet simulations	67
4.3.1	Application of a 2D manifold	68
4.4	Unsteady flamelet simulations	68
4.4.1	Manifold dimensional analysis	70
4.4.2	Application of a 3D manifold	72
4.4.3	Results and discussion	76
4.5	Conclusions	76

5	Incorporating extinction and re-ignition in Flamelet-Generated Manifolds	79
5.1	Introduction	80
5.2	Governing equations	80
5.3	Flamelet-Generated Manifolds construction	82
5.3.1	Constructing a 2D FGM beyond the steady extinction limit	82
5.3.2	Constructing a 3D FGM	83
5.4	FGM application and discussion	87
5.4.1	Prediction of species with slow chemical time-scales	89
5.5	Conclusions	90
6	Concluding remarks	93
A	Transformation relations	97
A.1	Covariant and contravariant base	97
A.1.1	Line increment	99
A.1.2	Surface increment	100
A.1.3	Volume increment	101
A.2	Differential operators in a generalized curvilinear space	102
A.2.1	Time derivative	103
A.2.2	Relation between covariant and contravariant basis vectors	105
A.2.3	Derivative operators	106
B	Physical interpretation of the mass consumption rate	107
C	Individual contributions of the species conservation equation	109
D	Non-premixed reacting mixing Layer - simulation and reaction rate parameters	113
	References	115
	Dankwoord	123
	Curriculum Vitae	125

Summary

Incorporating Unsteady Flow-Field Effects in Flamelet-Generated Manifolds

In general, simulating combustion can be a very costly job. This is caused by the large number of chemical reacting species that are strongly coupled. Moreover, all the (chemical) time-scales that are present, span a multitude of orders, which results in a very large, stiff system of strongly coupled, nonlinear equations and solving such a system is very CPU-intensive. Fortunately, it appears that many combustion systems are dominated by a handful of (slow) processes only. This is due to the fact that the fastest processes rapidly become exhausted and therefore are often neglected. This has subsequently led to a number of reduction techniques that take advantage of the observation that combustion can often be predicted reasonably accurate by taking only a small number of time-scales into account.

In this thesis a reduction technique that was introduced by van Oijen [61], i.e., Flamelet-Generated Manifolds (FGM), is expanded upon. The main goal of this thesis is to study whether unsteady flow effects can be captured within the Flamelet-Generated Manifolds concept. The flames that are studied are one-dimensional, non-premixed, stagnation flames and although FGM was initially developed for and successfully applied to premixed flames but in principle it can also be applied to non-premixed flames. To that end, first a **unified** one-dimensional flame model is presented, which can be used to describe (partially) premixed and non-premixed flames. Such a one-dimensional flame model is often referred to as flamelet model. The first step is to decompose the combustion process into three distinct sub-problems, i.e., 1) fluid motion and mixing of enthalpy and elements, 2) the flame front dynamics and 3) the dynamics of the internal flame structure embedded within this flame front. When flames are considered, it is often useful to use a so-called flame adapted coordinate system, where coordinate surfaces correspond to flame surfaces. The flame front dynamics can be described by the evolution of these flame surfaces, which correspond to iso-surfaces of a so-called principal controlling

variable \mathcal{Y} , for which a conservation equation can be solved. Applying such a coordinate transformation, leads to a set of quasi-one-dimensional combustion equations, which serve as the basis of the FGM method.

Generally it is assumed that perturbations from one-dimensional flame behavior are small, and can therefore be neglected. In order to numerically assess these assumptions, the species conservation equation is subdivided into several individual contributions, i.e., an unsteady term, normal transport, flame stretch, curvature, tangential diffusion and the chemical production and consumption terms, respectively. Three different two-dimensional flames are simulated, one unsteady premixed flame, one unsteady non-premixed flame and one steady non-premixed flame. Using the numerical results from these detailed flame simulations, the individual contributions of the species conservation equations are computed and compared to each other. The results show that besides normal transport and chemistry, flame stretch rate and curvature can also be important in both premixed and non-premixed flame simulations. From the two unsteady flame simulations it also follows that the unsteady contribution can be significant. Furthermore, for the steady non-premixed flame, two different principal controlling variables were chosen, resulting in two different coordinate transformations, i.e., a typical non-premixed flame-adapted coordinate system and a typical premixed one. This is possible due to the fact that the flamelet model derived in this thesis is a **unified** flamelet model, which is able to describe both (partially) premixed flames as well as non-premixed flames.

To study whether the effect of transient, local flow fluctuations can be captured by the FGM approach, both steady and unsteady non-premixed flamelet simulations with a detailed chemistry model are studied. Two different situations are studied, 1) a flame which is significantly strained but still far away from the steady extinction limit and 2) a flame where the applied strain-rate is near or even beyond the steady extinction limit. For both situations, two different Flamelet-Generated Manifolds are constructed, i.e., one based on a set steady flamelet simulations and one based on a set of unsteady flamelet simulations. The chemical compositions found during the steady flamelet simulations form a two-dimensional manifold in composition space. On the other hand, a detailed analysis of the chemical compositions found during the unsteady flamelet simulations shows that the unsteady flamelet simulations form a three-dimensional manifold in composition space. Both manifolds are applied to simulate one-dimensional flames that are subjected to sinusoidally varying strain-rate. The results of both FGM simulations are compared to an unsteady simulation with a detailed chemistry model. Both local observables, like species mass fractions and temperature for example, as well as flame-surface area properties like the integral source-term, are represented well with both manifolds. However, for species that are related to the slowest time-scales it is shown that a three-dimensional manifold may result in less accurate predictions, and more controlling variables may be needed.

Samenvatting

Incorporating Unsteady Flow-Field Effects in Flamelet-Generated Manifolds

In het algemeen kan geconcludeerd worden dat het numeriek simuleren van een verbrandingsproces een kostbare aangelegenheid kan zijn. Dit wordt veroorzaakt door het grote aantal chemisch reagerende stoffen die ook nog eens sterk afhankelijk van elkaar zijn. Wat de zaak nog verder compliceert, is dat de aanwezige (chemische) tijd-schalen zeer sterk uiteen loopt, wat uiteindelijk leidt tot een zeer groot, stijf systeem van niet-lineaire behoudsvergelijkingen die sterk gekoppeld zijn en het oplossen van dit systeem vraagt een grote hoeveelheid aan rekenkracht. Gelukkig blijkt dat in veel gevallen een verbrandingsproces wordt gedomineerd door slechts een klein aantal (langzame) processen. Dit komt doordat de snelste processen snel uitgedempt raken en daardoor verwaarloosd kunnen worden. Dit gegeven heeft geleid tot een aantal zogenoemde reductie technieken die gebruik maken van de vaststelling dat een verbrandingsproces vaak ook redelijk nauwkeurig kan worden voorspeld door slechts een klein aantal tijd-schalen te beschouwen.

In dit proefschrift wordt de reductie techniek die door van Oijen [61] is geïntroduceerd, de Flamelet-Generated Manifolds methode (FGM), verder uitgebreid. Het hoofddoel van dit werk is dan ook om te achterhalen of de FGM methode in staat is om tijdsafhankelijke processen te representeren. De vlammen die hiervoor worden bestudeerd zijn eendimensionale, niet-voorgemengde stagnatie vlammen en ondanks het feit dat FGM in eerste instantie is ontwikkeld voor, en met succes is toegepast op voorgemengde vlammen, is het in principe net zo goed mogelijk om dit te doen voor niet-voorgemengde vlammen. Daartoe wordt eerst een **unified** (verenigd) eendimensionaal vlam model geïntroduceerd (*flamelet model*), wat in staat is om zowel (deels) voorgemengde als niet-voorgemengde vlammen kan beschrijven. Het verbrandingsproces wordt eerst in drie sub-problemen opgedeeld, 1) de beweging van de gassen en het mengen van enthalpie en elementen, 2) de dynamica van het vlam front en 3) de dynamica van

de interne vlam structuur. Wanneer men vlammen beschouwt is het vaak nuttig om een vlam-georiënteerd coördinatenstelsel te hanteren. De dynamica van het vlam front kan vervolgens worden beschreven door de evolutie van een zogeheten primaire controle-variabele, \mathcal{Y} , waarvoor een behoudsvergelijking kan worden opgelost. Door een coördinaten-transformatie toe te passen waarbij het Cartesische coördinatenstelsel wordt vervangen door een vlam-georiënteerd coördinatenstelsel kan uiteindelijk een quasi-eendimensionaal stelsel van verbrandingsvergelijkingen worden afgeleid, wat weer als basis dient voor de FGM methode.

Vaak wordt aangenomen dat afwijkingen van eendimensionaal vlamgedrag klein zijn en dus mogen worden verwaarloosd. Om dit numeriek te valideren, wordt de behoudsvergelijking voor chemische stofjes opgedeeld in een aantal individuele bijdragen, een tijdsafhankelijke term, *normal transport* (transport loodrecht op de vlamvlakken), *flame stretch* (vlamrek), *curvature* (kromming van de vlam), *tangential diffusion* (diffusie evenwijdig aan de vlamvlakken) en een chemische productie en consumptie term. Aan de hand van drie verschillende tweedimensionale vlam simulaties, een tijdsafhankelijke voorgemengde vlam, een tijdsafhankelijke niet-voorgemengde vlam en een stationaire niet-voorgemengde vlam. Aan de hand van de resultaten van de numerieke vlam simulaties, worden de individuele bijdragen van de behoudsvergelijking voor chemische stofjes berekend en met elkaar vergeleken. Uit de resultaten blijkt dat naast *normal transport* en chemische bron-termen ook *flame stretch* en *curvature* een aanzienlijke bijdrage leveren in zowel de voorgemengde als de niet-voorgemengde vlam simulaties. De twee tijdsafhankelijke vlam simulaties laten verder zien dat ook transiënte effecten belangrijk kunnen zijn. Voor de stationaire niet-voorgemengde vlam zijn twee verschillende coördinaten transformaties toegepast, één die leidt tot een typisch niet-voorgemengd vlam-georiënteerd coördinatenstelsel en één die leidt tot een typisch voorgemengd vlam-georiënteerd coördinatenstelsel. Het feit dat dit mogelijk is komt door het **unified** karakter van het eendimensionaal vlam model, waarmee zowel (deels) voorgemengde als niet-voorgemengde vlammen kunnen worden beschreven.

Om te bestuderen of het mogelijk is om transiënte, locale stromingsfluctuaties te beschrijven met behulp van de FGM methode, worden zowel stationaire als niet-stationaire niet-voorgemengde vlam simulaties bestudeerd. De chemie van deze vlam simulaties wordt beschreven door een gedetailleerd chemie model. Twee verschillende situaties worden beschouwd, 1) een vlam waarbij de *applied strain-rate* (toegepaste rek) aanzienlijk is, maar nog lang niet in de buurt ligt van de zogenaamde *steady extinction limit* (stationaire uitdoof-limiet) en 2) een vlam waarbij de *applied strain-rate* de *steady extinction limit* nadert of zelfs overschrijdt. Voor beide situaties worden twee verschillende Flamelet-Generated Manifolds gegenereerd, een gebaseerd op een serie stationaire *flamelet* simulaties en een gebaseerd op een serie niet-stationaire *flamelet* simulaties. Het blijkt dat de chemische composities die tijdens de stationaire *flamelet* simulaties gevonden

worden een tweedimensionale subruimte ofwel manifold vormen in de zogeheten compositie-ruimte. Voor de chemische composities die tijdens de niet-stationaire *flamelet* simulaties worden gevonden, wordt met behulp van een gedetailleerde analyse aangetoond dat deze simulaties een driedimensionaal manifold vormen in de compositie-ruimte. Beide manifolds zijn vervolgens toegepast om eendimensionale vlammen te simuleren die onderhevig zijn aan een *applied strain-rate* die als een sinus-functie toe- en afneemt. De resultaten van de beide FGM simulaties worden vergeleken met een niet-stationaire simulatie waarbij een gedetailleerd chemie model gebruikt is. Zowel locale variabelen, zoals chemische stofjes en de temperatuur bijvoorbeeld, als geïntegreerde grootheden zoals de integrale chemische bron-term worden goed voorspeld door beide manifolds. Echter, voor chemische stofjes met een lange tijd-schaal, wordt aangetoond dat een driedimensionaal manifold tot minder nauwkeurige resultaten leidt. Het toevoegen van één extra controle-variabele zou kunnen leiden tot een aanzienlijke verbetering van de resultaten.

Stephen King's answer to the question: "How do you write?"

CHAPTER ONE

Introduction

This first chapter serves as an introduction to the topic of this thesis, which is the analysis and application of Flamelet-Generated Manifolds for (unsteady) non-premixed flames. First, in the general introduction it is explained why it is important to reduce the computational effort when simulating combustion systems. Furthermore, a short historical overview of combustion research is presented, followed by an introduction to combustion where some aspects like premixed and non-premixed combustion will be highlighted. Subsequently, the model which is used to mathematically describe combustion is presented. Also a short summary to the various reduction techniques is given, which subsequently leads to the purpose of this thesis; study whether the Flamelet-Generated Manifolds method can be extended to incorporate unsteady flow effects for non-premixed flames.

1.1 General introduction

Nowadays, more so than ever perhaps, there is a growing gap between the energy our society demands and the geological and environmental impact that generating this energy has. While durable solutions become increasingly important to our energy dilemma, combustion still remains essential when it comes to power-generating [36]. Figure 1.1 shows the most 'sustainable' scenario concerning energy production as estimated by the World Energy Council. It is clear that sustainable energy sources will not be sufficient to reduce or even eliminate the necessity to use fossil fuels in the coming decades.

Two of the major problems that are closely linked to combustion are the ever diminishing availability of fossil fuels and pollution due to harmful emissions. It goes without saying that these problems have a high priority to be solved, or at least reduce their impact. By introducing legislation that gets progressively more strict, governments and companies are obliged by law to reduce the emissions caused by combustion. An example of such legislation is the European Emission Standard. Because of this, it is very important that both the efficiency as well as the amount of pollutants that is produced during a combustion process, can be accurately predicted. This can be done both experimentally

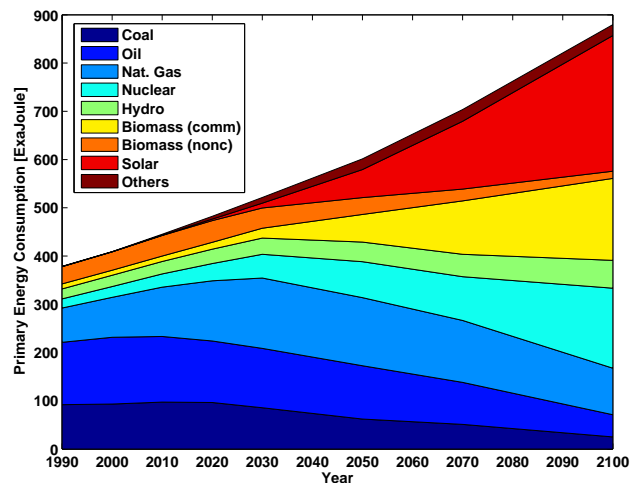


Figure 1.1: The most ‘sustainable’ energy scenario [36].

as well as numerically, where the latter has the major advantage that it is more flexible and is generally also cheaper.

Since combustion was first studied in the 17th century, our knowledge of the underlying physics and chemistry has increased enormously. This has resulted in complex combustion models, and although the CPU power has increased immensely in the last few decades and will probably continue to do so [59], the computational demand will probably remain very high. This is partly caused by the fact that there are a lot of species, and often even more chemical reactions involved. This results in a very large system of tightly coupled, non-linear partial differential equations. Another aspect that makes the computations very expensive is the fact that most combustion processes are characterized by a vast range of time-scales, which results in a very stiff system.

Fortunately, it has been observed that many time-scales associated with chemical reactions are much faster than the flow time-scales, i.e., most of the chemical time-scales are much smaller than the physical time-scales. This means that during a combustion process, a large portion of the chemical species can be assumed to be in steady state, in other words, the majority of a combustion process is dominated by a small number of time-scales [52,70,86]. These assumptions are the basis for a class of reduction techniques that are commonly known as chemical reduction techniques. Based on a chemical time-scale analysis, species are ranked from small time-scales to long time-scales, where the species associated with the smallest time-scales are assumed to be in steady state. These steady state relations describe a low-dimensional manifold in the so-called state-space, which can be characterized with (linear combinations of) species mass-fractions.

Another popular method that is commonly used to reduce the computational effort are the so-called flamelet models. Flamelet models are based on the assumption that changes along a flame are much smaller than changes perpendicular to a flame [71]. This assumption consequently leads to a quasi one-dimensional description of the flame structure. Because transport processes are also taken into account, flamelet models tend to be more accurate in the colder regions of a flame than chemical reduction techniques.

This is caused by the fact that at lower temperatures, most of the chemical time-scales become of the same order as the physical time-scales. Hence, a much smaller group of species can be assumed to be in steady state. One of the drawbacks of flamelet models compared to the chemical reduction techniques, is that it is not trivial to increase the accuracy by taking more time-scales into account. This is due to the fact that generally, flamelets are parameterized by the mixture fraction Z and the so-called scalar dissipation rate χ and increasing the dimension of the flamelet table is not straightforward.

Flamelet based manifolds, i.e., Flamelet-Generated Manifolds [61] (FGM) and Flame-Prolongation of ILDM [32] (FPI) can be considered as a combination between chemical reduction techniques and the laminar flamelet approach. Generally, one-dimensional flamelets are simulated and their structure is stored in a flamelet database. Like the chemical reduction techniques, (linear combinations of) species mass-fractions are used to characterize the local flame composition, which means that it is easier to take more time-scales into account than is the case with flamelet models.

Although FGM was initially developed for premixed flames [61], there is no reason to assume that it does not work for non-premixed flames. Therefore, in this work it will be shown that the FGM method can also be applied to partially premixed and non-premixed flames. Furthermore, all three types of flames will be incorporated into the FGM framework in a **unified** approach.

1.1.1 Historical background

Although fire has been known to mankind since prehistoric times, scientific research of combustion is still fairly young. Where the early days of combustion research were of a more philosophical nature and many phenomena were studied qualitatively, nowadays a deep understanding exists to the nature of the many different aspects of combustion. Nevertheless, we are still far from a total understanding.

It was the Flemish physician Johann Baptista van Helmont (1580 - 1644) who observed that there was a direct link between a burning material and the presence of a flame and smoke. He reasoned that this process involved the escape of what he called a "spiritus silvestre", which means wild spirit. This idea was incorporated in the so-called phlogiston theory by Johann Joachim Becher (1635 - 1682) and Georg Ernst Stahl (1660 - 1734). It was believed that all combustible materials contain a certain amount of phlogiston, which is an invisible substance that has no odor, no color, no taste and no mass. Any material that is still combustible was called "phlogisticated", whereas burnt substances were called "dephlogisticated". In this theory, air played a very important role; it was thought that air had the ability to absorb only a limited amount of phlogiston that was released by a combusting substance. When the surrounding air was completely phlogisticated, a flame would extinguish because the air was saturated with phlogiston. Initially, phlogiston was conceived as a sort of anti-oxygen, and although the importance of air was already included in this theory, it has been discarded. It was Antoine Laurent Lavoisier (1743 - 1794) who discovered that it was in fact the oxygen present in air that is essential to any combustion process. According to Lavoisier, combustion is the process by which a material combines with oxygen. Together with Pierre Simon Laplace (1749 - 1827),

Lavoisier made another very important breakthrough regarding combustion. The two men discovered that the amount of heat needed to break down the molecules is the same as the amount of heat that is liberated, which was called the heat of combustion.

During the last hundred years, the nature of scientific research to combustion phenomena changed due to the emergence of modern computers. It became possible to not only study combustion experimentally or analytically, but also numerically. Modern computers have enabled (combustion) researchers to develop more detailed models, leading to a much deeper understanding of the physics and chemistry that play a role in combustion. However, the (chemical) models have also become increasingly complex, which means that applying complex combustion models to practical combustion systems is still not realistic. Therefore, much attention is given in reducing the complexity of the chemical models while retaining the accuracy. Before briefly discussing the various reduction methods, a general introduction to combustion will be given below.

1.1.2 Introduction to combustion

Combustion can be regarded as a self sustaining oxidative chemical reaction that is characterized by a thermal runaway. In its most simple form, combustion can be described as a one-step global reaction, which reads:



In reality it is not just one single chemical reaction that occurs, but there are a lot of elementary chemical reactions that take place (almost) simultaneously. All these elementary reactions have their own reaction rate, which are highly non-linear functions in temperature and species concentration and can differ in magnitude immensely from one elementary reaction to the other. As a result, a combustion process contains a huge range of both chemical and physical time-scales. From a computational point of view this means that a very large and stiff set of equations has to be solved and with current technology this is not feasible for practical combustion problems.

Depending on the initial state of the mixing of fuel and oxidizer, a combustion process can either be identified as (partially) premixed or non-premixed. In premixed combustion, the unburnt gas is already mixed on the molecular level, which means that chemical reactions can take place directly and the reaction progress is not inhibited by molecular mixing processes. The rate of reaction is only limited by the chemical kinetics of the reactions involved and heat diffusion towards the unburnt mixture. In non-premixed combustion however, the fuel and oxidizer are not yet mixed, and diffusion and mixing of fuel with the oxidizer is the limiting process.

In figure 1.2 (l) a typical structure of a computed, one-dimensional premixed flame can be seen. Note that only a few species are shown. The unburnt mixture containing both fuel and oxidizer, is present in a large amount at the left side of the flame, and is consumed at the flame front. The combustion products, consisting of CO_2 and H_2O amongst others, are produced at the flame front, while the intermediate species are produced and consumed very fast near the flame front. In this figure one of the intermediates, OH, is shown. Because the mass fraction for OH is very small, it is scaled with $0.25 \times Y_{\text{OH,max}}$

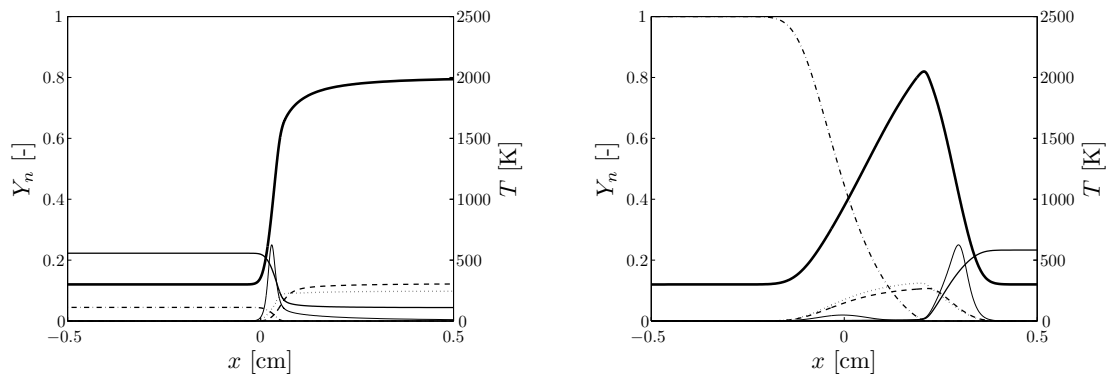


Figure 1.2: The internal structure of a premixed flame (l) and a non-premixed counterflow flame (r). Shown are the mass fractions of O_2 (solid line), CH_4 (dash-dotted line), H_2O (dotted line), CO_2 (dashed line) and OH , which has been scaled with $10 \times Y_{OH,max}$ (l) and $2.5 \times Y_{OH,max}$ (r) for visualization purposes. Also shown is the temperature (thick solid line).

for convenience. The temperature T rises from its initial value at the unburnt side of the flame to its maximum value at the burnt side.

Figure 1.2 (r) shows a typical structure of a computed, one-dimensional, non-premixed counterflow flame. Combustion can only take place when mixing on a molecular scale is accomplished. As can be seen, both the fuel and the oxidizer are consumed at the flame front, while products like CO_2 and H_2O are produced there. The intermediate species, of which OH is one, are produced and consumed at the flame front. Here, the mass fraction for OH is again scaled with $0.25 \times Y_{OH,max}$. The temperature T reaches its maximum value at the flame front, and decreases to both the fuel side and the oxidizer side due to diffusion.

A key difference between a premixed flame and a non-premixed flame, is that a premixed flame is self-propagating. This propagation velocity can be characterized by the so-called displacement speed S_d [26,27], which is an intrinsic property of a premixed combustion system. This displacement speed can be regarded as a relative displacement velocity, which indicates the velocity of the flame with respect to the unburnt gas velocity. Since non-premixed flames do not propagate into an 'unburnt' mixture as premixed flames do, it is not common to introduce such a displacement speed for non-premixed flames. However, in chapter 2 it will be argued why a relative displacement speed can also be defined for non-premixed flames. Furthermore, in Appendix B it will be explained how this relative displacement speed can be regarded for non-premixed flames.

1.2 Mathematical combustion model

Flames can be described as thin reactive-diffusive layers embedded within an otherwise non-reacting flow field. This non-reacting flow field is described by the conservation equations from fluid dynamics, i.e., conservation of mass, momentum and energy or enthalpy [46]. In addition, conservation equations for the chemical components are needed to describe the internal structure of a flame.

1.2.1 Conservation laws

In a chemically reacting flow, a mass balance equation for every species has to be solved:

$$\frac{\partial (\rho_n)}{\partial t} + \nabla \cdot (\rho_n \mathbf{u}_n) = \dot{\omega}_n, \quad n \in [1, N_s], \quad (1.2)$$

with ρ_n the mass density and \mathbf{u}_n the particular velocity of species n , respectively. The species source-term $\dot{\omega}_n$ describes the rate of change of the mass of species n due to chemical reactions. The particular velocity of species n can be defined as a combination of the \mathbf{u} and the diffusion velocity \mathbf{V}_n and can be written as $\mathbf{u}_n = \mathbf{u} + \mathbf{V}_n$, with $\mathbf{u} = (u_1, u_2, u_3)^T$. Furthermore, the species mass fraction is the ratio between the (specific) species mass and the total mass of the mixture:

$$Y_n = \frac{\rho_n}{\rho}, \quad n \in [1, N_s], \quad (1.3)$$

with ρ the mass density of the mixture. The mass density of the mixture is the sum of the mass densities of all species present in the mixture:

$$\sum_{n=1}^{N_s} \rho_n = \rho, \quad (1.4)$$

which means that $\sum_{n=1}^{N_s} Y_n = 1$. When the definition of \mathbf{u}_n is substituted in (1.2), and by using the definition of the mass fraction of each species (1.3), equation (1.2) can be written as:

$$\frac{\partial (\rho Y_n)}{\partial t} + \nabla \cdot (\rho \mathbf{u} Y_n) + \nabla \cdot (\rho \mathbf{V}_n Y_n) = \dot{\omega}_n, \quad n \in [1, N_s]. \quad (1.5)$$

In section 1.2.3 an approach to model the diffusion velocity \mathbf{V}_n will be introduced.

Another set of important conservation equations that needs to be considered for reactive flows, are the conservation equations for element mass fractions, which are defined as:

$$Z_j = \sum_{k=1}^{N_s} w_{jk} Y_k, \quad j \in [1, N_e], \quad (1.6)$$

where w_{jk} is defined as:

$$w_{jk} = \frac{a_{jk} M_j}{M_k}, \quad j \in [1, N_e], \quad k \in [1, N_s], \quad (1.7)$$

with a_{jk} the total number of chemical elements j in species k . Furthermore, M_j and M_k are the molar masses of element j and species k , respectively. Since elements cannot be created or annihilated by chemical reactions, element mass is conserved during chemical reactions. This implies

$$\sum_{k=1}^{N_s} w_{jk} \dot{\omega}_k = 0. \quad (1.8)$$

By taking the proper linear combination of (1.5), the conservation equations for element mass fractions can be derived:

$$\frac{\partial(\rho Z_j)}{\partial t} + \nabla \cdot (\rho \mathbf{u} Z_j) + \sum_{k=1}^{N_s} w_{jk} \nabla \cdot (\rho \mathbf{V}_k Y_k) = 0, \quad j \in [1, N_e]. \quad (1.9)$$

By taking the summation of equation (1.2) over all species one can ultimately derive the continuity equation:

$$\sum_{n=1}^{N_s} \frac{\partial(\rho_n)}{\partial t} + \sum_{n=1}^{N_s} \nabla \cdot (\rho_n \mathbf{u}_n) = \sum_{n=1}^{N_s} \dot{\omega}_n. \quad (1.10)$$

Considering that $\sum_{n=1}^{N_s} \rho_n \mathbf{u}_n = \rho \mathbf{u}$, which defines the average mixture velocity, and where ρ_n is defined by (1.4), leads to the conservation equation of mass for the mixture:

$$\frac{\partial \rho}{\partial t} + \nabla \cdot (\rho \mathbf{u}) = 0. \quad (1.11)$$

Note that (1.11) does not contain a chemical source-term, contrary to the conservation equation of species (1.5). This is of course due to the fact that chemical reactions cannot change the total mass of a reacting system.

In fluid dynamics, conservation of momentum is described by the Navier-Stokes equations [46]:

$$\frac{\partial(\rho \mathbf{u})}{\partial t} + \nabla \cdot (\rho \mathbf{u} \mathbf{u}) = \rho \mathbf{g} - \nabla \cdot \mathcal{P}, \quad (1.12)$$

where \mathbf{g} is the gravitational acceleration and \mathcal{P} is the stress tensor, which is defined as $\mathcal{P} = p\mathcal{I} - \boldsymbol{\tau}$. Furthermore, p is the hydrostatic pressure, $\boldsymbol{\tau}$ is the viscous stress tensor, and \mathcal{I} the unit tensor.

And finally, conservation of enthalpy can be written as follows:

$$\frac{\partial(\rho h)}{\partial t} + \nabla \cdot (\rho \mathbf{u} h) = \rho \mathbf{u} \cdot \mathbf{g} - \nabla \cdot \mathbf{q} + \boldsymbol{\tau} : (\nabla \mathbf{u}) + \frac{Dp}{Dt}, \quad (1.13)$$

where h is the enthalpy density and \mathbf{q} is the heat flux. The last term on the right-hand-side is the material derivative for the pressure¹.

1.2.2 State equations

With the use of two state equations the pressure and enthalpy can be written as functions of the density, the temperature and the species mass fractions. For the pressure, the thermal equation of state will be used and for the enthalpy, the caloric equation of state.

¹The material derivative of the pressure is given by:

$$\frac{Dp}{Dt} = \frac{\partial p}{\partial t} + \mathbf{u} \cdot \nabla p.$$

In most common combustion problems the gas mixture and its components are assumed to behave as perfect gasses. The thermal equation of state is then given by the ideal gas law, which is a relation between the pressure, the density, the temperature and the species mass fractions. The ideal gas law for the pressure for each species p_k is given by:

$$p_k = n_k RT = n X_k RT, \quad k \in [1, N_s], \quad (1.14)$$

where R is the universal gas constant and $X_k = n_k/n$ the species mole fraction, with n_k the molar concentration of species k and n the molar concentration of the total gas mixture. The species mole fraction is related to the species mass fraction as follows:

$$X_k = Y_k \frac{\bar{M}}{M_k}, \quad k \in [1, N_s], \quad (1.15)$$

with M_k the molar mass of species k and \bar{M} the mean molar mass. When $\rho = n\bar{M}$ is used in combination with (1.15), equation (1.14) becomes:

$$p_k = \rho RT \frac{Y_k}{M_k}, \quad k \in [1, N_s]. \quad (1.16)$$

The sum of all the partial pressures p_k is equal to the hydrostatic pressure according to:

$$p = \sum_{k=1}^{N_s} p_k = \rho RT \sum_{k=1}^{N_s} \frac{Y_k}{M_k}. \quad (1.17)$$

The enthalpy density is related to the temperature T and the species mass fractions Y_k by the caloric equation of state as follows:

$$h = \sum_{k=1}^{N_s} Y_k h_k, \quad (1.18)$$

where h_k is the enthalpy density of species k . The enthalpy density of species k is related to the formation enthalpy at a certain reference temperature T^* :

$$h_k = h_k^* + \int_{T^*}^T c_{p_k}(T) dT, \quad k \in [1, N_s], \quad (1.19)$$

with h_k^* the species enthalpy density of formation at a certain reference temperature T^* and c_{p_k} the specific heat of species k at constant pressure, which is well tabulated in polynomial form [42].

1.2.3 Transport and chemistry models

In this section the transport models for the diffusion velocity, the viscous stress tensor and the heat-flux are presented. Furthermore a model to calculate the chemical source-terms is presented.

Transport models

The diffusion velocity field V_n can be solved by using the so-called Stefan-Maxwell equations [93]. When neglecting contributions caused by pressure and temperature

gradients, the equations that have to be solved, are:

$$\nabla X_n = \sum_{k=1}^{N_s} \frac{X_n X_k}{\mathcal{D}_{nk}} (\mathbf{V}_k - \mathbf{V}_n), \quad n \in [1, N_s], \quad (1.20)$$

with \mathcal{D}_{nk} the binary mass diffusion coefficient of species n into species k . Because the computational costs to solve equation (1.20) are very high, a model that is less complex will be used. This model is based on Fick's law and it is commonly used to model the diffusion velocities [54]. The diffusion velocities are defined as:

$$\mathbf{V}_n = -\frac{D_{nm}}{Y_n} \nabla Y_n, \quad n \in [1, N_s - 1], \quad (1.21)$$

where D_{nm} is the diffusion coefficient of species n into the mixture m , which can be related to the overall diffusion coefficient D as follows:

$$D_{nm} = \frac{D}{\text{Le}_n}, \quad (1.22)$$

with the overall diffusion coefficient:

$$D = \frac{\lambda}{\rho c_p}. \quad (1.23)$$

The Lewis number, which is the ratio of thermal conduction and species mass diffusion, is defined as:

$$\text{Le}_n = \frac{\lambda}{\rho D_{nm} c_p}, \quad n \in [1, N_s - 1] \quad (1.24)$$

where c_p is the specific heat at constant pressure and λ the heat conductivity. The ratio between the thermal conductivity and the heat capacity can be computed by using a simplified relation [85] that is dependent on the temperature only:

$$\frac{\lambda}{c_p} = 2.58 \times 10^{-5} \left(\frac{T}{298} \right)^{0.69} \quad [\text{kg m}^{-1} \text{s}^{-1}]. \quad (1.25)$$

Equation (1.21) assumes that there is an abundant species. Using (1.24), equation (1.21) becomes:

$$\mathbf{V}_n = -\frac{D}{\text{Le}_n Y_n} \nabla Y_n, \quad n \in [1, N_s - 1], \quad (1.26)$$

where it has been assumed that the Lewis numbers are constant through the flame. Equation (1.26) is the diffusion model that will be used throughout the remainder of this report. Using (1.26), equation (1.5) becomes:

$$\frac{\partial (\rho Y_n)}{\partial t} + \nabla \cdot (\rho \mathbf{u} Y_n) - \frac{1}{\text{Le}_n} \nabla \cdot (\rho D \nabla Y_n) = \dot{\omega}_n, \quad n \in [1, N_s - 1]. \quad (1.27)$$

The transport model for the heat flux \mathbf{q} , is given by [93]:

$$\mathbf{q} = -\lambda \nabla T + \sum_{k=1}^{N_s} \rho \mathbf{V}_k Y_k h_k, \quad (1.28)$$

The first term of (1.28) represents heat transport through conduction and the second term represents heat transport through mass diffusion. It can be shown [65] that equation (1.28) can also be written as:

$$\mathbf{q} = -\rho D \nabla h - \rho D \sum_{k=1}^{N_s} \left(\frac{1}{Le_k} - 1 \right) h_k \nabla Y_k. \quad (1.29)$$

When it is assumed that the gas mixture behaves as a Newtonian fluid, the viscous stress tensor $\boldsymbol{\tau}$ can be modeled with Stokes' law of friction, cf. [93]:

$$\boldsymbol{\tau} = \mu \left(\nabla \mathbf{u} + (\nabla \mathbf{u})^T - \frac{2}{3} (\nabla \cdot \mathbf{u}) \boldsymbol{\mathcal{I}} \right), \quad (1.30)$$

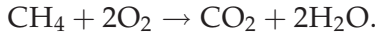
where μ is the dynamic viscosity of the mixture, which is related to the kinematic viscosity ν as $\mu = \rho \nu$. Using equation (1.29), the conservation equation for the enthalpy (1.13) becomes:

$$\frac{\partial (\rho h)}{\partial t} + \nabla \cdot (\rho \mathbf{u} h) - \nabla \cdot (\rho D \nabla h) = \sum_{k=1}^{N_s} \left(\frac{1}{Le_k} - 1 \right) \nabla \cdot (\rho D h_k \nabla Y_k), \quad (1.31)$$

where it has been assumed that effects caused by gravity, viscous stress and pressure can be neglected.

Chemistry model

As an example, for combustion of a methane-air flame, the global reaction can be written as:



On a molecular level, many elementary reactions take place. The general form that describes these elementary reactions is given by:

$$\sum_{n=1}^{N_s} \nu_{nl}' \frac{\rho Y_n}{M_n} \rightleftharpoons \sum_{n=1}^{N_s} \nu_{nl}'' \frac{\rho Y_n}{M_n}, \quad l \in [1, N_r], \quad (1.32)$$

where ν_{nl}' and ν_{nl}'' are the molar stoichiometric coefficients of species n in reaction l , and N_r is the number of reactions. The chemical source-term $\dot{\omega}_n$ for species n contains the contribution of all chemical reactions and is given by:

$$\dot{\omega}_n = M_n \sum_{l=1}^{N_r} (\nu_{nl}'' - \nu_{nl}') r_l, \quad n \in [1, N_s], \quad (1.33)$$

where the reaction rate r_l , is defined as:

$$r_l = k_1^f \prod_{n=1}^{N_s} \left(\frac{\rho Y_n}{M_n} \right)^{\nu_{nl}'} - k_1^b \prod_{n=1}^{N_s} \left(\frac{\rho Y_n}{M_n} \right)^{\nu_{nl}''}, \quad l \in [1, N_r], \quad (1.34)$$

where k_j is the reaction rate constant of reaction l , and the superscripts f and b refer to the forward and backward reactions. This leads to the following expression for the

chemical source-term:

$$\dot{\omega}_n = M_n \sum_{l=1}^{N_r} (\nu_{nl}'' - \nu_{nl}') \left\{ k_1^f \prod_{n=1}^{N_s} \left(\frac{\rho Y_n}{M_n} \right)^{\nu_{nl}'} - k_1^b \prod_{n=1}^{N_s} \left(\frac{\rho Y_n}{M_n} \right)^{\nu_{nl}''} \right\}, \quad n \in [1, N_s]. \quad (1.35)$$

For many fuels, the reactions and the reaction constants are listed in various reaction mechanisms. These reaction mechanisms range from simple one-step mechanisms [7, 53], to more complex reaction mechanisms [84, 85], to very large mechanisms containing hundreds of chemical reacting species and thousands of reactions [44, 82].

1.2.4 Combustion equations

Finally, the set of equations describing combustion processes and that is used in the remainder of this thesis is summarized. The combustion equations consist of the continuity equation, the Navier-Stokes equations accounting for conservation of momentum, conservation of enthalpy and conservation of species mass:

$$\frac{\partial \rho}{\partial t} + \nabla \cdot (\rho \mathbf{u}) = 0, \quad (1.36)$$

$$\frac{\partial (\rho \mathbf{u})}{\partial t} + \nabla \cdot (\rho \mathbf{u} \mathbf{u}) = -\nabla p + \nabla \cdot \boldsymbol{\tau}, \quad (1.37)$$

$$\frac{\partial (\rho Y_n)}{\partial t} + \nabla \cdot (\rho \mathbf{u} Y_n) - \nabla \cdot \left(\frac{\lambda}{\text{Le}_n c_p} \nabla Y_n \right) = \dot{\omega}_n, \quad n \in [1, N_s - 1], \quad (1.38)$$

$$\sum_{n=1}^{N_s} Y_n = 1, \quad (1.39)$$

and

$$\frac{\partial (\rho h)}{\partial t} + \nabla \cdot (\rho \mathbf{u} h) - \nabla \cdot (\rho D \nabla h) = \sum_{k=1}^{N_s} \left(\frac{1}{\text{Le}_k} - 1 \right) \nabla \cdot (\rho D h_k \nabla Y_k), \quad (1.40)$$

where radiation, as well as gravitational and external forces have been neglected.

1.3 Reduction of computational demand

When simulating combustion, the set of combustion equations (1.36)-(1.40) needs to be solved. The chemical reactions are modeled using (detailed) chemical mechanisms, which can contain many chemically reacting species, each associated with its own chemical time-scale. Because the species are dependent on each other in a highly non-linear fashion, this means that in general the set of combustion equations becomes very stiff. Solving

complex combustion problems using detailed chemical mechanisms is therefore very expensive. One way to cope with this is by simplifying the chemical model without losing too much accuracy.

During a combustion process there is generally a large number of chemical reactions involved, describing the (unsteady) conversion from one state of the system to another state. Each state of a system is fully determined by the state variables, i.e., the enthalpy h , the pressure p and the species mass fractions Y_n . This means that the state of a chemical system can be regarded as a single point in a N_{st} -dimensional state space. Here N_{st} is the number of variables that determine the state of a chemical reacting system, i.e., $N_{\text{st}} = N_s + 2$, with N_s the number of reacting species. Furthermore, the state space is a mathematical entity, where the basis vectors are spanned by the enthalpy h , the pressure p and the species mass fractions Y_n . Taking several restrictions into account, e.g., conservation of elements, no creation or annihilation of mass, the reaction trajectories are restricted onto an N_R -dimensional reaction space, where $N_R < N_{\text{st}}$. In principle, combustion can take place in the complete N_R -dimensional reaction space, however, it is observed that many of the chemical time-scales become quickly exhausted and the majority of the reaction trajectory can be described by a small number of slow processes. This observation has led to the assumption that a combustion process can also be accurately described by the slowest processes only, thereby neglecting the (very short) initial trajectories. The question is of course what are these slowest processes and how can they be identified? As is the case often in science, there is no single concluding answer, which has led to a number of successful approaches to reduce the computational demand, of which a select number will be discussed below.

The conventional reduction technique [70] employs partial-equilibrium and steady-state assumptions for certain reactions and species that are typically associated with the shortest, often chemical, time-scales. For a certain species n , a steady-state assumption simply states that all chemical reactions involving said species exactly balance, i.e., equation (1.33) equals zero for steady-state species:

$$\dot{\omega}_n = M_n \sum_{l=1}^{N_r} (\nu_{nl}'' - \nu_{nl}') r_l = 0, \quad n \in [1, N_{\text{ss}}], \quad (1.41)$$

where N_{ss} is the number of steady-state species. Note that this does not mean that there are no chemical reactions involved with steady-state species, but merely that species n is produced in exactly the same amount and exactly the same rate as it is consumed.

Assuming that the first N_{ss} species are in steady-state, the conservation equations for species (1.38) can be simply replaced by:

$$0 = \dot{\omega}_n, \quad n \in [1, N_{\text{ss}}], \quad (1.42)$$

$$\frac{\partial (\rho Y_n)}{\partial t} + \nabla \cdot (\rho \mathbf{u} Y_n) - \nabla \cdot \left(\frac{\lambda}{\text{Le}_n c_p} \nabla Y_n \right) = \dot{\omega}_n, \quad n \in [N_{\text{ss}} + 1, N_s]. \quad (1.43)$$

The advantage of using (1.42) and (1.43) is twofold; 1) the number of partial differential equations that needs to be solved is reduced, i.e., the conservation equations of the

steady-state species are replaced by N_{ss} algebraic equations and 2) the stiffness is greatly reduced, due to the fact that the fastest time-scales are removed from the combustion equations.

One difficulty remains however; the steady-state relations (1.41) form a set of non-linear, coupled algebraic equations and solving these is not trivial. This problem can be overcome by considering the largest terms in (1.41) only [70,86]. This way, the complexity can be further reduced and sometimes as a result, explicit relations for the steady-state species are obtained.

Choosing the steady-state species is done manually, which means that a deep insight in the chemical kinetics is required. Furthermore, applying the conventional reduction technique on simple chemical systems containing only a few reactive species may not be a problem, but for more complex chemical models containing hundreds of species and reactions, this becomes very difficult. Finally, the steady-state relations are assumed to be valid for the entire system, which is generally not the case.

In both the Computational Singular Perturbation (CSP) algorithm [47] as well as the Intrinsic Low-Dimensional Manifolds (ILDM) method [52], a time-scale analysis is performed automatically, based on the local Jacobi matrix of the chemical source-term. In the CSP method, introduced by Lam and Goussis [47], singular perturbation theory is applied to distinguish the slow from the fast processes, while in the ILDM method, introduced by Maas and Pope [52], the manifold is found by an eigenvalue decomposition of the chemical source-term. In both methods, only chemical time-scales are considered, which means that in for instance low-temperature areas, where transport plays an important role, it is expected that both CSP and ILDM will not yield accurate results.

In another very successful approach to reduce the computational effort, it is assumed that a flame can be described by an ensemble of one-dimensional flame structures called flamelets [69,71]. The basic assumption of the classical flamelet models is based on the observation that in most applications combustion occurs in thin regions. This means that a three-dimensional flame can be considered as an ensemble of one-dimensional flame structures. The major drawback of most flamelet models is that it is not straightforward to extend the model to include more time-scales. In an effort to bring the chemical reduction techniques and the laminar flamelet models together, the Combustion Technology section at the Eindhoven University of Technology advanced two new reduction methods, i.e., the Flamelet-Generated Manifolds method [61], which is similar to flame prolongation of ILDM (FPI) [32], and the Phase-Space Intrinsic Low-Dimensional Manifold method (PS-ILDM) [10].

The basic idea of the PS-ILDM method is to apply an eigenvalue decomposition, in a similar fashion as the ILDM method, only now by also explicitly including transport. Although it is a very promising reduction method, it is not straightforward to apply to actual combustion systems. Furthermore, in the cases tested by Bongers [10], it was shown that the PS-ILDM was equally accurate as the ILDM method and less accurate than the FGM approach.

The Flamelet-Generated Manifolds method can be considered as a combination between the ILDM and the laminar flamelet approach. The basic assumption of FGM and the

laminar flamelet approach are the same, i.e., a three-dimensional flame can be considered as an ensemble of one-dimensional flamelets. The implementation however, has more in common with the ILDM approach. In the FGM method, flamelet simulations are performed in an a-priori step, after which the chemical states during the flamelet simulations are stored in a manifold. The manifold is subsequently parameterized by controlling variables, which are often (linear combinations of) species mass fractions. Increasing the dimension of the manifold and thus the number of controlling variables is in principle not a problem. Initially, FGM was developed for and successfully applied to premixed flames. However, there are no principal objections to apply it to non-premixed flames as well.

1.4 Purpose of this study

As pointed out in the previous sections, although the computational power is expected to increase in the future, so will the computational demand due to increasingly sophisticated models, e.g., more detailed chemical mechanisms and detailed turbulence models. This means that reducing the computational effort by using chemical or flamelet manifolds will remain important even in the foreseeable future.

As the title of this thesis already suggests, the main goal of this work is to study whether the Flamelet-Generated Manifolds method can be extended to incorporate unsteady flow effects. This will be done for non-premixed systems, and since FGM was initially developed for and applied to premixed flames, first a set of **unified** flamelet equations will be presented serving as the basis for the Flamelet-Generated Manifolds method. This unified flamelet model relies heavily on the work of de Goey and ten Thije Boonkamp [34], where a laminar flamelet description was derived for premixed flames. In this thesis however, no a-priori assumptions about the nature of the system, i.e., (partially) premixed or non-premixed, are made. The resulting flamelet equations are made up of various contributions, of which the influence of flame stretch and curvature of the flame front have been numerically studied before [34, 35, 37, 61]. Tangential diffusion however, is generally assumed to be negligible and in this thesis this assumption is numerically evaluated. Flame stretch and curvature are also considered and this is done by studying the order of magnitude of each of the individual contributions to the species conservation equation. This will give an indication of which of the individual contributions can be significant and should be taken into account when constructing a manifold.

One of these individual contributions is the unsteady term and the main question that will be answered is whether it is possible to incorporate unsteady flow-field behavior in Flamelet-Generated Manifolds. In order to answer this question two distinct manifolds are created, the first manifold is based on *steady* flamelet simulations while the second manifold is generated by simulating *unsteady* flamelets. One of the key aspects in generating manifolds is to parameterize the manifold in a unique way and with as few controlling variables as possible. For Flamelet-Generated Manifolds based on steady flamelets this is generally not a problem, since each steady flamelet solution is a one-dimensional trajectory in the state-space. As a consequence, when generating higher-dimensional manifolds based on steady flamelets, the dimension of the manifold can be

easily predicted; it is simply equal to the number of parameters that has been varied during the construction of the manifold. For Flamelet-Generated Manifolds based on unsteady flamelet simulations however, this is generally not the case. This is caused by the fact that each unsteady flamelet simulation contains as many time-scales as there are chemically reacting species, which means that an unsteady flamelet simulation can not be considered as a one-dimensional trajectory in state-space. Typical dynamic behavior such as relaxation and phase-shift can play an important role. This means that when constructing a manifold based on unsteady flamelet simulations, a detailed study needs to be performed to the dimensionality of the FGM database. From these results, it can finally be concluded whether unsteady effects can and need to be incorporated in the Flamelet-Generated Manifolds approach.

1.5 Outline of this thesis

In chapter 2, a unified quasi-one-dimensional flamelet model is derived which is capable of describing both (partially) premixed as well as non-premixed combustion systems. To this end, the combustion process is divided into three sub-problems, i.e., 1) fluid motion and mixing of enthalpy and elements, 2) the flame front dynamics and 3) the dynamics of the internal flame structure embedded within this flame front. Furthermore, it is explained how the set of flamelet equations can be used within the concept of the FGM method.

In chapter 3, the quasi-one-dimensional species conservation equation is subdivided into several individual contributions, i.e., an unsteady term, normal transport, flame stretch, curvature, tangential diffusion and the chemical production and consumption terms, respectively. Each of these contributions is evaluated numerically using the coordinate transformation that was introduced in chapter 2. Evaluating and comparing all the individual contributions will be done for three different two-dimensional flames, i.e., one premixed flame and two non-premixed flames. This will give an indication of which of the individual contributions can be significant and should be taken into account when constructing a manifold.

In the following two chapters, it is studied whether or not unsteady flow effects can be captured and incorporated within Flamelet-Generated Manifolds. In chapter 4 this is done for one-dimensional flames which are far away from the steady extinction limit and in chapter 5 one-dimensional flames are considered where the applied strain-rate is around or even beyond the steady extinction limit. In the final chapter of this thesis, chapter 6, all the conclusions of the previous chapters are summarized.

CHAPTER TWO

Towards a Unified Flamelet-Generated Manifolds Approach

A so-called Unified Flamelet Model, capable of describing premixed, non-premixed and partially premixed flames, is proposed. As a first step, the combustion process is decomposed into three distinct sub-problems, i.e., 1) fluid motion and mixing of enthalpy and elements, 2) the flame front dynamics and 3) the dynamics of the internal flame structure embedded within this flame front. The flame front dynamics can be described by a so-called principal controlling variable \mathcal{Y} , for which a conservation equation can be solved. Additionally, a coordinate transformation to an orthogonal curvilinear coordinate system is introduced, resulting in a set of quasi-one-dimensional equations. From a computational point of view, not much is gained yet and therefore, the Flamelet-Generated Manifolds method is introduced as a way to significantly reduce the complexity of the system without losing too much accuracy. Furthermore, how to practically generate Flamelet-Generated Manifolds is also explained and finally, a short overview of various simulations where FGM is applied is given.

It is well known that simulating a complex combusting system in all its details generally involves huge computational costs. This is caused by the large number of chemical reacting species which are strongly coupled. Furthermore, the set of partial differential equations that describe the species evolution is highly non-linear. Computationally, this alone would already be quite a demanding task, however, to make things worse, all the (chemical) time-scales that are present, span a multitude of orders. In the end, a very large, stiff system of strongly coupled, non-linear partial differential equations remains and solving such a system is very CPU-intensive. Simulating a practical combustion system without simplifications is therefore simply not feasible. Fortunately, as it appears, many combustion systems are dominated by a handful of (slow) processes only. This is due to the fact that the fastest modi rapidly become exhausted and therefore can often be neglected. This has led to a number of reduction techniques that take advantage of the

observation that combustion can often be predicted reasonably accurate by only a small number of time-scales.

The chemical composition of a system can be regarded as a point in an N_s -dimensional composition space, where N_s is the total number of chemical species present in the system. Subsequently, the thermo-chemical state of a system can be fully described by the chemical composition, the enthalpy and the pressure of the system. This means that the thermo-chemical state can be represented by a point in an N_{st} -dimensional state space, where $N_{st} = N_s + 2$. Every combustion process can then be described by a path through this state space. Regarding the aforementioned observation, the fast processes lead to a quick relaxation onto a small subset of the state space, which is generally referred to as a low-dimensional manifold. The remainder of the reaction path is then restricted to this low-dimensional manifold, which can be represented by a reduced number of controlling variables. Suppose such a low-dimensional manifold is available during a complex combustion simulation, then one only needs to solve conservation equations for the reduced number of controlling variables, instead of the complete (stiff) set of partial differential equations. Consequently, a significant reduction of the computational effort can be achieved.

The obvious question that arises is: how does one find such a manifold? Unfortunately, there is no such thing as *the* manifold, and hence, it cannot be found. In fact the manifold is defined by the specific, often a-priori assumptions that are used to generate it. There are many different approaches to reduce the computational effort, and generally there are two distinct ways to do this: 1) purely chemically based reduction techniques and 2) flamelet based reduction methods. The chemical reduction techniques are based on detailed analyses of the chemical time-scales associated with reacting species [47, 52, 79]. The major advantage of many chemical reduction techniques is that it provides a systematical classification of all the chemical time-scales that are present. However, in regions where transport effects are also important, i.e., in the colder regions, these chemical reduction techniques are less suitable. Laminar flamelet models on the other hand are based on the assumption that many flames can be considered thin compared to the flow length-scales [69]. In other words, the chemical time-scales are much smaller than the flow time-scales, i.e., the internal structure of the reaction layer of these one-dimensional flames is almost frozen in time. Traditionally, the chemical reduction techniques and the laminar flamelet models were considered to be two distinctly different approaches, but with the introduction of Flamelet-Generated Manifolds [61] (FGM) and Flame-Prolongation of ILDM [32] (FPI), the gap between the chemical reduction techniques and the laminar flamelet models has been bridged.

In the FGM method, one-dimensional flame structures, flamelets, are used to generate a manifold. The big advantage of FGM is that not only chemistry is taken into account, but also (diffusive) transport, which can be of the same order of magnitude in regions where chemistry is not the dominant process. By definition, each steady flamelet solution spans a one-dimensional manifold and by varying a representative set of parameters, different flamelet solutions can be combined in order to span also higher-dimensional manifolds.

To derive an appropriate set of representative flamelets the full combustion problem is divided into three sub-problems, i.e., 1) fluid motion and mixing of enthalpy and elements, 2) the dynamics of the flame-front (described by a principal controlling

variable) and 3) the dynamics of the internal flame structure (described by a small number of additional controlling variables), which is attached to the flame-front. This approach is based on the observation that in many combustion applications a flame can be regarded as a thin interface moving through Cartesian space. Moreover, the fact that flames are often very thin is a clear indication that the majority of the time-scales are indeed small, which means that the process can be accurately described by a reduced number of parameters.

When a flame is defined as the region where a suitable variable \mathcal{Y} assumes values within a certain interval to be specified later, then tracking the flame front merely becomes a case of describing the (unsteady) behavior of \mathcal{Y} and how \mathcal{Y} is affected by its surroundings. On one end of the spectrum, i.e., for premixed flames, often a kinematic equation, sometimes referred to as the G-equation [93], is used to describe the unsteady evolution of the flame-front. On the other end of the spectrum, i.e., for non-premixed flames, a full conservation equation for \mathcal{Y} is solved, taking transport and (if necessary) chemical reactions into account [69]. In non-premixed combustion often the mixture fraction Z is defined as principal controlling variable \mathcal{Y} . Furthermore, in mixed systems it is not straightforward to combine these two approaches. In section 2.1 a unified approach will be presented, capable of describing both (partially) premixed as well as non-premixed flames. Furthermore, it will be shown that in fact, within this unified approach, solving either a kinematic equation or a full conservation equation for \mathcal{Y} is fully equivalent.

In this thesis it is intended to generalize the FGM concept and derive a set of quasi-one-dimensional equations which is able to describe premixed, partially-premixed and non-premixed flames. To that end, a combination of mixing and reaction progress variables, is proposed. However, it might be necessary to extend the number of progress variables if either a higher accuracy is needed or in order to describe the internal flame front dynamics, i.e., $c = c_1, \dots, c_N$ are used as controlling variables describing the slowest processes in the flame, like in ILDM or CSP. In a more general sense, the controlling variable can contain both species mass fractions Y_1, \dots, Y_n as well as mixing variables Z_1, \dots, Z_m . The question remains, how to span a representative manifold? This can be achieved by varying specific (and representative) boundary conditions for each of the controlling variables. In any case, the flame is for instance described by one principle controlling variable $c_1 = \mathcal{Y}$ that describes the primary motion of the flame front, while the other controlling variables c_2, \dots, c_N are used for internal dynamics and perturbations.

The flamelet approach that will be used in the remainder of this thesis will be introduced in section 2.1. This will be done by deriving a model that describes the dynamics of the flame-front, which will be presented in section 2.1.1. Following that, the dynamics of the internal flame structure is considered in section 2.1.2. Due to the assumption that a flame can be considered as a thin layer, usually only the contributions of the transport fluxes in the direction normal to the flame are taken into account, while tangential effects are neglected. In order to assess this assumption, a coordinate transformation is introduced that allows for a proper decomposition of the flamelet model in normal and tangential contributions. This ultimately leads to a quasi-one-dimensional flamelet model, where the normal and tangential contributions are separated.

Finally, in section 2.2, the Flamelet-Generated Manifolds approach will be presented. To that end, in section 2.2.1 it will be explained how decoupling the flame front dynamics from the dynamics of the internal flame structure can lead to a reduction technique,

more specifically to FGM. In section 2.2.2 a brief overview of the generation of Flamelet-Generated Manifolds will be given. Following that, a short summary of previous publications where the FGM or FPI methods were applied to a variety of applications is also given in section 2.2.2.

2.1 Unified flamelet model

The one-dimensional, unified flamelet model that will be used in the remainder of this thesis will be presented in this section. First the equations describing the flame front dynamics are derived in section 2.1.1. This is done by introducing a so-called flame-front velocity v_f , which is subsequently decomposed in two major components, i.e., a normal component that describes the movement of the flame-front perpendicular to itself and a tangential component that ultimately accounts for flame stretch, which will be introduced as well. Following that, the set of quasi-one-dimensional equations describing the dynamics of the internal flame structure is derived in section 2.1.2.

In previous publications [34, 61, 64] similar one-dimensional flamelet equations were derived for premixed flames. Therefore, a final but crucial point has to be made here and that is that no a-priori assumptions are made about the premixed or non-premixed nature of the flame. In other words, the flamelet model that will be presented in this chapter is a **unified** flamelet model in the sense that it can be used to describe premixed flames and non-premixed flames, but also partially premixed flames.

2.1.1 Flame front dynamics

A flame can be defined as the region in the spatial domain, where $\mathcal{Y}_1 \leq \mathcal{Y} \leq \mathcal{Y}_2$ for a certain scalar variable \mathcal{Y} . The subscripts 1 and 2 indicate the two boundaries of the flame that are separated by the flame, i.e., for premixed flames these two sides correspond to the unburnt and the burnt side, respectively and for non-premixed flames these two sides would be the fuel and oxidizer side, respectively. Often, species mass fractions, or linear combinations of species mass fractions, are chosen as suitable controlling variable \mathcal{Y} for which $\nabla \mathcal{Y} \neq 0$ holds in the entire domain. Note that for premixed flames often product species are used as principal controlling variable, for instance the mass fraction of carbon dioxide $\mathcal{Y} = Y_{\text{CO}_2}$, while for non-premixed flames it is more common to use the mixture fraction as principal controlling variable, i.e., $\mathcal{Y} = Z$. Flame surfaces can now be defined as iso-surfaces of \mathcal{Y} where $\mathcal{Y}(x, t) = \mathcal{Y}_0$ for some constant \mathcal{Y}_0 . In general, flame surfaces are curved and wrinkled surfaces moving through Cartesian space. The dynamic behavior of \mathcal{Y} , which can manifest in translation, compression, curving or wrinkling of the flame surfaces, can be described by a kinematic equation as follows:

$$\frac{d\mathcal{Y}}{dt} = \frac{\partial \mathcal{Y}}{\partial t} + v_f \cdot \nabla \mathcal{Y} = 0, \quad (2.1)$$

meaning that a point on an iso-surface of \mathcal{Y} stays on that surface for all time t . The transient behavior of the iso-surfaces of \mathcal{Y} , and hence the dynamics of the flame front, is

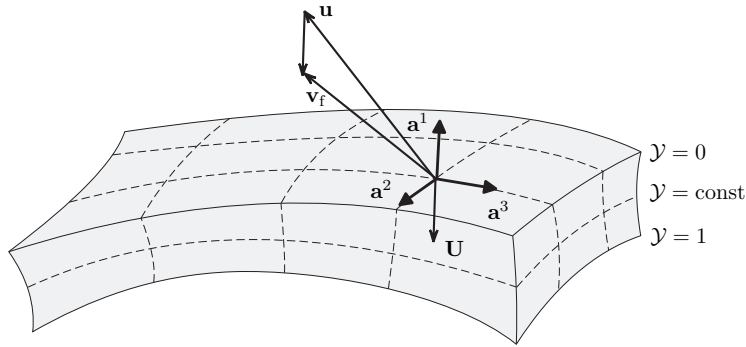


Figure 2.1: Schematic representation of a flame front. Shown here are several flame surfaces at constant values of the principal controlling variable, i.e., $\mathcal{Y} = \text{constant}$. Also shown are the three velocity vectors \mathbf{u} , \mathbf{v}_f and \mathbf{U} , which represent the fluid velocity, the flame front velocity and the relative displacement velocity of the iso-surfaces of \mathcal{Y} , respectively.

described by equation (2.1). In order to solve (2.1), the flame front velocity \mathbf{v}_f has to be known first.

Figure 2.1 shows several iso-surfaces of the principal controlling variable \mathcal{Y} . At this point, it is convenient to introduce a flame-adapted coordinate system of which the basis vectors are chosen such that \mathbf{a}^1 is perpendicular to the iso-surfaces of \mathcal{Y} . Note that the basis vectors in figure 2.1 are depicted as an orthogonal coordinate system. In general however, \mathbf{a}^2 and \mathbf{a}^3 do not have to be perpendicular to each other or to \mathbf{a}^1 . In fact the classical, non-premixed flamelet model by Peters [69] is a well-known example of a curvilinear coordinate system where \mathbf{a}^2 and \mathbf{a}^3 are non-orthogonal to \mathbf{a}^1 . In [69], the first basis vector \mathbf{a}^1 is defined as the gradient of the mixture fraction Z , which acts as the first controlling variable. The second and third basis vectors \mathbf{a}^2 and \mathbf{a}^3 however, merely replace the Cartesian coordinates x_2 and x_3 , respectively. As a result, \mathbf{a}^2 and \mathbf{a}^3 are perpendicular to each other, but in general not to \mathbf{a}^1 .

Also shown in figure 2.1 are the three velocity vectors \mathbf{u} , \mathbf{v}_f and \mathbf{U} , which represent the fluid velocity, the flame front velocity and a relative displacement velocity of the iso-surfaces of \mathcal{Y} , respectively. The local flame front velocity \mathbf{v}_f dictates the movement of the flame front, and can be described as a superposition of the local fluid velocity \mathbf{u} and a relative displacement velocity \mathbf{U} as follows¹:

$$\mathbf{v}_f = \mathbf{u} + \mathbf{U}. \quad (2.2)$$

For premixed systems the relative displacement velocity \mathbf{U} is better known as the so-called displacement speed S_d [26, 27] and in the literature, many ways to model S_d can be found [1, 20, 25, 45, 56, 58]. The main drawback is that most of these empirical models

¹If $\mathbf{u} = \mathbf{v}_f - U\mathbf{n}$ and equation (2.4) are used in (2.1), an equation that is very similar to the so-called G-equation [93] is found:

$$\frac{d\mathcal{Y}}{dt} = \frac{\partial\mathcal{Y}}{\partial t} + \mathbf{u} \cdot \nabla\mathcal{Y} = U|\nabla\mathcal{Y}|.$$

are only valid within a very specific operating range. Furthermore, for non-premixed systems, it is not common practice to introduce a displacement speed, and therefore empirical models do not even exist. However, from a simple decomposition of the velocity components, it can be argued that a displacement speed may also be introduced for non-premixed flames.

Regarding the evolution of the iso-surfaces of \mathcal{Y} , only the normal velocity component is relevant. Therefore, it is convenient to decompose the flame front velocity v_f into normal and tangential components as follows:

$$v_f = v_f^n + v_f^t, \quad (2.3)$$

where v_f^n describes the actual movement of the flame front, while the tangential velocity component v_f^t represents the flame front velocity in the \mathcal{Y} -planes. Now, the relative displacement velocity \mathbf{U} only has a component that is perpendicular to the surface of the flame, i.e., $\mathbf{U} = Un$, where the normal vector \mathbf{n} is defined as:

$$\mathbf{n} = -\frac{\nabla\mathcal{Y}}{|\nabla\mathcal{Y}|} = -\frac{\mathbf{a}^1}{|\mathbf{a}^1|}, \quad (2.4)$$

which means that the normal vector is directed towards the unburnt side for premixed flames if $\mathcal{Y} = Y_{product}$ which can be Y_{CO_2} or Y_{H_2O} for instance, while for non-premixed flames it points towards the oxidizer side when $\mathcal{Y} = Z$ is chosen. Note that by this definition of the normal vector, the first unit vector e_1 becomes:

$$e_1 = \frac{\mathbf{a}^1}{|\mathbf{a}^1|} = -\mathbf{n}. \quad (2.5)$$

The normal and tangential components of the flame front velocity v_f can now be written as follows:

$$v_f^n = \mathbf{u}^n + Un, \quad (2.6)$$

$$v_f^t = \mathbf{u}^t, \quad (2.7)$$

where \mathbf{u}^n and \mathbf{u}^t are the normal and tangential components of the fluid velocity, respectively. From (2.6) it follows that even for non-premixed flames, there are situations where the relative displacement velocity \mathbf{U} is not equal to zero. The evaluation of the tangential component of the flame front velocity is rather straightforward, i.e., it is merely the tangential component of the fluid velocity. The evaluation of the normal component of the flame front velocity on the other hand, is not. From (2.6), it follows that in order to compute v_f^n , first \mathbf{U} has to be determined.

Alternatively, in order to circumvent these problems, one could also use the conservation equation of \mathcal{Y} to derive an expression for the flame front velocity v_f . The conservation equation of \mathcal{Y} is given below:

$$\frac{\partial\rho\mathcal{Y}}{\partial t} + \nabla \cdot (\rho\mathbf{u}\mathcal{Y}) - \nabla \cdot (\rho D_y \nabla\mathcal{Y}) = \dot{\omega}_y, \quad (2.8)$$

which describes the local change of \mathcal{Y} as a function of time t , resulting from an imbalance between convection, diffusion and chemical reactions². When (2.8) is combined with the continuity equation (1.11) and is subsequently divided by the density ρ , the above equation can be written as follows:

$$\frac{\partial \mathcal{Y}}{\partial t} + \mathbf{u} \cdot \nabla \mathcal{Y} = \frac{\dot{\omega}_{\mathcal{Y}} + \nabla \cdot (\rho D_{\mathcal{Y}} \nabla \mathcal{Y})}{\rho}. \quad (2.9)$$

Subtraction of (2.9) from equation (2.1) finally results in the expression for \mathbf{v}_f :

$$\mathbf{v}_f \cdot \nabla \mathcal{Y} = \mathbf{u} \cdot \nabla \mathcal{Y} - \frac{\dot{\omega}_{\mathcal{Y}} + \nabla \cdot (\rho D_{\mathcal{Y}} \nabla \mathcal{Y})}{\rho}, \quad (2.10)$$

which could subsequently be used to solve equation (2.1). Dividing equation (2.10) by $|\nabla \mathcal{Y}|$ and combining it with equation (2.6), leads to an expression for the absolute value of the relative displacement velocity:

$$U = \frac{\dot{\omega}_{\mathcal{Y}} + \nabla \cdot (\rho D_{\mathcal{Y}} \nabla \mathcal{Y})}{\rho |\nabla \mathcal{Y}|}. \quad (2.11)$$

Obviously, solving equation (2.1) in conjunction with (2.10) as a model for \mathbf{v}_f is equivalent to solving (2.9). Within the FGM framework however, equation (2.9) is preferred.

Concluding, it can be said that the dynamics of the flame front can be described by solving a kinematic equation for a so-called principal controlling variable \mathcal{Y} . In order to solve this kinematic equation, the flame front velocity \mathbf{v}_f has to be modeled. For premixed flames, many empirical models are readily available and have been known to perform quite well, but often only under specific conditions. For non-premixed flames on the other hand, such models do not exist. Therefore, a more rigorous approach is taken. Instead of solving a kinematic equation for \mathcal{Y} , a conservation equation is solved for \mathcal{Y} . It was shown that from this conservation equation, it was possible to derive an expression for the flame front velocity \mathbf{v}_f , thereby nicely connecting the two different approaches.

2.1.2 Internal flame dynamics

Now that it is possible to track the iso-surfaces of a flame via (2.9), the next step is to describe the dynamics of the internal flame structure. As said, within the flamelet regime, a multi-dimensional flame is assumed to be representable by one-dimensional flamelets. Going from a fully three-dimensional flame model to a one-dimensional flamelet model, requires certain terms to be neglected, which can be analyzed best in a flame-adapted coordinate system. In order to provide a well-established foundation, first the derivative operators of a generalized curvilinear coordinate system are introduced. After that, a more convenient curvilinear coordinate system, i.e., an orthogonal one, is introduced. This orthogonal curvilinear coordinate system subsequently leads to a reformulation of the three-dimensional flame model, and when specific choices for the basis vectors are made, the resulting model can be decomposed in contributions normal to the flame surfaces and contributions that take place within the flame surfaces themselves.

²Note that the full set of combustion equations (1.36)-(1.40) would have to be solved. This is due to the fact that the chemical source-term $\dot{\omega}_{\mathcal{Y}}$ can in principle be a function of the pressure, temperature and all the other species mass fractions.

Differential operators in a generalized curvilinear space

In order to decompose the flame model in contributions that are normal and tangential to the flame front, the following generalized curvilinear coordinate system $\xi(x, t) = (\xi^1, \xi^2, \xi^3)$ is introduced, such that

$$\mathcal{Y}(x, t) = \mathcal{Y}(\xi^1), \quad (2.12)$$

holds, which implicitly fixes the ξ^1 iso-surfaces onto the iso-surfaces of \mathcal{Y} . Another important consequence is that \mathcal{Y} does not depend on τ , which represents time in the transformed space. This is a direct result of the choice to fix the curvilinear coordinate system to the iso-surfaces of \mathcal{Y} .

Since a material derivative is independent from the coordinate system, the time-derivative with respect to the Cartesian coordinate system is related to the time-derivative with respect to the curvilinear coordinate system via the material derivative³. The material derivative can be expressed as a function of the Cartesian coordinate system [46] and for a scalar quantity A this leads to:

$$\frac{DA}{Dt} = \frac{\partial A}{\partial t} + \mathbf{u}_x \cdot \nabla A, \quad (2.13)$$

where the first part represents the local rate of change at a fixed position in Cartesian space. The second part is the so-called advective derivative, which results from the fact that when an element is advected from one position to the other with velocity \mathbf{u}_x , the local value of A changes. Similarly, the material derivative can also be defined with respect to a (curvilinear) coordinate system that moves with velocity \dot{x} . For the scalar quantity A this becomes:

$$\frac{DA}{Dt} = \frac{\partial A}{\partial \tau} + \mathbf{u}_\xi \cdot \nabla A, \quad (2.14)$$

where the first part again represents the local rate of change, only now at a fixed position in the transformed (moving) space. Figure 2.2 shows the relation between \mathbf{u}_x and \mathbf{u}_ξ . Shown are a particle P and an iso-line ξ_0^1 at two different time instances, i.e., at t and $t + dt$ respectively. Initially the particle P coincides with the origin of the curvilinear coordinate system, i.e., $\xi^1 = 0$ and $\xi^2 = 0$. A short time later, the curvilinear coordinate system has traveled with velocity \dot{x} to a different position than the particle P did. Particle P has moved from $\mathbf{r}(t)$ to $\mathbf{r}(t + dt)$ with velocity \mathbf{u}_x . This means that the velocity of particle P with respect to the moving coordinate system, can be written as follows:

$$\mathbf{u}_\xi = \mathbf{u}_x - \dot{x}. \quad (2.15)$$

Combining the right-hand-sides of equations (2.13) and (2.14) with equation (2.15), leads to the following relation between the time-derivative in Cartesian space and the time derivative in transformed space:

$$\frac{\partial A}{\partial \tau} = \frac{\partial A}{\partial t} + \dot{x} \cdot \nabla A. \quad (2.16)$$

³Within the realm of Newtonian or classical mechanics this phenomenon is known as Galilean invariance.

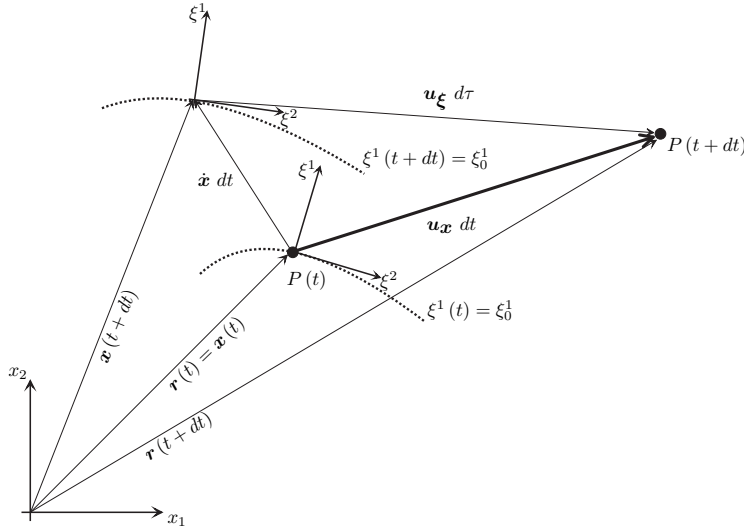


Figure 2.2: Schematic representation of a displacement vector $u_x dt$, indicating the displacement of a particle P from initial position $r(t) = x(t)$ to position $r(t + dt)$. Also shown are the displacement vector of the curvilinear coordinate system $\dot{x} dt$ and the displacement vector of particle P with respect to the curvilinear coordinate system $u_\xi d\tau$. From the laws of vector addition it follows that $u_\xi = u_x - \dot{x}$.

As a result of the specific coordinate transformation (2.12), the time-derivative of \mathcal{Y} with respect to the curvilinear coordinate system is equal to zero, i.e.:

$$\frac{\partial \mathcal{Y}}{\partial \tau} = \frac{\partial \mathcal{Y}}{\partial t} + \dot{x} \cdot \nabla \mathcal{Y} = 0. \quad (2.17)$$

Note that equation (2.17) is almost identical to equation (2.1). Combining these two equations, leads to:

$$(\mathbf{v}_f - \dot{x}) \cdot \mathbf{a}^1 = 0, \quad (2.18)$$

meaning that the components of \mathbf{v}_f and \dot{x} normal to the iso-surfaces of \mathcal{Y} have the same values. This is a direct result of the choice to attach the curvilinear coordinate system onto the flame-surfaces. For the ξ^2 and ξ^3 components of \dot{x} , now the following arbitrary but convenient choice is made:

$$(\mathbf{u} - \dot{x}) \cdot \mathbf{a}^i = 0, \quad \text{with } i = [2, 3], \quad (2.19)$$

which states that the local velocity of the ξ^2 and ξ^3 -coordinates is the same as the fluid velocity component in ξ^2 and ξ^3 -direction, respectively.

As a result of the coordinate transformation to a generalized curvilinear system, the various derivative operators can now be expressed in terms of the curvilinear coordinates. In Appendix A a more detailed derivation is given. Here only the derivative operators that are present in the conservation equations are given:

$$\nabla A = \mathbf{a}^i A_{\xi^i}, \quad (2.20)$$

$$\nabla \cdot \mathbf{f} = \frac{1}{\sqrt{g}} \left[\sqrt{g} \mathbf{a}^i \cdot \mathbf{f} \right]_{\xi^i}, \quad (2.21)$$

$$\nabla \cdot (b \nabla A) = \frac{1}{\sqrt{g}} \left[b \sqrt{g} g^{ij} A_{\xi^j} \right]_{\xi^i}, \quad (2.22)$$

$$\frac{\partial A}{\partial t} = \frac{\partial A}{\partial \tau} - \dot{\mathbf{x}} \cdot \nabla A, \quad (2.23)$$

where $[...]_{\xi^i}$ indicates the derivative with respect to ξ^i . Furthermore, A is an arbitrary, differentiable, scalar quantity, \mathbf{a}^i is the i^{th} contravariant basis vector, ξ^i represent the curvilinear coordinates, \mathbf{f} represents an arbitrary vector quantity, \sqrt{g} is the Jacobian of the coordinate transformation, b is also an arbitrary, differentiable, scalar quantity, e.g., conductivity or diffusivity. Finally, g^{ij} is an element of the contravariant metric-tensor, which describes the geometry of the transformation.

Orthogonal curvilinear coordinate system

As mentioned in 2.1.1, in general a curvilinear coordinate system does not necessarily have to be orthogonal. However, to avoid cross-terms that can arise when a non-orthogonal system is used, i.e., the cross-terms in equations (2.20)-(2.23), in the remainder of this thesis the specific choice for an orthogonal curvilinear coordinate system is made. This means that the covariant metric tensor (g_{ij}) and the contravariant metric tensor (g^{ij}), only have non-zero components on their diagonal. The Jacobian of the transformation can now be written as follows:

$$\sqrt{g} = \sqrt{\det(g_{ij})} = h_{\xi^1} h_{\xi^2} h_{\xi^3}, \quad (2.24)$$

where the scale factors h_{ξ^i} are given by:

$$h_{\xi^i} = \left| \frac{\partial \mathbf{x}}{\partial \xi^i} \right|. \quad (2.25)$$

Applying the transformed divergence operators to the continuity equation (1.11), leads to:

$$\frac{\partial \rho}{\partial t} + \frac{1}{\sqrt{g}} \frac{\partial}{\partial \xi^i} \left(\sqrt{g} \mathbf{a}^i \cdot \mathbf{u} \rho \right) = 0, \quad (2.26)$$

where the Einstein summation convention was used. It is apparent that equation (2.26) still explicitly contains tangential transport, i.e., for $i = [2, 3]$, which are commonly associated with stretch-like effects. In order to reformulate equation (2.26) in a quasi-one-dimensional manner, here a so-called mass based stretch rate [33] is introduced as follows:

$$\rho K_M = \frac{\partial \rho}{\partial t} + \nabla \cdot (\rho \mathbf{v}_f), \quad (2.27)$$

which, after applying the transformed divergence operator becomes:

$$\rho K_M = \frac{\partial \rho}{\partial t} + \frac{1}{\sqrt{g}} \frac{\partial}{\partial \xi^i} \left(\sqrt{g} \mathbf{a}^i \cdot \mathbf{v}_f \rho \right). \quad (2.28)$$

Subtracting equation (2.26) from (2.28) and applying the definition for the flame front velocity (2.2), leads to:

$$\rho K_M = \frac{1}{\sqrt{g}} \frac{\partial}{\partial \xi^1} \left(\sqrt{g} \mathbf{a}^1 \cdot \mathbf{U} \rho \right), \quad (2.29)$$

where the ξ^2 and ξ^3 derivatives vanished due to the fact that the relative displacement velocity \mathbf{U} only has a component in the direction normal to the flame. Furthermore, if the line increment ∂s is defined as $h_{\xi^1} \partial \xi^1$ and the surface increment σ is introduced as $h_{\xi^2} h_{\xi^3}$, equation (2.29) can be reformulated as follows⁴:

$$\rho K_M = -\frac{1}{\sigma} \frac{\partial}{\partial s} (\sigma m), \quad (2.30)$$

where the mass consumption rate m is defined as follows⁵:

$$m = \rho U. \quad (2.31)$$

Introducing the curvature κ as follows:

$$\kappa = \nabla \cdot \mathbf{n} = -\frac{1}{\sigma} \frac{\partial \sigma}{\partial s}, \quad (2.32)$$

the continuity equation (1.11) can finally be reformulated in terms of curvilinear coordinates:

$$\frac{\partial m}{\partial s} = -\rho K_M + m \kappa. \quad (2.33)$$

Decomposing the flame front velocity \mathbf{v}_f into normal and tangential components gives more insight in the actual contributions of the mass based stretch rate, and thus also in the contributions of the continuity equation itself, cf. [33]:

$$\mathbf{v}_f = \mathbf{v}_f^n + \mathbf{v}_f^t = v_{\xi^1} \mathbf{e}_1 + \mathbf{v}_f^t. \quad (2.34)$$

Now (2.27) can be written as follows:

$$\rho K_M = \frac{D\rho}{Dt} + \rho \nabla \cdot \mathbf{v}_f^t + \rho v_{\xi^1} \nabla \cdot \mathbf{e}_1 + \rho \mathbf{e}_1 \cdot \nabla v_{\xi^1}. \quad (2.35)$$

The first term is commonly known as the material derivative, while the second contribution represents flow straining, and the third term is a result of curvature due to movement of the flame front itself. Both these terms were also reported by Law [48]. The fourth contribution is new and arises due to the unsteady flame thickness variations caused by varying flame front velocities among different flame contours.

⁴Taking the inner-product of the first contravariant basis vector and the normal vector results in:

$$\mathbf{a}^1 \cdot \mathbf{n} = -\frac{\mathbf{a}^1 \cdot \mathbf{a}^1}{|\mathbf{a}^1|} = -|\mathbf{a}^1|,$$

which is also the reciprocal of the scale factor h_{ξ^1} , except for the minus sign.

⁵See Appendix B for a more in-depth discussion regarding the meaning of the relative propagation velocity \mathbf{U} and the mass consumption rate m for non-premixed flames.

Unified flamelet equations

Likewise, the conservation equations of the principal controlling variable \mathcal{Y} , the species mass fractions Y_n and the enthalpy h can also be reformulated in terms of the orthogonal curvilinear coordinates. Introducing the fluxes of the principal controlling variable, species mass fractions and enthalpy as follows:

$$F_{\mathcal{Y}} = m\mathcal{Y} - \rho D_{\mathcal{Y}} \frac{\partial \mathcal{Y}}{\partial s}, \quad (2.36)$$

$$F_n = mY_n - \rho D_n \frac{\partial Y_n}{\partial s}, \quad n \in [1, N_s], \quad (2.37)$$

$$F_h = mh - \frac{\lambda}{c_p} \frac{\partial h}{\partial s} - \frac{\lambda}{c_p} \sum_{n=1}^{N_s} \left(\frac{1}{Le_n} - 1 \right) h_n \frac{\partial Y_n}{\partial s}, \quad (2.38)$$

and applying the transformation rules, finally leads to the following set of quasi-one-dimensional flamelet equations:

$$\frac{\partial m}{\partial s} = -\rho K_M + m\kappa, \quad (2.39)$$

$$\frac{\partial F_{\mathcal{Y}}}{\partial s} - \dot{\omega}_{\mathcal{Y}} = -\rho K_M \mathcal{Y} + F_{\mathcal{Y}} \kappa, \quad (2.40)$$

$$\rho \frac{\partial Y_n}{\partial \tau} + \frac{\partial F_n}{\partial s} - \dot{\omega}_n = -\rho K_M Y_n + F_n \kappa + Q_n, \quad n \in [1, N_s], \quad (2.41)$$

$$\rho \frac{\partial h}{\partial \tau} + \frac{\partial F_h}{\partial s} = -\rho K_M h + F_h \kappa + Q_h, \quad (2.42)$$

which describe the internal flame dynamics with respect to the principal controlling variable \mathcal{Y} ⁶. For completeness, the continuity equation has also been included in the above set of equations. Note that all perturbations from flat, one-dimensional flame behavior have been collected at the right-hand-side. Furthermore, Q_n and Q_h are short notations for diffusion-like derivatives in ξ^2 and ξ^3 -direction:

$$Q_n = \frac{1}{\sqrt{g}} \frac{\partial}{\partial \xi^i} \left(\rho D_n \sqrt{g} g^{ii} \frac{\partial Y_n}{\partial \xi^i} \right), \quad (i = 2, 3), \quad n \in [1, N_s], \quad (2.43)$$

$$Q_h = \frac{1}{\sqrt{g}} \frac{\partial}{\partial \xi^i} \left(\frac{\lambda}{c_p} \sqrt{g} g^{ii} \frac{\partial h}{\partial \xi^i} \right) + \frac{1}{\sqrt{g}} \frac{\partial}{\partial \xi^i} \left(\frac{\lambda}{c_p} \sum_{n=1}^{N_s} \left(\frac{1}{Le_n} - 1 \right) h_n \sqrt{g} g^{ii} \frac{\partial Y_n}{\partial \xi^i} \right), \quad (i = 2, 3), \quad (2.44)$$

⁶As a result of the coordinate transformation with \mathcal{Y} as principal controlling variable, both $\frac{\partial \mathcal{Y}}{\partial \tau}$ and $Q_{\mathcal{Y}}$ are per definition equal to zero.

which describe diffusive transport of Y_n and h along ξ^2 and ξ^3 -direction, respectively.

Concluding remarks

It can be concluded that the original combustion model, i.e., equations (1.36)-(1.40) have been reformulated in terms of an orthogonal curvilinear coordinate system, which makes it possible to distinguish between contributions that are normal and tangential to the flame surfaces. The unsteady and normal terms are collected at the left-hand-sides of (2.39) - (2.42), while all tangential contributions are gathered at right-hand-sides. These tangential contributions are made up of several distinct phenomena that arise due to the fact that a flame is in principle a three-dimensional entity:

1. flow straining, flame thickness variations and curvature, which are represented by the mass based stretch rate K_M and the curvature κ .
2. diffusive transport of species and enthalpy along flame surfaces, which is gathered in Q_n and Q_h .

Note that no explicit assumptions regarding the premixed or non-premixed nature of the system are made. In that sense the formulation that has been introduced here has led to a unified flamelet model. On the other hand, since the system has not been reduced, in fact the complete set of partial differential equations has been merely reformulated, not much has been gained from a computational point of view. The huge amount of computational costs for complex industrial applications still inhibits the use of the set of equations (2.39) - (2.42), which are essentially still multi-dimensional equations. In the next section, three of the possible solutions are discussed.

2.2 Flamelet-Generated Manifolds

In the previous section, the combustion process was divided into three separate subproblems, i.e., flow and mixing processes, the dynamics of the flame front and the dynamics of the internal flame structure. Ultimately, this led to a quasi-one-dimensional, unified flamelet model, but as stated, from a computational point of view, not much was gained. This is due to the fact that all chemical time-scales are still present in the model. The most significant reduction of CPU costs can be achieved by removing the stiffness from the combustion process. By recognizing that a major part of the flame front dynamics can be decoupled from the dynamics of the internal flame structure, an important first step is made towards an actual reduction technique.

In the remainder of this chapter, it will be explained how decoupling flame front dynamics from the internal flame structure, can be used within the FGM framework. Therefore, in section 2.2.1 it is explained how a combustion simulation can be divided into three separate subproblems, but also how these subproblems are subsequently combined

to describe a combustion proces. Specifically, the decoupling and interaction between the flame front dynamics and the internal flame structure can be achieved in various ways, of which one is often used in combination with the FGM method. Furthermore, how to practically generate Flamelet-Generated Manifolds will be discussed in section 2.2.2. Finally, it is shown how phenomena like flame stretch, enthalpy variations and local mixing can be taken into account. This is done through various examples of (complex) combustion simulations where FGM has been successfully applied.

2.2.1 Flame front and internal flame structure (de)coupling

In this section it is discussed how the flame front dynamics can be decoupled from the internal flame structure and how these two subproblems interact not only with each other but also with the flow and mixing processes.

The flow and mixing processes are described by the continuity equation (1.36), the three components of the Navier-Stokes equation (1.37), conservation of enthalpy (1.40) and elements (1.9). Note that there are no chemical source-terms, which means that relatively large time-steps can be taken within the flow and mixing solver.

The flame front dynamics can be either described by 1) a kinematic equation for the principal controlling variable \mathcal{Y} , i.e., (2.1) together with (2.10) or 2) a conservation equation for the principal controlling variable \mathcal{Y} , i.e., (2.9). Local perturbations from steady, one-dimensional flame behavior can be represented in a number of ways⁷. One way to do this, is by taking local geometric effects like the stretch rate K_M and curvature κ into account, while alternatively, this can also be parameterized by additional controlling variables, c_2, \dots, c_n .

Solving the flamelet equations can also be done in different ways, for instance, 1) using an online solving procedure where the flamelet equations are solved as a part of the combustion simulation or, 2) pre-computing a series of representative flamelets and storing the flamelet solutions in tables as is done within the FGM framework. During a detailed combustion simulation, the flame front dynamics can be coupled with the internal flame structure in various ways, but here only three solving strategies are shown.

Figure 2.3 shows a schematic diagram of an online solving procedure, as suggested in [34]. As can be seen, the combustion simulation is divided into several sub-problems, which are to be solved in an iterative manner. Because the chemical kinetics are decoupled from the flow-field, the flow and mixing variables can be solved in a non-reacting flow field. Following that, the kinematic equation describing the unsteady evolution of the principal controlling variable can be solved. Applying the coordinate transformation that was outlined in section 2.1.2, the stretch and curvature fields can be extracted using (2.32) and (2.33). The local stretch rate and curvature then serve as input for the online flamelet solver⁸, which computes the species mass fractions Y_n , the temperature T and the transport coefficient $\frac{\lambda}{c_p}$ and finally also the flame front velocity v_f which is needed to update the kinematic equation (2.1).

⁷In the classical flamelet model [69], the scalar dissipation rate χ is the parameter that represents local straining, while more recently also time was added to incorporate flamelet histories.

⁸The internal flame structure has effectively been translated from a three-dimensional problem to a series of one-dimensional simulations.

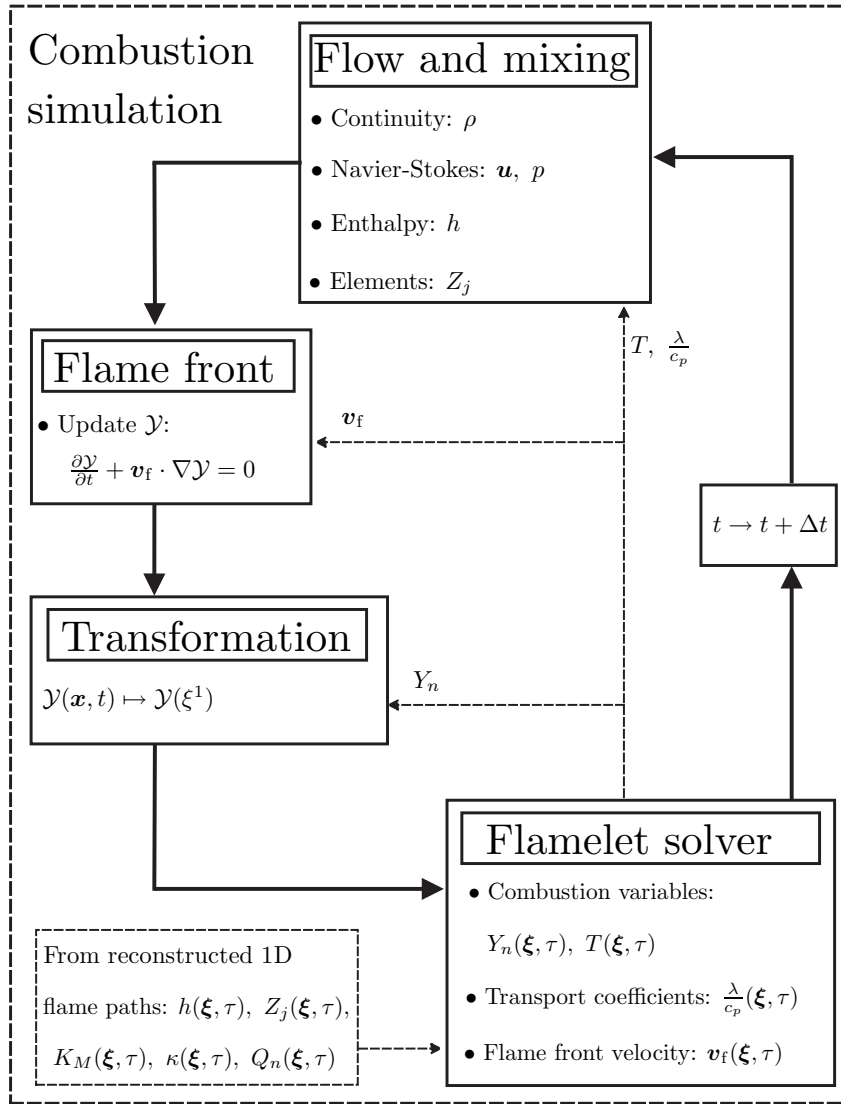


Figure 2.3: Flow diagram of an online solving procedure as proposed by de Goey and ten Thije Boonkkamp [34].

Figure 2.4 shows a schematic diagram of another online solving procedure. Instead of solving an equation to track the flame front, now conservation equations for n controlling variables are solved⁹. During a combustion simulation, several online, parallel running flamelet solvers can be used to simulate a number of representative flamelet solutions. A set of representative initial and boundary conditions can be determined from the combustion simulation. The controlling variables are subsequently used to retrieve all the necessary manifold variables from the generated tables. All the flamelet solutions can be stored each time-step, resulting in a growing flamelet database, much like the In-Situ Adaptive Tabulation (ISAT) technique [78]. The advantage of such a technique is that only a minimum set of flamelets needs to be simulated.

⁹Note that n can be equal to 1.

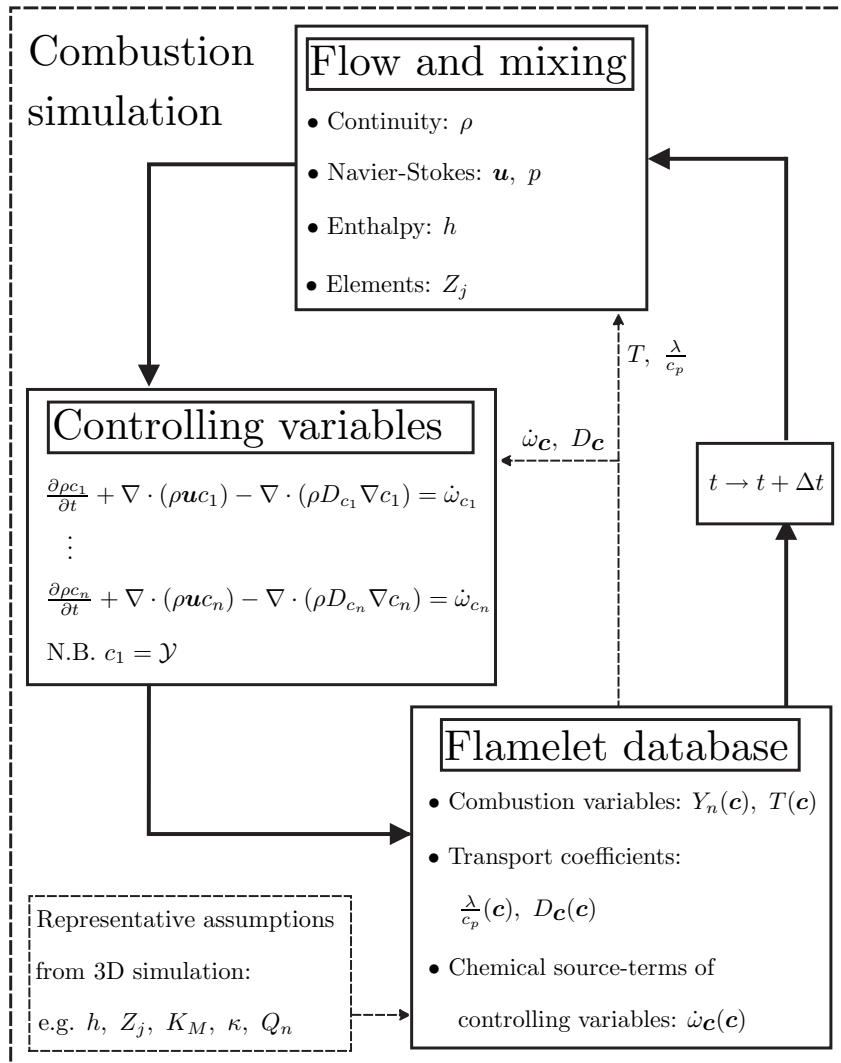


Figure 2.4: Flow diagram of an online solving procedure, where each time-step a new flamelet database is generated using the controlling variables \mathbf{c} to lookup and retrieve all the manifold variables.

Due to the decoupling of flame front dynamics from the internal flame structure, the stiffness that is associated with the chemical kinetics is indirectly removed from the flow and mixing solver. However, since the stiff set of equations is still present within the flamelet solver in both the previous solving procedures, the computational effort will probably not decrease significantly¹⁰.

A major reduction in computation effort can be achieved by actually removing the stiff set of flamelet equations from the combustion simulation itself. This can be seen in figure 2.5, which shows another solving procedure¹¹, i.e., pre-computing a series of representative

¹⁰This was also pointed out by de Goey and ten Thijs Boonkcamp. In [34] de Goey and ten Thijs Boonkcamp argued that as a result of the complex coupling between the flow and mixing processes and the flamelet solver it remains to be seen whether the computational efficiency will increase very much.

¹¹Here only three possible solving strategies are shown, which does not mean that these are the only ones.

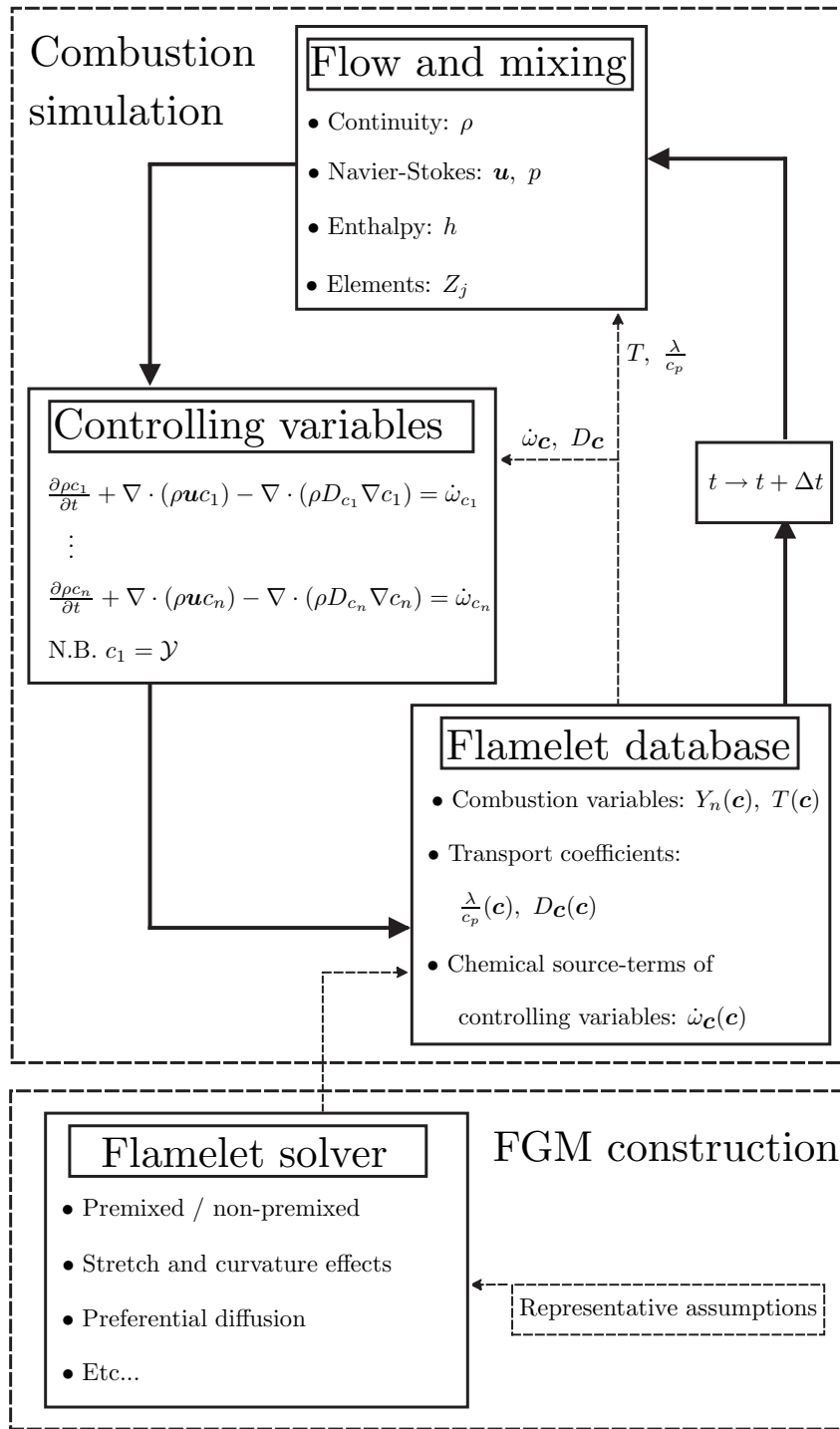


Figure 2.5: Flow diagram of an solving procedure using a pre-computed Flamelet-Generated Manifold.

flamelets. The internal flame structure is incorporated by means of a representative flamelet table that is generated a-priori. In the Flamelet-Generated Manifolds method, it is assumed that flamelets are actually one-dimensional trajectories, or one-dimensional manifolds in the N_{st} -dimensional state space. Furthermore, a collection of these one-

dimensional manifolds can be used to generate higher dimensional manifolds which can be parameterized by a (small) set of controlling variables c . When using the FGM method, instead of solving the kinematic equation to account for flame front dynamics, one needs to solve conservation equations for the controlling variables. During a combustion simulation, the local values of the controlling variables are then used to access the pre-computed FGM table and all the relevant manifold variables are retrieved from the database. The major challenge when constructing a pre-computed manifold, is to include representative phenomena into the FGM. Additionally, a span of appropriate boundary conditions needs to be chosen.

Figures 2.6 and 2.7 show two different types of combustion simulations. Due to the **unified** nature of the flamelet model as described in 2.1, it is now possible to apply the coordinate transformation to both a premixed flame (figure 2.6) as well as a non-premixed flame (figure 2.7). The only difference between the premixed and non-premixed case is the definition of the principal controlling variable \mathcal{Y} . For the premixed flame the mass fraction of CO_2 scaled with its value at the burnt side is selected as the principal controlling variable while for the non-premixed flame the mixture fraction Z is chosen as principal controlling variable.

The premixed flame that can be seen in figure 2.6 (top-left) is a cylindrical expanding, fully premixed flame that is embedded in a turbulent flow-field. The flame is visualized as a false-color plot of atomic oxygen where the color-scale ranges from blue (low values) to red (high values). Due to the turbulence the flame is subjected to flame stretch and curvature, which ultimately results in variations of variables in the ξ^2 -direction, i.e., Q_n terms. Whether or not tangential transport can be neglected, will be studied in chapter 3, where these tangential variations as well as the other contributions to the conservation equations are studied numerically. A more detailed view can be seen in figure 2.6 (top-right) where also the curvilinear coordinate lines are shown. Additionally the grey line indicates a reconstructed flamelet. Figure 2.6 (bottom) shows the flame transformed from Cartesian coordinates to curvilinear, flame-adapted coordinates. The grid-points of the curvilinear coordinate system are located where the iso-lines of ξ^1 intersect the ξ^2 -lines. Note that at certain locations, variations in ξ^2 -direction appear to be of the same order of magnitude as variations in ξ^1 -direction. However, this is caused by the fact that the picture is compressed in ξ^2 -direction.

An example of a two-dimensional non-premixed flame can be seen at the top of figure 2.7, which shows a typical result of a reacting mixing layer subject to a Kelvin-Helmholtz instability. This instability originates on the interface of two opposing flows, i.e., the fuel flows from left to right, above the interface and oxidizer flows in the other direction, below the interface. Figure 2.7 (top-left) shows a false-color plot of the temperature. In figure 2.7 (bottom-left) a more detailed view can be seen, where the curvilinear coordinate lines are shown. The grey line again corresponds to a single reconstructed flamelet which of course coincides with a ξ^2 -line. Figure 2.7 (right) shows the flame in the transformed curvilinear space.

By decoupling the flamelet solver from the flow and mixing solver as shown in figure 2.5, the stiffness that results from the multitude of chemical time-scales is removed from the actual combustion simulation. As a result, larger time-steps can be used which subsequently leads to a drastic speed-up of the simulation.

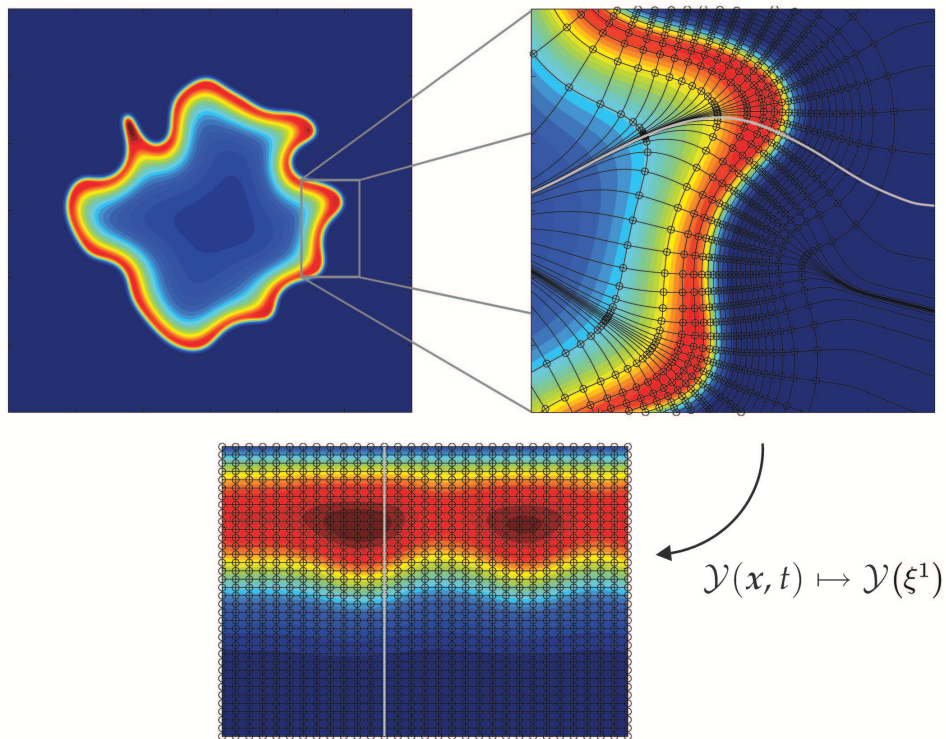


Figure 2.6: Typical example of a freely expanding cylindrical premixed flame. The figure at the top-left shows the species mass fraction of atomic oxygen as a false color plot. A more detailed view can be seen at the top-right, where additionally the curvilinear grid-lines are shown. The principal controlling variable \mathcal{Y} is defined as $\mathcal{Y} = Y_{\text{CO}_2} / Y_{\text{CO}_2}^{\text{burnt}}$. The figure at the bottom shows essentially the same as the one at the top-right, however, now in the transformed curvilinear space. This transformation is indicated by the black arrow marked $\mathcal{Y}(x, t) \mapsto \mathcal{Y}(\xi^1)$. Also shown is a single flamelet, indicated by the grey line in the figures at the top-right and the bottom.

In the cases presented here, see figures 2.6 (bottom) and 2.7 (right), gradients in ξ^1 -direction are generally significantly larger than gradients in ξ^2 -direction. One can thus assume that diffusive transport in the ξ^2 -direction is much smaller than diffusive transport in the ξ^1 -direction. For the set of equations (2.39) - (2.42), which describe the dynamics of the internal flame structure, this means that Q_n and Q_h are small.

Looking again at figures 2.6 (bottom) and 2.7 (right), it can be seen, however, that there are variations in ξ^2 -direction, i.e., the individual flamelet solutions differ from each other. This is mainly caused by varying boundary conditions or local topology variations. This means that all the solutions together form a higher-dimensional manifold. Taking these variations into account, can be done in a way that is very similar to the ILDM method, i.e., by adding more controlling variables, which are generally (combinations of) species mass fractions. The basic assumption of this approach is identical to the assumption that lies at the heart of the ILDM method [52]; that the majority of the reaction trajectories quickly relax onto a low-dimensional manifold of the state space and the closer the system gets to chemical equilibrium the lower the dimension of the manifold becomes.

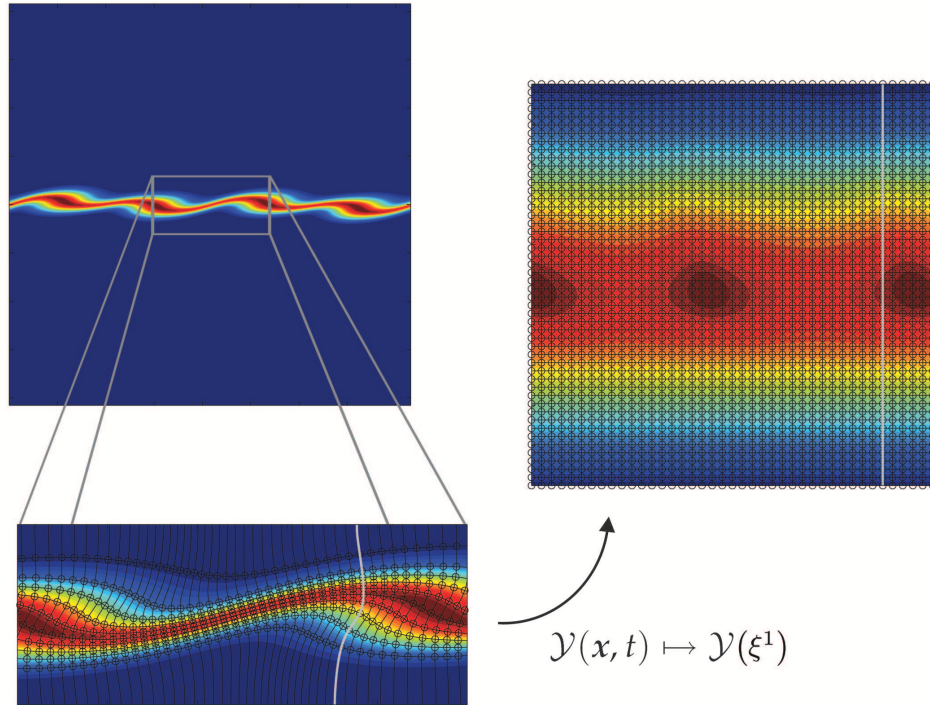


Figure 2.7: Typical example of a non-premixed two-dimensional reacting mixing layer on top of a Kelvin-Helmholtz instability. The figure at the top-left shows the temperature as a false color plot. A more detailed view can be seen at the bottom-left, where additionally the curvilinear grid-lines are shown. The mixture fraction is chosen as the principal controlling variable, i.e., $\mathcal{Y} = Z$. The figure at the right shows essentially the same as the one at the bottom-left, however, now in the transformed curvilinear space. This transformation is indicated by the black arrow marked $\mathcal{Y}(x, t) \mapsto \mathcal{Y}(\xi^1)$. Also shown is a single flamelet, indicated by the grey line in the figures at the bottom-left and the right.

Since the iso-contours of \mathcal{Y} are used to describe the unsteady evolution of the flame front, it is henceforth referred to as the principal controlling variable c_1 . All the other controlling variables are referred to as additional controlling variables c_2, \dots, c_n , where n indicates the total number of controlling variables. Combining the flamelet model with ideas that originated from the chemical reduction methods, resulted in the so-called Flamelet-Generated Manifolds (FGM) method [61]. In the next section, the Flamelet-Generated Manifolds method will be briefly discussed and for more details, the reader is referred to [61].

2.2.2 Generating manifolds

The Flamelet-Generated Manifolds method can be considered as a combination of flamelet models and chemical reduction methods. By simulating one-dimensional flames,

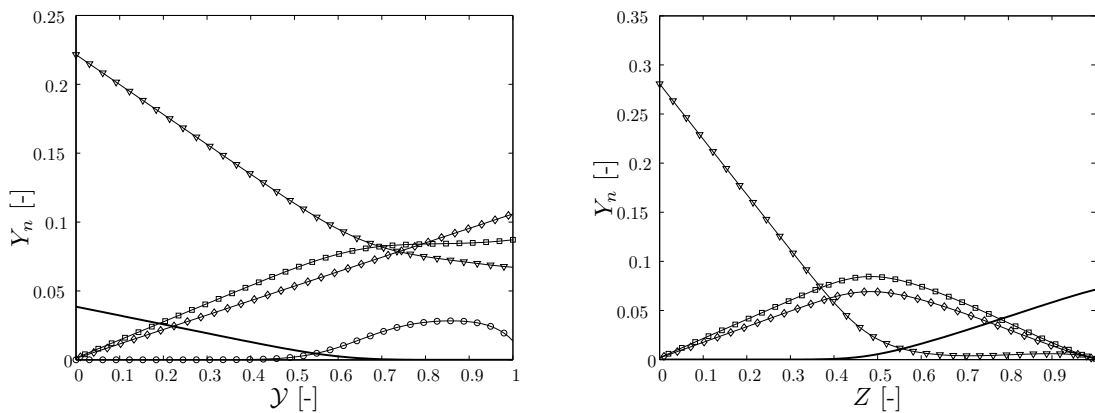


Figure 2.8: Species mass fraction profiles along the two flamelets indicated by the grey lines in figures 2.6 and 2.7, respectively. The figure at the left shows typical premixed species profiles as a function of the principal controlling variable, $\mathcal{Y} = Y_{\text{CO}_2} / Y_{\text{CO}_2}^{\text{burnt}}$ and the figure at the right contains typical non-premixed species profiles as a function of the principal controlling variable, $\mathcal{Y} = Z$. Shown are Y_{CH_4} (solid line), Y_{O_2} (solid line with triangles), Y_{CO_2} (solid line with diamonds), $Y_{\text{H}_2\text{O}}$ (solid line with squares) and Y_{OH} (solid lines with circles - left figure).

i.e., flamelets (2.39) - (2.42), the interaction between important flow-field phenomena and chemistry can be captured. Among these flow-field phenomena are local mixing effects, strain and curvature due to the fluid flow and even local extinction or re-ignition. The major similarity between Flamelet-Generated Manifolds and chemical manifolds is that it is assumed in both approaches, that most of the processes take place within only a small part of the state space. This is called a low-dimensional manifold, which can be parameterized using a small number of controlling variables. Furthermore, by taking more controlling variables into account, the number of time-scales and thus the accuracy of the manifold increases.

Note that during the derivation of the flamelet equations (2.39) - (2.42), no explicit statement has been made, regarding the premixed or non-premixed nature of the flame. In principle, every type of flamelet can be modeled this way. Whether a flamelet can be considered as a premixed or a non-premixed flamelet, strongly depends on the boundary conditions that are imposed on equations (2.45)-(2.48).

A (partially) premixed flamelet forms when the fuel and oxidizer enter at the same side as is the case in figure 2.6. This means that on a molecular scale, the fuel and oxidizer are already mixed when they reach the flame front. This can be modeled by solving (2.39) - (2.42) with appropriate boundary conditions. At the inlet, Dirichlet boundary conditions are imposed, specifying the species mass fractions Y_n , the enthalpy h , the stoichiometry indicated by Z and the local stretch rate K_M . At the outlet on the other hand, Neumann boundary conditions are defined, which state that all the spatial derivatives of the four aforementioned variables are equal to zero. Furthermore, the translational degree of freedom is removed by choosing a fixed temperature T^* at $x_1 = 0$, with $T^* > T_{\text{inlet}}$. Figure 2.8 (left) shows several species mass fractions as a function of the principal controlling variable, $\mathcal{Y} = Y_{\text{CO}_2} / Y_{\text{CO}_2}^{\text{burnt}}$ in this case. Shown are the mass fractions of

methane (solid line), oxygen (solid line with triangles), carbon dioxide (solid line with diamonds), water (solid line with squares) and hydroxyl (solid lines with circles).

When the fuel and oxidizer enter at opposite sides, a non-premixed flamelet forms, see figure 2.7. Simulating a non-premixed flamelet can be done by again solving (2.39) - (2.42). At both the fuel and oxidizer side, Dirichlet boundary conditions are imposed for the species mass fractions Y_n , the enthalpy h and the mixture fraction Z , defining the fuel and oxidizer compositions. Since the local stretch rate K_M only needs to be specified at one side of the domain, a Dirichlet boundary condition needs to be specified at the oxidizer side, while a Neumann boundary condition is imposed at the fuel side of the flame. The latter boundary condition states that the spatial derivative of the local stretch rate is equal to zero at the fuel side. Again, the translational degree of freedom is removed, but now by choosing the stagnation point at $x_1 = 0$, i.e., $u_1(0) = 0$. Figure 2.8 (right) shows several species mass fractions as a function of the principal controlling variable, here $\mathcal{Y} = Z$ is chosen. Shown are the mass fractions of methane (solid line), oxygen (solid line with triangles), carbon dioxide (solid line with diamonds) and water (solid line with squares).

When a steady, flat, adiabatic flame is considered, the temporal and tangential contributions disappear as well as stretch and curvature effects. This means that from (2.39) - (2.42), the following set of differential equations remains:

$$\frac{\partial m}{\partial s} = 0, \quad (2.45)$$

$$\frac{\partial F_y}{\partial s} - \dot{\omega}_y = 0, \quad (2.46)$$

$$\frac{\partial F_n}{\partial s} - \dot{\omega}_n = 0, \quad n \in [1, N_s], \quad (2.47)$$

$$\frac{\partial F_h}{\partial s} = 0. \quad (2.48)$$

The set of differential equations (2.45)-(2.48) can be solved using CHEM1D [14], which results in a one-dimensional trajectory in state space. This trajectory can be considered to be a one-dimensional manifold that can be tabulated as a function of a controlling variable \mathcal{Y} . Increasing the accuracy of the FGM can be done in two distinct ways; 1) by simulating multiple flamelets while varying one or more of the boundary conditions and 2) by taking one or more of the neglected terms of equations (2.39)-(2.42) into account. Which of the boundary conditions should be varied or which of the neglected terms should be taken into account strongly depends on the situation, and must be chosen appropriately. For instance, when it is expected that enthalpy losses play an important role, a 2D FGM can be constructed by simulating a series of steady one-dimensional flamelets, where the enthalpy is varied at the boundaries [64]. On the other hand, when flow straining is thought to be important, it would be wise to include the stretch rate K_M . Over the years a number of papers outlining various ways to apply FGM or FPI has been published.

Steady, flat, unstretched, laminar, premixed flamelets have been used to generate Flamelet-Generated Manifolds [63,64]. In [64], van Oijen et al., generated a 1D manifold

from premixed flamelets. The 1D FGM was compared to a 1D ILDM and it was concluded that both the FGM and the ILDM perform equally well in the high temperature range. In fact, the FGM and ILDM were found to be equivalent in areas where chemistry is dominant. The FGM was validated by performing both a one-dimensional and a two-dimensional test-case. A three-dimensional freely expanding spherical flame embedded in a turbulent flow field was also simulated using a DNS where the combustion chemistry was modeled by using a one-dimensional FGM [63]. It was concluded that the FGM method, using only one controlling variable is able to accurately predict the burning velocity of the flame. However, at high turbulence levels, flame stretch starts to influence the reaction kinetics, resulting in less accurate predictions.

Enthalpy variations have been taken into account as well [30, 64, 81]. In [64], a 2D FGM was generated by simulating a series of premixed flamelets, with constant equivalence ratio but with different enthalpy levels. The 2D FGM was parameterized by $c_1 = Y_{\text{H}_2\text{O}}$ and $c_2 = h$. The mass fraction of H_2O was chosen because it is continuously increasing during the combustion process and therefore satisfying the condition that $\nabla \mathcal{Y} \neq 0$ in the entire domain. Fiorina et al. [30], constructed a 3D FPI table, using the mixture fraction Z , a progress variable c and the enthalpy h to simulate non-adiabatic partially premixed flames. Using these three controlling variables, Fiorina et al., were able to predict the stabilization of the flame due to heat losses on the burner lips very well. In [81], Ribert et al., also included enthalpy losses by simulating burner stabilized premixed flamelets with constant equivalence ratio but with different enthalpy levels. The FPI table was parameterized using two controlling variables, the fuel mass fraction Y_f and the enthalpy h .

Mixture variations and preferential diffusion effects have also been taken into account [11, 31, 32, 65, 66]. For a weakly stretched flame [65], mixture variations and preferential diffusion effects were incorporated into the FGM, where a counterflow premixed flame was modeled. Three cases were considered, i.e., 1) unit Lewis numbers, 2) all Lewis numbers equal to a constant and 3) all Lewis numbers constant but not the same. Since the element mass fractions and the enthalpy are constant in the first case, no additional controlling variable was needed. In the second case, the enthalpy can no longer be considered constant and one additional controlling variable was needed to account for enthalpy variations. Unlike the previous publications [64, 68], in [65] van Oijen et al., opted for species mass fractions only as controlling variables, instead of one species mass fraction and the enthalpy itself as second controlling variable. In the third case, where element mass fractions and enthalpy variations were considered, two controlling variables appeared to be sufficient. This was due to the fact that in the weak stretch case, variations in element mass fractions are strongly coupled to enthalpy variations. The Flamelet-Generated Manifolds method has also been applied to numerically study confined triple flames [66]. In this case, the FGM was extended to not only describe the reaction progress, but also partially premixing. The way the FGM was extended was as follows; a series of purely premixed flamelets was simulated, where the inlet stoichiometry was incrementally changed in order to capture local mixing variations. The reaction progress was again parameterized by \mathcal{Y} and the mixture fraction Z was added as an extra progress variable. It was concluded that there was a good agreement between the results computed with detailed chemistry and the FGM method. A similar approach was used by Bongers et al. [11] and Fiorina et al. [31], where the FGM and FPI methods were applied to simulate a steady, planar, partially premixed [11] and even non-premixed [31],

counterflow flames. The 2D manifolds were generated by simulating premixed flamelets, where again the inlet stoichiometry was incrementally varied. Bongers et al., showed that the FGM method is very capable to model partially premixed flames "efficiently and accurately". Fiorina et al., also concluded that excellent agreement could be obtained using a premixed FPI table to simulate partially premixed and even non-premixed flames.

Non-premixed flamelets can also be used to generate a Flamelet-Generated Manifold, even though it is often assumed that FGM is developed for premixed flames only. However, nowhere it is explicitly stated that non-premixed flamelets cannot be used to generate a Flamelet-Generated Manifold. In fact, in [91], Vreman et al., have constructed two distinct manifolds, i.e., a premixed FGM and a non-premixed FGM, respectively. Both the premixed and the non-premixed manifolds are parameterized by \mathcal{Y} and Z , respectively. Vreman et al., used a linear interpolation to extend the non-premixed FGM beyond the steady extinction limit. Vreman et al., concluded that the premixed FGM covers the non-equilibrium reaction region, which the non-premixed FGM does not.

2.3 Concluding remarks

In this chapter a detailed derivation of a unified flamelet model has been presented. It is a unified flamelet model in the sense that no explicit assumptions have been made regarding the premixed or non-premixed nature. In the unified flamelet model, the flame type is merely a result of the chosen boundary conditions. Furthermore, the original set of equations (1.36)-(1.40) has been decomposed in a natural way into normal and tangential contributions, i.e., (2.39) - (2.42). Often, it is assumed that tangential diffusion, i.e., mass or enthalpy diffusion along the flame front, is small so that it can be neglected. In the next chapter this assumption will be numerically evaluated. The resulting one-dimensional flamelet model can subsequently be used to simulate one-dimensional flames, which can each be considered as one-dimensional manifolds. By simulating one-dimensional flames, a manifold can be constructed, and by adding more controlling variables, the number of time-scales that is incorporated in the manifold can also be increased. In that respect, the application of the FGM method is very similar to the ILDM approach.

Furthermore, it has been shown that Flamelet-Generated Manifolds have been successfully applied in various (complex) combustion simulations. Traditionally the FGM method is automatically associated with premixed flames, however, in principle it is perfectly possible to apply the FGM method also to non-premixed systems as shown by Vreman et al. [91].

In the remainder of this thesis, Flamelet-Generated Manifolds that are based on non-premixed flamelets are studied in detail. But first in chapter 3, the flamelet model that was presented in this chapter is numerically validated by performing a quantitative study to the various neglected terms of the quasi-one-dimensional flamelet equations, i.e., the influence of κ , K_M and Q_n is studied numerically. Additionally, in chapters 4 and 5, it is studied whether unsteady flow-field effects can be successfully incorporated in the Flamelet-Generated Manifolds method.

Eddie Dean explains to Roland Deschain what
he thinks of assuming too much
in *Wolves of the Calla*
by Stephen King

CHAPTER THREE

Numerical evaluation of the flamelet assumptions

In this chapter the species conservation equation is subdivided into several individual contributions, i.e., an unsteady term, normal transport, flame stretch, curvature, tangential diffusion and the chemical production and consumption terms, respectively. Each of these contributions is evaluated numerically using the coordinate transformation that was introduced in the previous chapter. Three different two-dimensional flames are simulated, one premixed flame and two non-premixed flames. Using the numerical results from these detailed flame simulations, the individual contributions of the species conservation equations are computed and compared to each other. Finally, it is concluded which of the individual contributions can be of leading order and which ones may be neglected.

In chapter 2 a unified quasi-one-dimensional flamelet model was presented, which consists of equations (2.39) - (2.42). Often it is assumed that perturbations from one-dimensional behavior are small compared to the normal contributions which means that the steady flamelet model reduces to (2.45)-(2.48). The influence of taking these perturbations from one-dimensional behavior into account (or neglecting them) has been studied in various publications [18,34,37,61]. In [34,37,61], the influence of flame stretch and curvature has been studied for several flames; the tip of a two-dimensional steady bunsen flame [34], steady counterflow flames [61] and spherical and cylindrical premixed flames [37]. Consul et al. [18], analyzed the application of the 'classical' flamelet model based on the mixture fraction Z and the scalar dissipation rate χ . Five different levels of premixing are considered, ranging from fully premixed to pure non-premixed. However, the major difference between this study and previous work, is that tangential diffusion effects are also explicitly considered.

In this chapter these assumptions are numerically evaluated for three different flame simulations, i.e., one premixed flame and two non-premixed flames. The fact that (partially) premixed flames as well as non-premixed flames can be analyzed using the flamelet model (2.39) - (2.42) that was introduced in chapter 2, further illustrates the

unified character of that model. It should be noted that all three flames that are simulated are two-dimensional flames.

The first flame is a freely expanding premixed flame embedded in a turbulent flow field. Similar flames have been simulated and analyzed by van Oijen et al. [62]. The second flame is a reacting mixing layer [6, 92], where a simple one-step chemistry model is used to describe the chemical reactions. In the third simulation, a laminar co-flow flame is simulated. For the premixed flame, the primary controlling variable is defined as $\mathcal{Y} = Y_{\text{CO}_2}/Y_{\text{CO}_2}^{\text{burnt}}$. Whereas, for both latter flames, a different primary controlling variable is chosen. As is common for non-premixed flames, the mixture fraction was introduced as primary controlling variable, i.e., $\mathcal{Y} = Z$.

In order to evaluate the flamelet assumption, the various contributions of the transformed species conservation equation (2.41) are compared to each other. For convenience the transformed species conservation equation is reformulated as follows:

$$\rho \frac{\partial Y_n}{\partial \tau} = \sum_{i=1}^6 T_{n,i}, \quad (3.1)$$

with $T_{n,i}$ the various contributions in the conservation equation that are considered:

$$T_{n,1} = -\frac{\partial F_n}{\partial s}, \quad (3.2)$$

$$T_{n,2} = -\rho K_M Y_n, \quad (3.3)$$

$$T_{n,3} = F_n \kappa, \quad (3.4)$$

$$T_{n,4} = Q_n, \quad (3.5)$$

$$T_{n,5} = \dot{\omega}_n^+, \quad (3.6)$$

$$T_{n,6} = \dot{\omega}_n^-. \quad (3.7)$$

Thus, $T_{n,1}$ represents normal transport (both convective and diffusive), $T_{n,2}$ is the stretch contribution, $T_{n,3}$ represents curvature, $T_{n,4}$ tangential diffusion and $T_{n,5}$ and $T_{n,6}$ the chemical production and consumption, respectively. The postprocessing procedure to compute each of these contributions will be presented in section 3.1. Following that, in section 3.2.1 the unsteady, premixed test case is presented followed by the two non-premixed flames.

3.1 Postprocessing procedure

The individual contributions $T_{n,i}$ are computed in a postprocessing step. In general, the curvilinear mesh points do not coincide with the original Cartesian mesh points. This means that the first and second order derivatives of (3.2)-(3.7) have to be computed on interpolated mesh points, which may lead to numerical artifacts. To avoid this, instead of actually computing the derivatives of equations (3.2)-(3.7) with respect to the transformed coordinate system, the curvilinear derivatives are reformulated in terms of

the original Cartesian coordinates, by applying the chain-rule as follows:

$$\frac{\partial A}{\partial \xi^i} = \frac{\partial x_j}{\partial \xi^i} \frac{\partial A}{\partial x_j} = h_{\xi^i} \mathbf{e}_i \cdot \frac{\partial A}{\partial \mathbf{x}}, \quad (3.8)$$

which is basically the projection of the Cartesian derivative $\frac{\partial A}{\partial \mathbf{x}}$ onto the curvilinear basis vectors \mathbf{a}_i . The following is also true:

$$\frac{\partial A}{\partial s} = \frac{1}{h_{\xi^1}} \frac{\partial A}{\partial \xi^1} = \mathbf{e}_1 \cdot \frac{\partial A}{\partial \mathbf{x}},$$

and similarly:

$$\frac{1}{h_{\xi^2}} \frac{\partial A}{\partial \xi^2} = \mathbf{e}_2 \cdot \frac{\partial A}{\partial \mathbf{x}}.$$

This means that the individual contributions $T_{n,i}$ can be written as below¹:

$$T_{n,1} = -\mathbf{e}_1 \cdot \frac{\partial}{\partial \mathbf{x}} \left(mY_n - \rho D_n \mathbf{e}_1 \cdot \frac{\partial Y_n}{\partial \mathbf{x}} \right), \quad (3.9)$$

$$T_{n,2} = -m\kappa Y_n + \mathbf{e}_1 \cdot \frac{\partial m}{\partial \mathbf{x}} Y_n, \quad (3.10)$$

$$T_{n,3} = \left(mY_n - \rho D_n \mathbf{e}_1 \cdot \frac{\partial Y_n}{\partial \mathbf{x}} \right) \kappa, \quad (3.11)$$

$$T_{n,4} = \mathbf{e}_2 \cdot \frac{\partial}{\partial \mathbf{x}} \left(\rho D_n \mathbf{e}_2 \cdot \frac{\partial Y_n}{\partial \mathbf{x}} \right) - \rho D_n \mathbf{e}_2 \cdot \frac{\partial Y_n}{\partial \mathbf{x}} \nabla \cdot \mathbf{t}, \quad (3.12)$$

$$T_{n,5} = \dot{\omega}_n^+, \quad (3.13)$$

$$T_{n,6} = \dot{\omega}_n^-, \quad (3.14)$$

where $\nabla \cdot \mathbf{t}$ can be considered as a curvature contribution due to local variations in flame front thickness [55]. The tangential vector \mathbf{t} in (3.12) is defined as follows:

$$\mathbf{t} = -\frac{\mathbf{a}^2}{|\mathbf{a}^2|}. \quad (3.15)$$

Since the mass consumption rate m is an important parameter in (3.9) - (3.11), it is also reformulated as follows:

$$m = h_{\xi^1} \dot{\omega}_y - \rho D_y \kappa + h_{\xi^1} \mathbf{e}_1 \cdot \frac{\partial}{\partial \mathbf{x}} (\rho D_y |\nabla \mathcal{Y}|), \quad (3.16)$$

where (2.22), (2.32) and (3.8) were used to reformulate (2.11).

Now the actual procedure to compute all the individual contributions $T_{n,i}$ is outlined. First the scalar fields of all species, temperature and density have to be retrieved from the simulation. Following that, the scalar field of the primary controlling variable is computed. As mentioned, for the premixed flame the primary controlling variable is

¹For a step-by-step derivation the reader is referred to Appendix C.

defined as $\mathcal{Y} = Y_{\text{CO}_2}/Y_{\text{CO}_2}^{\text{burnt}}$, while for the two non-premixed flames, the mixture fraction is chosen as the primary controlling variable, $\mathcal{Y} = Z$.

The mixture fraction is defined as follows, cf. [9]:

$$Z = \frac{Z^* - Z_{\text{ox}}^*}{Z_{\text{fu}}^* - Z_{\text{ox}}^*}, \quad (3.17)$$

where the subscripts "ox" and "fu", indicate the oxidizer and fuel stream respectively. Furthermore, Z^* is a specific linear combination of the element mass fractions Z_j , i.e.,:

$$Z^* = \frac{2}{M_C}Z_C + \frac{1}{2M_H}Z_H - \frac{1}{M_O}Z_O, \quad (3.18)$$

with M_C , M_H and M_O the molar masses of atomic carbon, hydrogen and oxygen, respectively.

The next step is to determine the first contravariant basis vector \mathbf{a}^1 as follows:

$$\mathbf{a}^1 = \nabla \mathcal{Y}. \quad (3.19)$$

The first covariant scale-factor is defined as follows:

$$h_{\xi^1} = |\mathbf{a}_1| = \frac{1}{|\mathbf{a}^1|}. \quad (3.20)$$

Subsequently, the unit vector \mathbf{e}_1 is computed by normalizing \mathbf{a}^1 and following that, the second unit vector \mathbf{e}_2 follows from $\mathbf{e}_1 \cdot \mathbf{e}_2 = 0$, thereby spanning an orthogonal flame-adapted coordinate system. The diffusion coefficients are computed using equations (1.24) and (1.25).

Finally, the flamelets along which the individual contributions $T_{n,i}$ will be evaluated have to be reconstructed. These flamelet paths $\mathbf{x}(s)$ are extracted from the two-dimensional flame simulations by integrating in the normal direction as follows:

$$\mathbf{x}^+(s) = \mathbf{x}_0 + \int_{\mathbf{x}_0}^{\mathbf{x}_\infty} \mathbf{n} ds, \quad (3.21)$$

$$\mathbf{x}^-(s) = \mathbf{x}_0 - \int_{\mathbf{x}_0}^{\mathbf{x}_{-\infty}} \mathbf{n} ds, \quad (3.22)$$

with \mathbf{x}_0 the initial coordinates located at a certain iso-contour and where the normal vector \mathbf{n} is given by (2.4). Furthermore, \mathbf{x}_∞ and $\mathbf{x}_{-\infty}$ represent the coordinates that mark the edges of the flamelet in positive and negative direction, respectively. Starting at specific iso-contours defining these edges, i.e., \mathcal{Y}^- and \mathcal{Y}^+ , the flamelet paths are integrated in both positive and negative normal direction. For the premixed flame, \mathbf{x}_0 is located where $\mathcal{Y} = 0.5$, while for the two non-premixed flames, \mathbf{x}_0 is situated at the stoichiometric iso-contour of the mixture fraction, i.e., where $\mathcal{Y} = Z_{\text{st}}$.

3.2 Numerical simulations

In this section three different combustion simulations are presented. For each of the three simulations, a flamelet analysis is performed in a postprocessing step in order to assess the assumptions already discussed in section 2.2.2. The goal of this chapter is to numerically determine the order of magnitude of each contribution of (2.41).

The following sections, corresponding to the three combustion simulations, are identical in structure; first the numerical approach is outlined, followed by the numerical results of the flamelet analysis.

3.2.1 Freely expanding two-dimensional premixed flame

Simulation setup

A cylindrically expanding, premixed, turbulent flame is used as a first test case to evaluate the flamelet assumptions. The flame considered is a lean premixed methane-air flame with an equivalence ratio of $\varphi = 0.7$. The combustion takes place at atmospheric pressure and the unburnt temperature is $T_u = 300$ K. This flame is very similar to spherically expanding, premixed, turbulent flames as described in [62, 67]. The biggest difference however, is that here detailed chemical kinetics were used as opposed to a 1D FGM in the previous studies. Figure 3.1 shows the simulation setup, as well as the boundary conditions.

[Numerical method] Conservation of mass, momentum, species mass and enthalpy is taken into account by solving equations (1.36)-(1.40) on a square two-dimensional grid of 12×12 mm² and 449×449 grid points. The spatial derivatives are computed using a sixth order compact spatial discretization scheme [50] and the time-integration uses a third order low storage Runge-Kutta scheme [94].

[Boundary conditions] All boundaries are implemented using the Navier-Stokes Characteristic Boundary Conditions (NSCBC) approach [77]. In this case all boundaries are modeled as non-reflecting outlet, which ensures that there is no pressure build-up. The turbulent parameters are $u'/U^0 = 4$ and $l_T/\delta_f = 2$, with u' the turbulent velocity fluctuations, U^0 the displacement speed² of a flat non-stretched flame, l_T the turbulent length-scale and δ_f the laminar flame thickness. Here, the laminar flame thickness δ_f is based on the maximum gradient of the temperature and is defined as follows:

$$\delta_f = \frac{T_{\max} - T_{\min}}{(dT/ds)|_{T_{il}}}, \quad (3.23)$$

where the subscript il denotes the inner layer. Using these parameters, the turbulent Reynolds number equals $Re_t = u'l_T/U^0\delta_f = 8$.

²For premixed flames, as is the case here, U^0 is simply the displacement speed S_d .

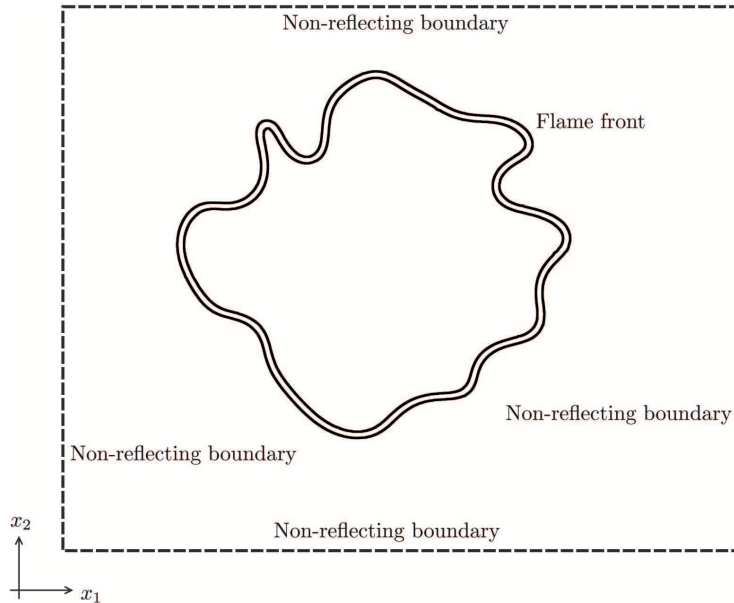


Figure 3.1: Freely expanding two-dimensional premixed flame. Shown are the flame front for $t < t_0$ as well as the type of boundary conditions that are imposed.

[Initial conditions] At $t = 0$ s the flame is initialized by a detailed solution of a one-dimensional, freely expanding, premixed laminar flame, simulated with the one-dimensional flame solver CHEM1D [14]. The radius of the initially circle-shaped flame is 3 mm at $T = 1500$ K. The initial field is superimposed onto a homogeneous and isotropic turbulent flow-field.

[Chemistry and transport models] The chemistry is described by the GRI 3.0 reaction mechanism [84], but ignoring all NO chemistry. A Fickian diffusion model is employed, assuming different but constant Lewis numbers for all species, i.e., $Le_n = \text{constant}$.

A typical result can be seen in figure 3.2, where the turbulent velocity field is shown as vectors. The thick solid lines represent the iso-lines where the local value of the heat release is 50% of its maximum and this indicates roughly where the reaction layer is. The thin solid line indicates another iso-line of the heat release, i.e., it indicates the iso-line \mathcal{Y}^+ where the local value of the heat release is only 5% of its maximum at the burnt side of the flame. Note that there still is a significant area behind the reaction layer where chemistry takes place. This is caused by the slow processes that dominate the last part of the reaction progress in phase space. The thick dashed line finally, represents the isotherm \mathcal{Y}^- that marks the unburnt side of the flame, i.e, $T = 305$ K. As previous studies have shown [62, 67], these type of flames are strongly stretched and curved. It is therefore expected that the stretch and curvature contributions, i.e., $T_{n,2}$ and $T_{n,3}$, will be significant.

An important validation of the numerical postprocessing algorithm as outlined in section 3.1, is to check whether the diffusion term $\nabla \cdot (\rho D_n \nabla Y_n)$ computed in terms of both the Cartesian and the curvilinear derivative operators, are actually the same. The

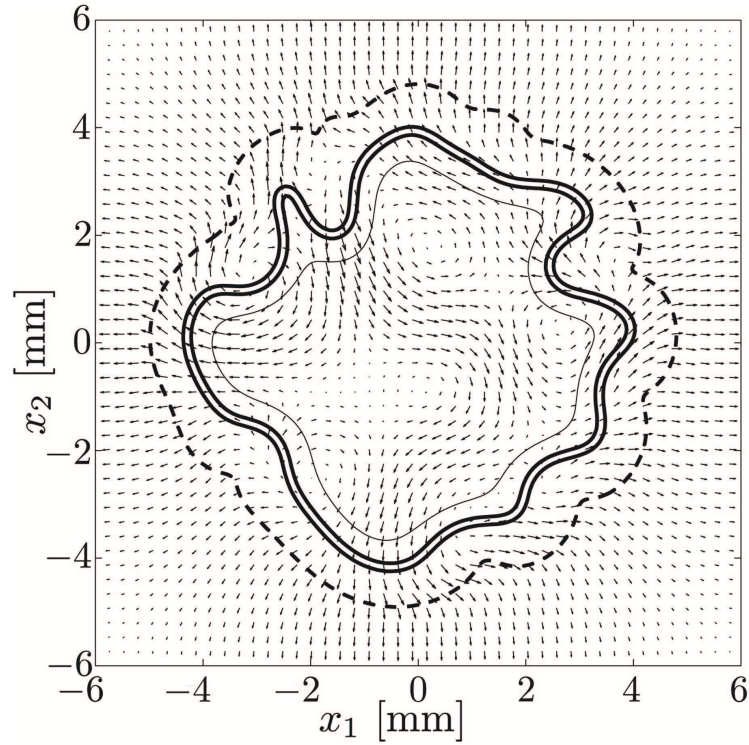


Figure 3.2: Typical result of a freely expanding two-dimensional premixed flame. The vectors represents the turbulent velocity field. The thick solid lines represent the iso-lines where the local value of the heat release is 50% of its maximum, indicating where the reaction layer is. The thin solid line indicates the iso-line \mathcal{Y}^+ which marks the burnt side of the flame. The thick dashed line finally, represents the isotherm \mathcal{Y}^- that marks the unburnt side of the flame.

total diffusion term computed in terms of the Cartesian derivative operators is as follows:

$$-\nabla \cdot (\rho D_n \nabla Y_n) = -\frac{\partial}{\partial x_1} \cdot \left(\rho D_n \frac{\partial Y_n}{\partial x_1} \right) - \frac{\partial}{\partial x_2} \cdot \left(\rho D_n \frac{\partial Y_n}{\partial x_2} \right), \quad (3.24)$$

and the total diffusion term computed in terms of the curvilinear derivative operators:

$$\begin{aligned} -\nabla \cdot (\rho D_n \nabla Y_n) &= -\frac{1}{\sqrt{g}} \frac{\partial}{\partial \xi^1} \cdot \left(\rho D_n \sqrt{g} g^{11} \frac{\partial Y_n}{\partial \xi^1} \right), \\ &\quad -\frac{1}{\sqrt{g}} \frac{\partial}{\partial \xi^2} \cdot \left(\rho D_n \sqrt{g} g^{22} \frac{\partial Y_n}{\partial \xi^2} \right). \end{aligned} \quad (3.25)$$

Since the total diffusion term is invariant to the frame of reference, it should not matter whether it is computed using (3.24), the Cartesian derivative operators or (3.25), the curvilinear derivative operators.

For the freely expanding flame, the total diffusion was computed using both (3.24) and

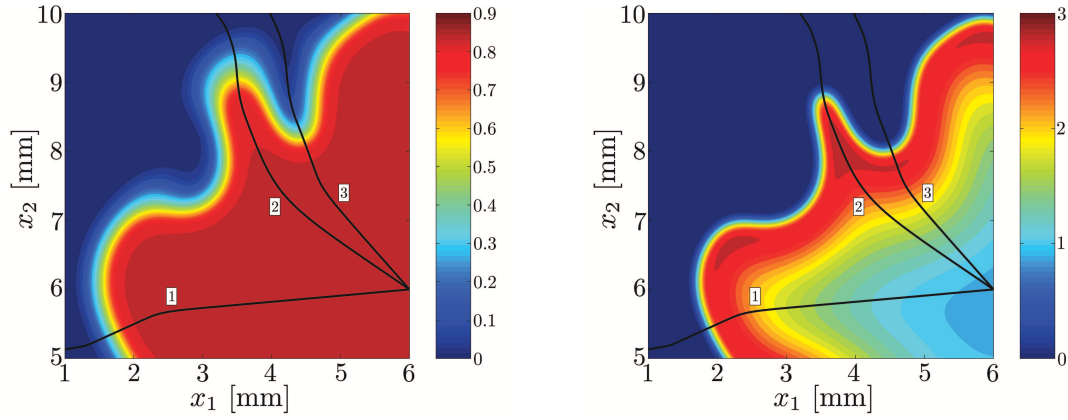


Figure 3.3: Typical results of a freely expanding premixed flame embedded in a turbulent flow (see section 3.2.1). Shown here is a small section of $Y_{\text{H}_2\text{O}} \times 10$ (left) and $Y_{\text{OH}} \times 10^3$ (right). The black lines correspond to three different flamelets.

(3.25), and the maximum difference that was found was about 10% of the total diffusion term. In general however, the difference was a lot smaller and it can be concluded that there are no significant numerical artifacts caused by the coordinate transformation. This is of course as it should be.

Results

A small section of a freely expanding premixed flame that is embedded in a turbulent flow is shown in figure 3.3. The figure at the left shows $Y_{\text{H}_2\text{O}} \times 10$ and the figure at the right shows $Y_{\text{OH}} \times 10^3$. Also shown are three flamelet trajectories, which were reconstructed using (3.21) and (3.22).

Figure 3.4 shows profiles along the three flamelets that were shown in figure 3.3. Shown in figure 3.4 are the temperature T (top-left), the mass consumption rate m (top-right), the mass fraction of water $Y_{\text{H}_2\text{O}}$ (bottom-left) and the species mass fraction of hydroxyl Y_{OH} (bottom-right). The three lines in each figure correspond to the three flamelets as indicated in figure 3.3. The arc length s is scaled with the flame thickness δ_f , which again follows from (3.23).

Figure 3.5 shows the scaled individual contributions $\tilde{T}_{n,i}$ for H_2O (left column) and for OH (right column) along the three flamelet paths $x(s)$ as indicated in figure 3.3 (left). All the contributions are scaled as follows:

$$\tilde{T}_{n,i} = T_{n,i} / \sum_{i=1}^6 |T_{n,i}|_{\max}. \quad (3.26)$$

The top row in figure 3.5 corresponds to the flamelet labeled "1", the middle row is the flamelet labeled "2" and the bottom row is flamelet "3". The dots in figure 3.5 represent the unsteady term $\rho \frac{\partial Y_n}{\partial \tau}$, the circles with dots the normal transport contribution $\tilde{T}_{n,1}$, the thick

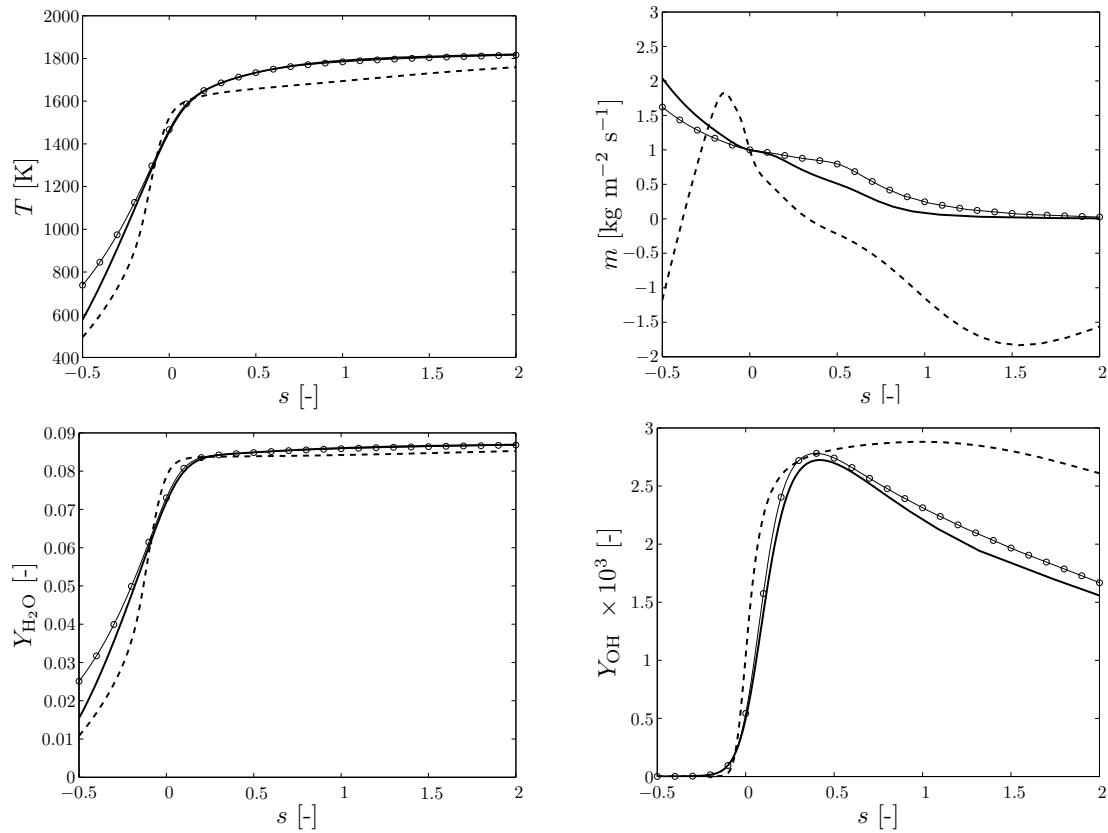


Figure 3.4: Various profiles along three flamelet trajectories. Top-left: Temperature $T(s)$; top-right: mass consumption rate $m(s)$; bottom-left: species mass fraction of water $Y_{\text{H}_2\text{O}}(s)$; bottom-right: species mass fraction of hydroxyl $Y_{\text{OH}}(s)$. The three lines in each figure correspond to the flamelets labeled "1" (thick solid), "2" (thick dashed) and "3" (thin solid with circles) in figure 3.3.

solid lines the stretch contribution $\tilde{T}_{n,2}$, the thin solid lines the curvature contribution $\tilde{T}_{n,3}$, the thick dashed lines the tangential transport contribution $\tilde{T}_{n,4}$, the thin solid lines with squares the chemical production term $\tilde{T}_{n,5}$ and the thin solid lines with diamonds the chemical consumption term $\tilde{T}_{n,6}$, respectively. As can be seen in figure 3.5 (top left), for H_2O the first flamelet shows mainly a balance between the chemical production term, the chemical consumption term and normal transport. A little less dominant are the unsteady term and the stretch rate. Local flame stretch and curvature are much more important for H_2O along the second and third flamelets and for neither of the flamelets, tangential diffusion of H_2O is important. In short, the behavior of H_2O is dependent on all contributions, except tangential diffusion. For OH , it should be noted that the chemical source-terms were multiplied by 10^{-2} , which means that both the chemical production and consumption terms dominate the behavior of OH along all three the flamelets. This means that, although for OH there is a significant tangential diffusion contribution along the second flamelet, it is still negligible compared to the chemical production and consumption contributions. Therefore, it can be concluded that the evolution of OH is dominated by chemistry only.

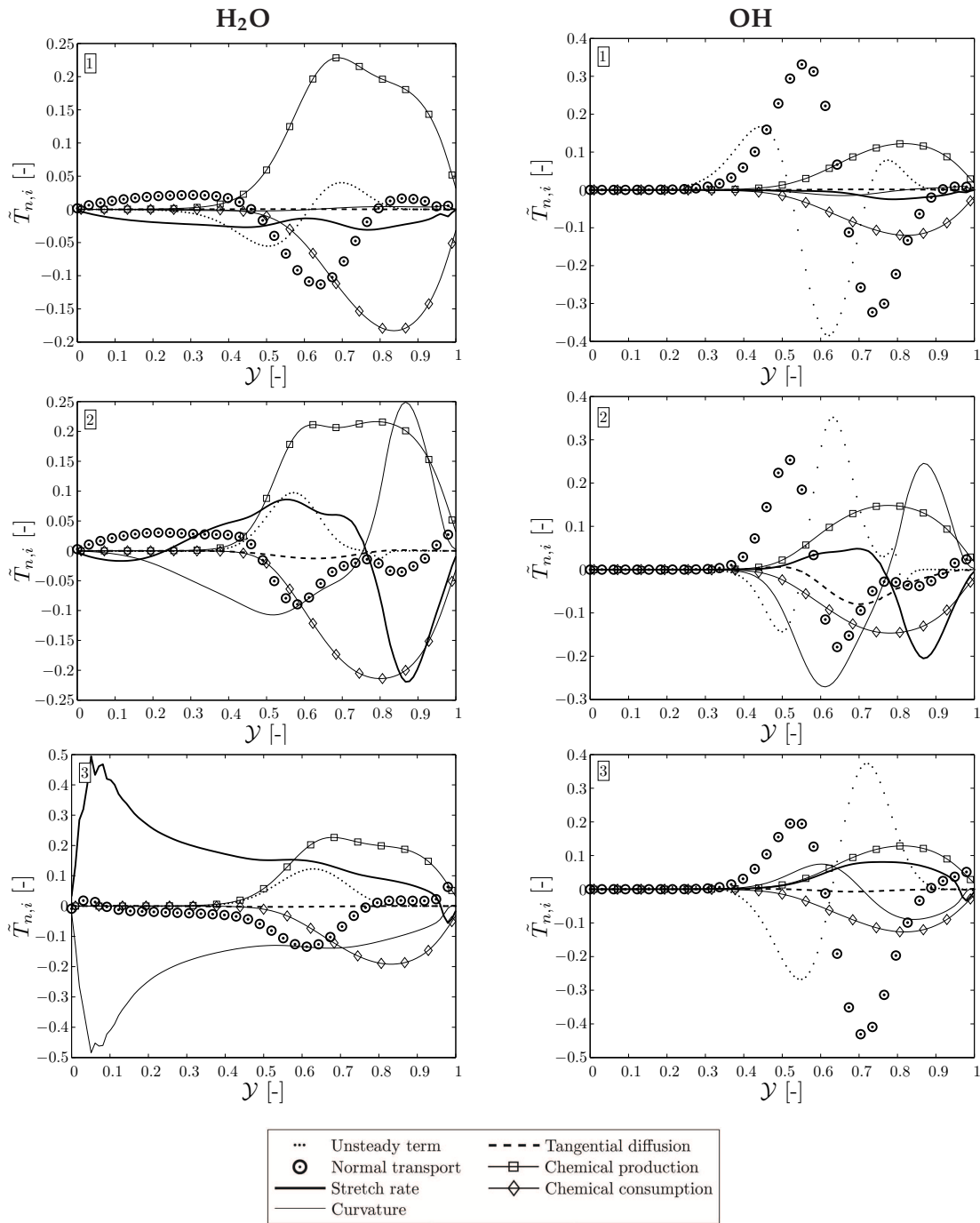


Figure 3.5: The unsteady term $\rho \frac{\partial \gamma_n}{\partial \tau}$ and scaled individual contributions $\tilde{T}_{n,i}$ of the species conservation equation along three different flamelets (see figure 3.3). Here the results are shown for two species, i.e., H₂O (left column) and OH (right column). The top row corresponds to flamelet "1", the middle row to flamelet "2" and the bottom row to flamelet "3". Finally it should be mentioned that the chemical production and consumption terms of OH were multiplied by 10^{-2} .

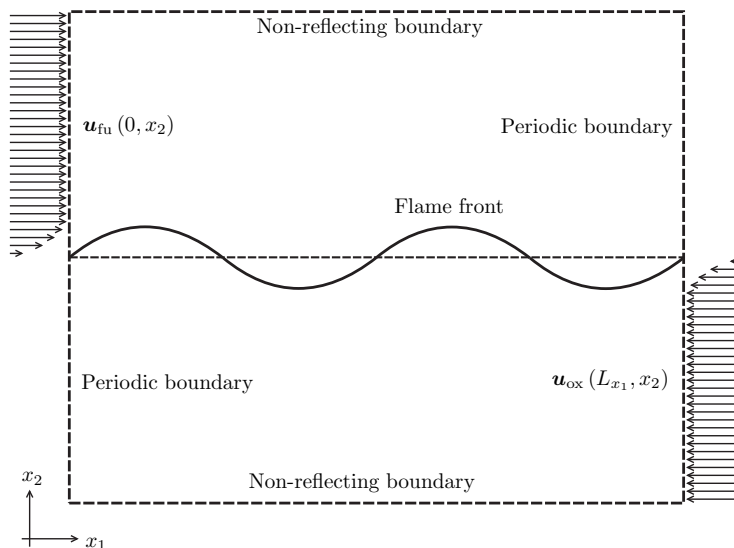


Figure 3.6: Non-premixed reaction mixing layer. Shown are the flame front for $t < t_0$ and the initial velocity profiles for the fuel and the oxidizer streams. Also shown are the type of boundary conditions that are imposed.

3.2.2 Non-premixed reacting mixing Layer

Simulation setup

The second test case is an unsteady, reacting mixing layer [6, 92]. The unsteady mixing layer originates on the interface of two streams with different velocities, resulting in flow shearing at the interface. In this case methane flows from left to right above the interface while oxidizer flows from right to left below the interface, as indicated in figure 3.6. Due to the viscous shearing, a so-called Kelvin-Helmholtz instability arises on the interface.

[Numerical method] Conservation of mass, momentum, species mass and enthalpy is taken into account by solving equations (1.36)-(1.40) on a square two-dimensional grid of $1.67 \times 1.67 \text{ mm}^2$ and 512×513 grid points. The spatial derivatives are computed using a sixth order compact spatial discretization scheme [50] and the time-integration uses a third order low storage Runge-Kutta scheme [94].

[Boundary conditions] The two-dimensional flow domain is periodic in streamwise (x_1) direction, which means that no explicit boundary conditions are needed. The top and bottom boundaries are implemented using the NSCBC approach [77]. In this case the top and bottom boundaries are also modeled as non-reflecting outlet.

[Initial conditions] At $t = 0 \text{ s}$ the flame is initialized by superimposing a reference temperature of $T = 1500 \text{ K}$ and a reference density of $\rho = 1.2 \text{ kg m}^3$, which results in non-atmospheric, non-premixed combustion. The fuel stream is defined as $Y_{\text{CH}_4} = 0.072$ and $Y_{\text{N}_2} = 0.928$, while the oxidizer stream consists of $Y_{\text{O}_2} = 0.287$ and $Y_{\text{N}_2} = 0.713$. This means that the stoichiometric value of the mixture fraction is $Z_{\text{st}} = 0.5$. In [92] the mixing layer is described for a cold non-reactive flow. Both the initial velocity profile in

x_1 -direction as well as the initial profiles for the species are described by a hyperbolic tangent in x_2 -direction. To ensure that the instability develops, a small perturbation term ϵ is added to the initial velocity profile³:

$$u_1 = U_\infty \tanh\left(\frac{2x_2}{\delta}\right) + \epsilon, \quad (3.27)$$

where the vorticity thickness δ can be computed via the Reynolds number, which is defined as follows:

$$\text{Re}_\delta = \frac{\rho_\infty U_\infty \delta / 2}{\mu_\infty}. \quad (3.28)$$

All other parameters that characterize the flow are listed in Appendix D.

[Chemistry and transport models] The chemistry is simulated as a single step chemical reaction, as described by the following global reaction:



where the reaction rate parameters are chosen to be the same as in [7] and are listed in Appendix D. A Fickian diffusion model is employed, assuming unity Lewis numbers for all species, i.e., $\text{Le}_n = 1$.

For the non-premixed, reacting mixing layer, the total diffusion was also computed using both (3.24) and (3.25), and the maximum difference that was found was about 0.5% of the total diffusion term. Therefore it can be concluded that there are no significant numerical artifacts caused by the coordinate transformation.

Results

Figure 3.7 shows some typical results of a non-premixed reacting mixing layer at two different time-intervals, i.e., $t = 2.5 \mu\text{s}$ (top row) and $t = 5.0 \mu\text{s}$ (bottom row). The two figures at the left show $Y_{\text{CO}_2} \times 10$ and the two figures at the right show $T_{\text{CO}_2,1} \times 10^{-5}$, i.e., equation (3.9). Also shown are two flamelet trajectories, which were reconstructed using (3.21) and (3.22).

Figure 3.8 shows profiles along the two flamelets that were shown in figure 3.7. Shown in figure 3.8 are the temperature T (top-left), the mass consumption rate m (top-right), the mass fraction of carbon dioxide Y_{CO_2} (bottom-left) and the species mass fraction of methane Y_{CH_4} (bottom-right). The two lines in each figure correspond to the three flamelets as indicated in figure 3.7. The arc length s is scaled with the flame thickness δ_f , which again follows from (3.23).

For the non-premixed reacting mixing layer, the scaled individual contributions $\tilde{T}_{n,i}$ for CO_2 are shown in figure 3.9, for two different time-intervals, i.e., $t = 2.5 \mu\text{s}$ (left column) and $t = 5.0 \mu\text{s}$ (right column). For both time-intervals, the scaled individual contributions

³The perturbation ϵ is obtained from the cold flow linear stability solution as described in [92].

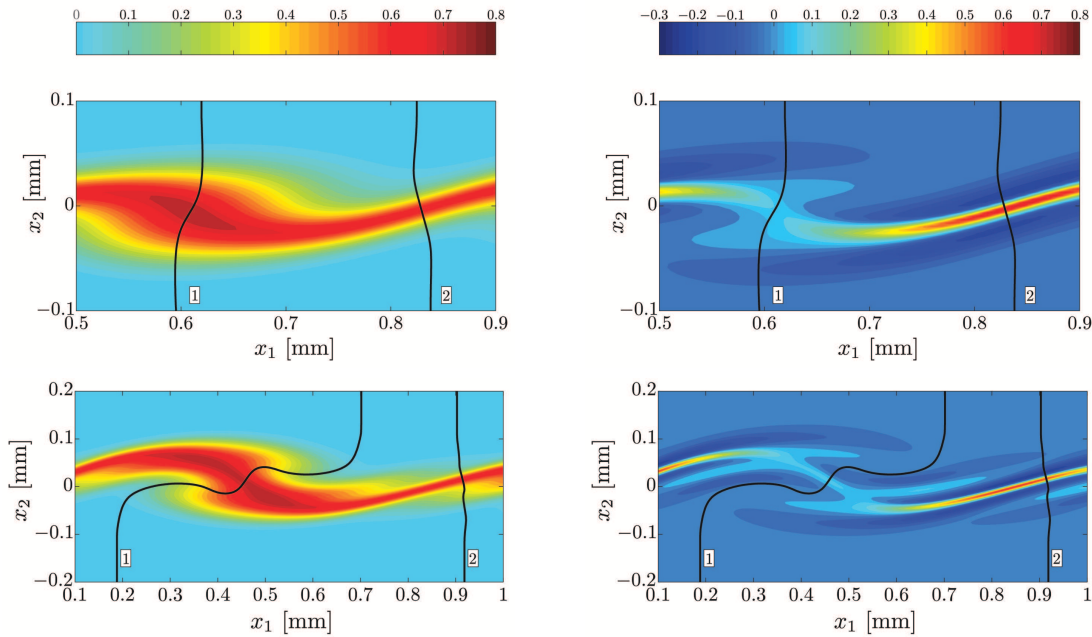


Figure 3.7: Typical results of the reacting mixing layer (see section 3.2.2), at two different time-intervals, i.e., $t = 2.5 \mu\text{s}$ (top-row) and $t = 5.0 \mu\text{s}$ (bottom-row). The left column shows $Y_{\text{CO}_2} \times 10$ and the column at the right shows $T_{\text{CO}_2,1} \times 10^{-5}$ (equation 3.9). The black lines correspond to two different flamelets.

$\tilde{T}_{n,i}$ are shown along two different flamelets, labeled "1" (top row) and "2" (bottom row) in figure 3.7. The dots in figure 3.9 represent the unsteady term $\rho \frac{\partial Y_n}{\partial \tau}$, the circles with dots the normal transport contribution $\tilde{T}_{n,1}$, the thick solid lines the stretch contribution $\tilde{T}_{n,2}$, the thin solid lines the curvature contribution $\tilde{T}_{n,3}$, the thick dashed lines the tangential transport contribution $\tilde{T}_{n,4}$ and the thin solid lines with squares the total chemical source-term $\tilde{T}_{n,5} + \tilde{T}_{n,6}$, respectively⁴.

As can be seen in figure 3.9 (top left), for the first time-interval $t = 2.5 \mu\text{s}$, the two dominant terms are the normal transport and the stretch rate contributions. It is interesting to see that the local value of the chemical source-term is not very large. This is caused by the fact that a pocket of reactants has formed, which is not very reactive anymore. Both curvature as well as tangential diffusive processes do not play a significant role. As can be seen in figure 3.9 (bottom left), chemistry plays a much bigger role along the second flamelet than it did along the first flamelet. The normal transport and the stretch rate contributions are of the same order and together with the unsteady term balance the chemical source-term. Along both flamelets, neither curvature effects nor tangential diffusion has a significant contribution.

The most noticeable difference between the first and the second time interval, is that the curvature contribution as can be seen in figure 3.9 (top right) is more important at $t = 5.0 \mu\text{s}$. The fact that curvature effects are much more significant compared to the previous

⁴Due to the global one-step chemistry model, obviously it is not possible to decompose the chemical source-term in a chemical production and consumption contribution.

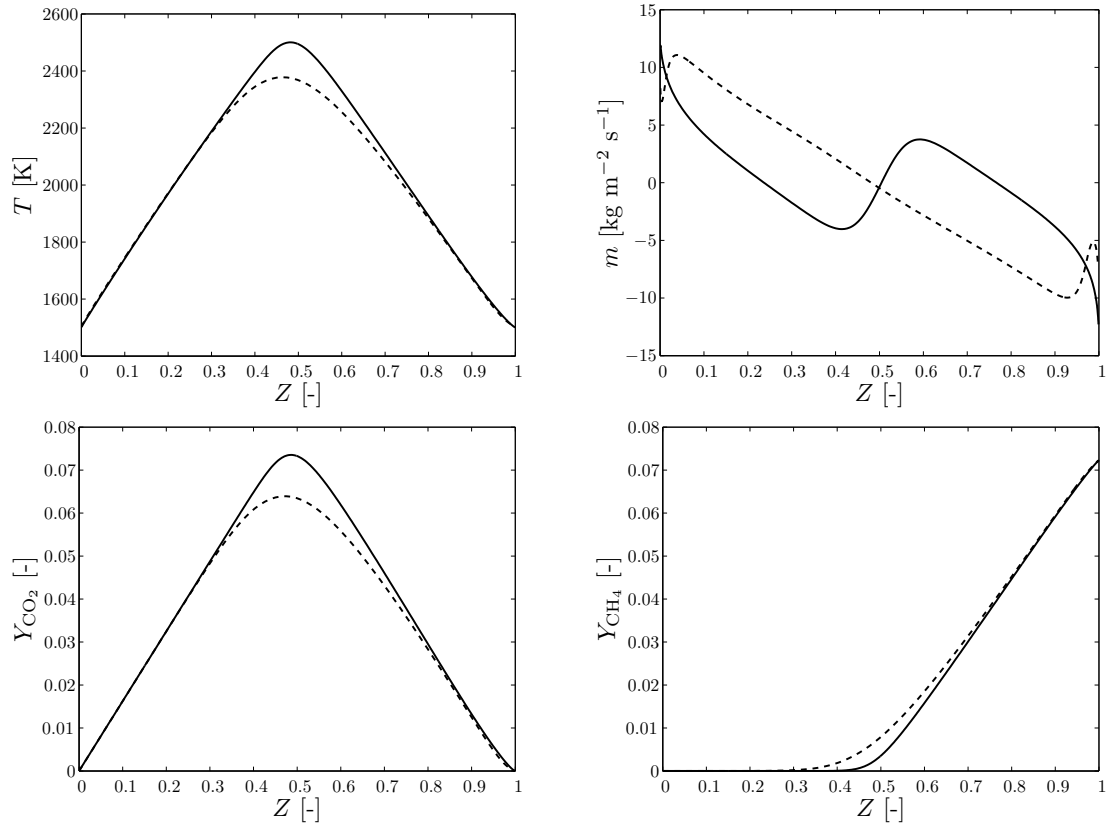


Figure 3.8: Various profiles along two flamelet trajectories. Top-left: Temperature; top-right: mass consumption rate; bottom-left: species mass fraction of carbon dioxide; bottom-right: species mass fraction of methane. The two lines in each figure correspond to the flamelets labeled "1" (thick solid) and "2" (thick dashed) in figure 3.7 (top-left).

time-interval can also be understood by looking at the first one-dimensional flamelet path $x(s)$ in figure 3.7 (bottom-left), which shows that flamelet "1" is much more distorted by the flow than flamelet "1" at the first time interval, i.e., figure 3.7 (top left). For the second flamelet, the curvature contribution is again very small as well as the tangential diffusion contribution, which is very small along both flamelets. In general it can be concluded that for the non-premixed reacting mixing layer tangential diffusion effects can be neglected, while all the other contributions can be of leading order.

3.2.3 Steady non-premixed co-flow flame

Simulation setup

The last flame that is used as a test case is a well documented laminar co-flow flame [8, 17–19]. Here only the most important characteristics are mentioned and for more details, the reader is referred to [8, 17–19]. Figure 3.10 shows the particular burner rotated at an angle of 90 degrees. Additionally, all the important measures are also indicated. The

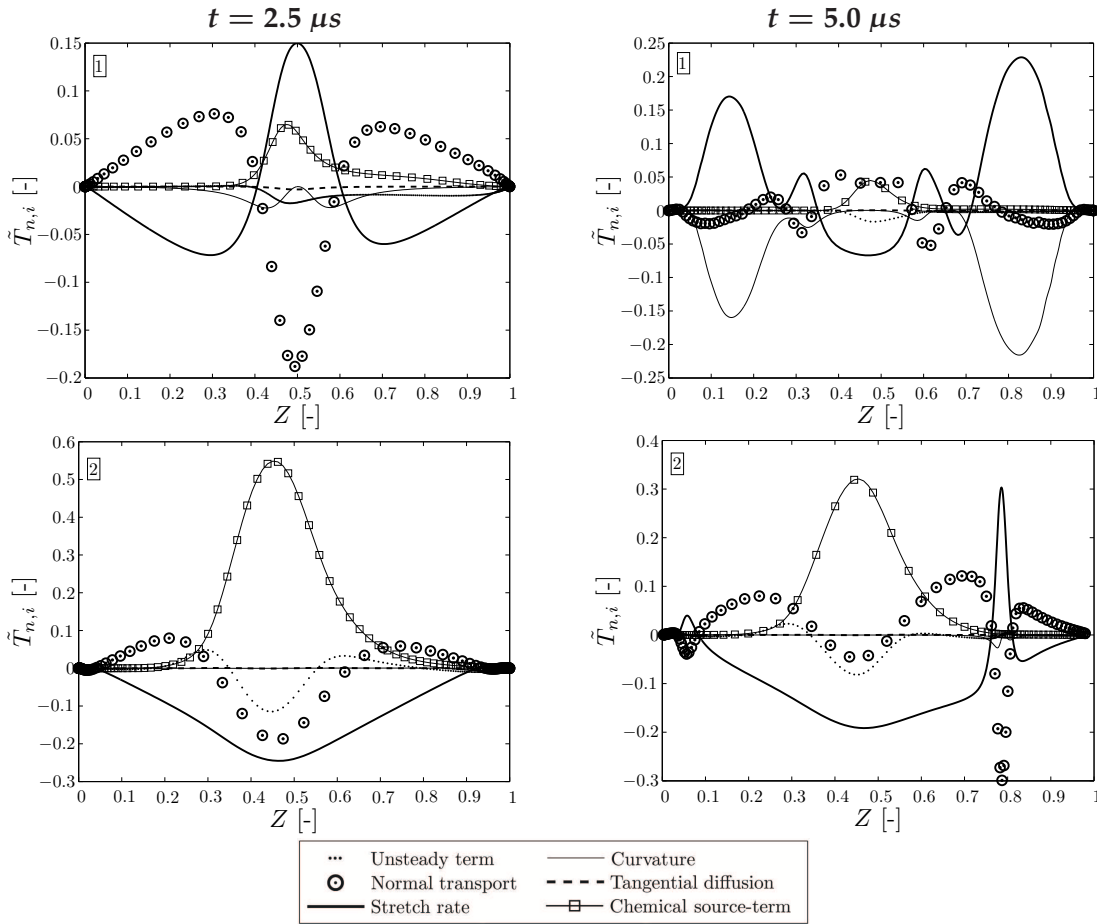


Figure 3.9: Scaled individual contributions $\tilde{T}_{n,i}$ along two flamelet trajectories and at two different time-intervals, i.e., $t = 2.5 \mu\text{s}$ (left column) and $t = 5.0 \mu\text{s}$ (right column). The top row corresponds to the flamelet labeled "1" and the bottom row is flamelet "2" in figure 3.7.

coarse mesh on which the initial simulations are run is shown, as well as two levels of grid-refinement.

[Numerical method] Conservation of mass, momentum, species mass and enthalpy is taken into account by solving equations (1.36)-(1.40) on a rectangular two-dimensional, uniform grid of $47.6 \times 240 \text{ mm}^2$ and 48×241 grid points. This coarse grid is used to compute a first estimate of the steady solution after which it is locally refined. The area of refinement is the area just above the burner rim, i.e., $5 \leq x_1 \leq 10 \text{ mm}$ and $0 \leq x_2 \leq 5 \text{ mm}$. The grid-size of the locally refined mesh is $\Delta x_1 = \Delta x_2 = 0.31 \text{ mm}$. The spatial derivatives are computed using a second order upwind discretization scheme.

[Boundary conditions] The boundary conditions are implemented as shown in figure 3.10. Fuel (methane) flows from the inner tube with a radius of $r_i = 5.55 \text{ mm}$ and a wall thickness of $w_i = 0.8 \text{ mm}$, while oxidizer (air) flows from the outer tube, which has a radius of $r_o = 47.6 \text{ mm}$. The volume flows of methane and oxidizer are $V_{\text{CH}_4} = 5.5 \times 10^{-6} \text{ m}^3 \text{ s}^{-1}$ and $V_{\text{ox}} = 7.33 \times 10^{-4} \text{ m}^3 \text{ s}^{-1}$, respectively.

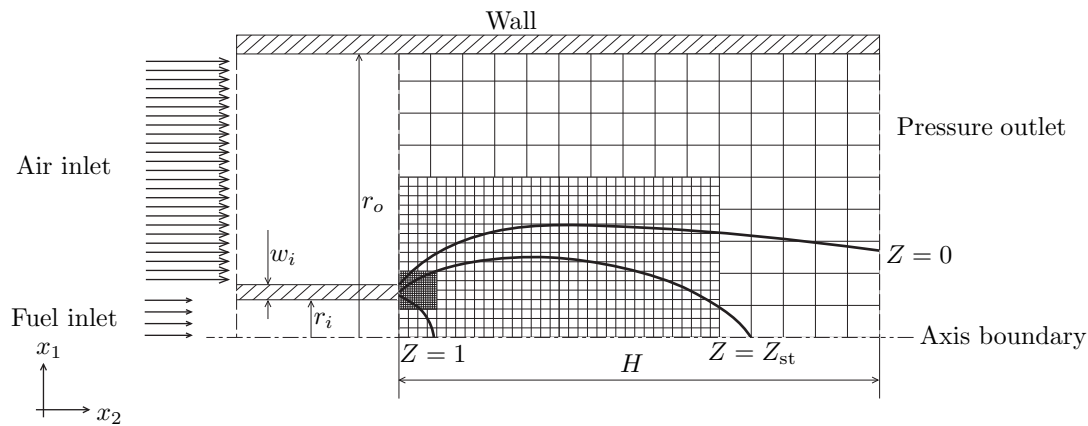


Figure 3.10: Steady non-premixed co-flow flame. Shown are the burner geometry and the inlet velocity profiles for the fuel and oxidizer streams. Also shown are three iso-contours of the mixture fraction as well as the various types of boundary conditions that are imposed.

[Chemistry and transport models] The chemistry is described by the GRI 2.11 reaction mechanism [12]. A Fickian diffusion model is employed, assuming different but constant Lewis numbers for all species, i.e., $Le_n = \text{constant}$.

For the steady non-premixed co-flow flame, the total diffusion was also computed using both (3.24) and (3.25), and the maximum difference that was found (just above the burner rim) was about 10% of the total diffusion term. In general however, the difference was a lot smaller and it can be concluded that there are no significant numerical artifacts caused by the coordinate transformation.

Results

Typical results of a steady non-premixed co-flow flame can be seen in figure 3.11. Shown are $Y_{\text{CO}_2} \times 10$ (left) and $Y_{\text{CH}_3} \times 10^2$ (right). Also shown are three flamelet trajectories, which were reconstructed using (3.21) and (3.22).

Figure 3.12 shows profiles along the three flamelets that were shown in figure 3.11. Shown in figure 3.12 are the temperature T (top-left), the mass consumption rate m (top-right), the mass fraction of carbon dioxide Y_{CO_2} (bottom-left) and the species mass fraction of methane Y_{CH_4} (bottom-right). The three lines in each figure correspond to the three flamelets as indicated in figure 3.11. The arc length s is scaled with the flame thickness δ_f , which again follows from (3.23).

For the steady non-premixed co-flow flame, the scaled individual contributions $\tilde{T}_{n,i}$ are shown in figure 3.13 for H_2O (left column) and CH_3 (right column), respectively. The top row of figure 3.13 shows the profiles along flamelet "1" and the bottom row shows the results along flamelet "2". Only a small region just above the burner rim is considered. Because this is a lifted flame, it is expected that it is exactly this region where the most interesting features can be expected. The circles with dots in figure 3.13 represent the

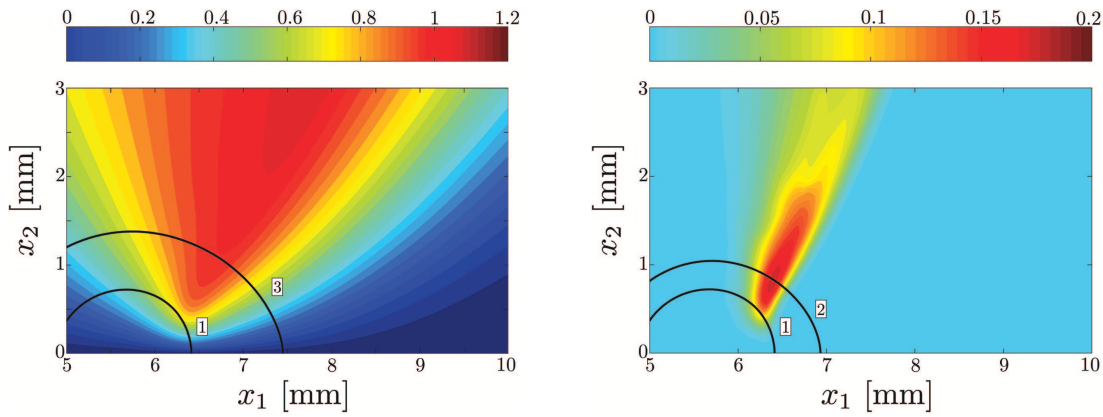


Figure 3.11: Typical result of the steady non-premixed co-flow flame (see section 3.2.3). Shown are $Y_{\text{H}_2\text{O}} \times 10$ (left) and $Y_{\text{CH}_3} \times 10^2$ (right). The black lines correspond to two different flamelets which have been reconstructed using $\mathcal{Y} = Z$ as principal controlling variable.

normal transport contribution $\tilde{T}_{n,1}$, the thick solid lines the stretch contribution $\tilde{T}_{n,2}$, the thin solid lines the curvature contribution $\tilde{T}_{n,3}$, the thick dashed lines the tangential transport contribution $\tilde{T}_{n,4}$, the thin solid lines with squares the chemical production term $\tilde{T}_{n,5}$ and the thin solid lines with diamonds the chemical consumption term $\tilde{T}_{n,6}$, respectively. Note that since this is a steady flame, $\rho \frac{\partial Y_n}{\partial \tau} = 0$ everywhere in the flame and is therefore not shown in figure 3.13.

As can be seen in figure 3.13 (top left), the chemical production and normal transport contributions are the most dominant. The most noticeable difference with the results of the previous two flames, is that the tangential diffusion contribution is now slightly more important. As mentioned, since this is a lifted flame, the iso-lines of the species, H_2O in this case, do not coincide with the iso-lines of the primary controlling variable $\mathcal{Y} = Z$. This means that generally gradients associated with species, ∇Y_n also do not coincide with gradients associated with the principal controlling variable, $\nabla \mathcal{Y}$. This ultimately results in diffusive transport in ξ^2 -direction as can be seen in figure 3.13 (top left). Flamelet "3" (bottom left) shows quite a different picture, i.e., the chemical production and consumption contributions are the most important ones, while the normal transport and stretch contributions also play a less significant role. Tangential diffusion however, almost does not play a role anymore.

Figure 3.13 (right column) shows the results for CH_3 along flamelets "1" and "2", which are very similar to the results for H_2O . One of the advantages of the unified approach is that it is rather straightforward to repeat the above analysis, but instead of using the mixture fraction Z as principal controlling variable, a product species can be chosen as principal controlling variable. In this case the species mass fraction of CO_2 was used, i.e., $\mathcal{Y} = Y_{\text{CO}_2}$. Figure 3.14 shows the species mass fractions of H_2O (left) and CH_3 (right), respectively. Also shown are three flamelets which have been reconstructed using $\mathcal{Y} = Y_{\text{CO}_2}$ as principal controlling variable.

As can be seen in figure 3.15 (left column), the chemical production and consumption contributions for H_2O are the most dominant, which is valid for all the results shown in

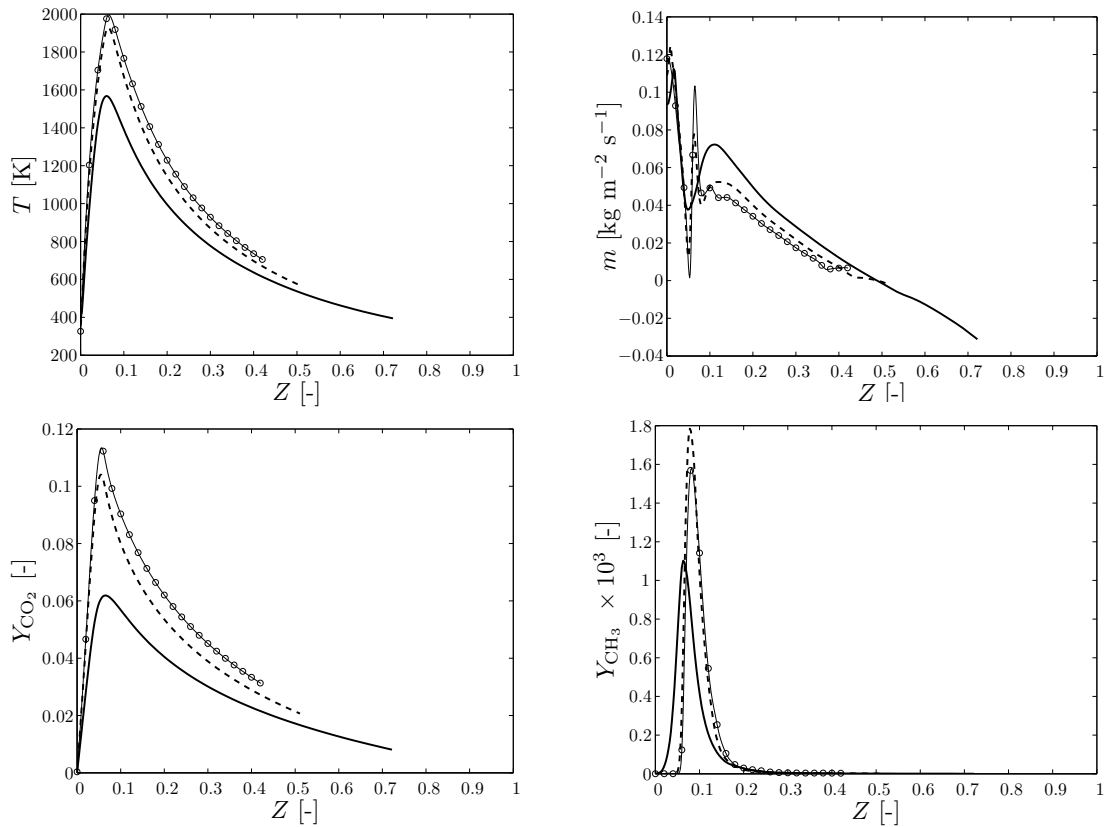


Figure 3.12: Various profiles along three flamelet trajectories. Top-left: Temperature; top-right: mass consumption rate; bottom-left: species mass fraction of CO_2 ; bottom-right: species mass fraction of CH_3 . The three lines in each figure correspond to the flamelets labeled "1" (thick solid) and "2" (thick dashed) in figure 3.11 (right) and "3" (thin solid with circles) in figure 3.11 (left).

figure 3.15. It is interesting to note that for CH_3 , the tangential diffusion contribution is of the same order as was the case with the mixture fraction Z as principal controlling variable. It can therefore be concluded that even for the steady non-premixed co-flow flame, applying two different coordinate transformations, tangential diffusion is negligible.

3.3 Discussion and conclusions

The goal in this chapter was to provide more insight into the several contributions of the species conservation equation. The importance of stretching and curvature for certain types of flames has been the subject of previous studies. Tangential diffusion however, is generally assumed to be negligible. Therefore, in this work, tangential diffusion is also explicitly considered. By applying a flamelet analysis to three different detailed flame simulations, each of the individual contributions of the species conservation equation was numerically verified. These contributions consist of 1) an unsteady term, 2) normal

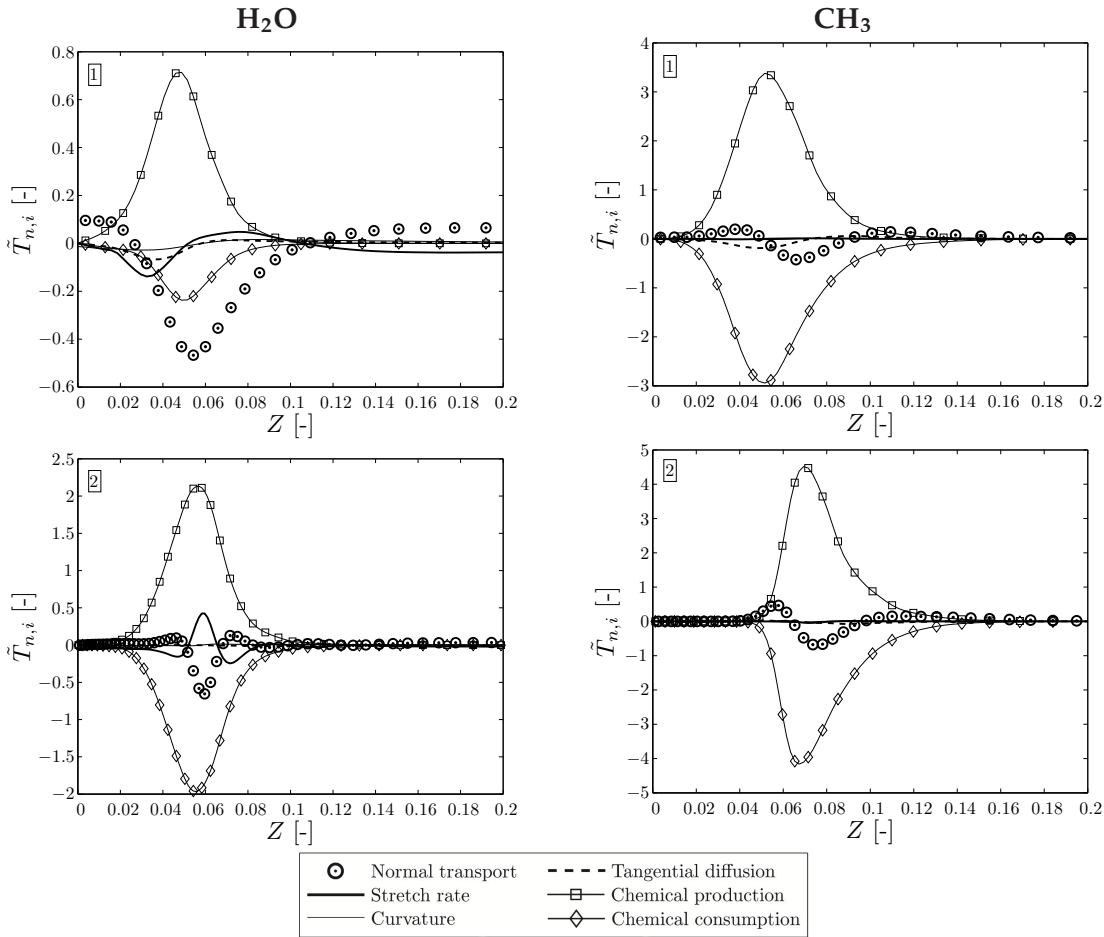


Figure 3.13: Scaled individual contributions $\tilde{T}_{n,i}$ along three flamelet trajectories for $Y_{\text{H}_2\text{O}}$ (left column) and Y_{CH_3} (right column). The top row corresponds to the flamelet labeled "1", the bottom left is flamelet "2" and the bottom right is flamelet "3" in figure 3.11.

transport, 3) stretch-rate effects, 4) curvature effects, 5) tangential diffusion and 6) a chemical source-term, which may be split in a production and a consumption term, respectively.

In order to perform this flamelet analysis, a postprocessing procedure was outlined. Due to the unified nature of the flamelet model that was presented in chapter 2, the postprocessing procedure can be applied to both premixed flames, as well as to non-premixed flames. The only difference between the premixed case and the non-premixed flames is the choice of the principal controlling variable. In the premixed case, a product species was chosen, i.e., $\mathcal{Y} = Y_{\text{CO}_2}/Y_{\text{CO}_2}^{\text{burnt}}$, while in the non-premixed cases the mixture fraction was chosen as primary controlling variable, i.e., $\mathcal{Y} = Z$. Apart from this, the rest of the postprocessing procedure is identical.

Three different flames, one premixed and two non-premixed, were used as test cases to perform a flamelet analysis. The first flame is a freely expanding premixed flame embedded in a decaying turbulent flow-field. As a second test-case a so-called non-premixed reacting mixing layer was used. One of the key features of this mixing layer

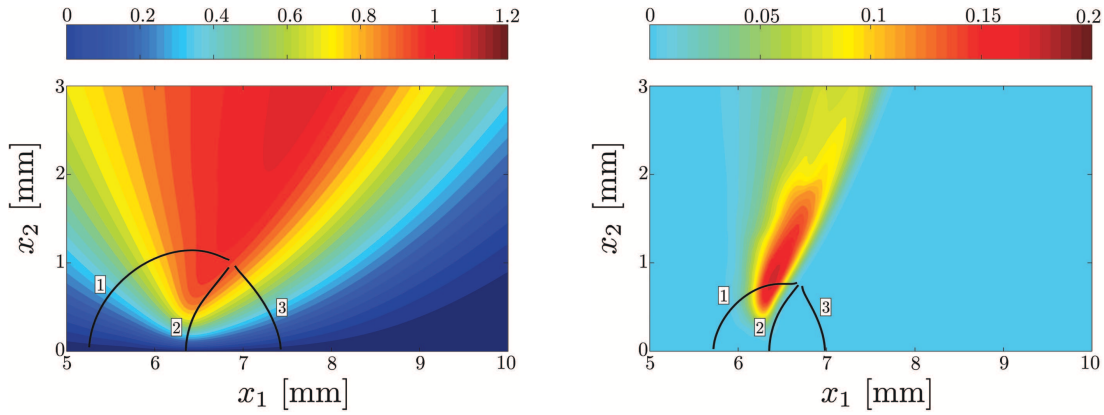


Figure 3.14: Typical result of the steady non-premixed co-flow flame. Shown are $Y_{\text{H}_2\text{O}} \times 10$ (left) and $Y_{\text{CH}_3} \times 10^2$ (right). The black lines correspond to three different flamelets which have been reconstructed using $\mathcal{Y} = Y_{\text{CO}_2}$ as principal controlling variable.

is the Kelvin-Helmholtz instability, which results in a sort of roll-up of the flame, which means that the strain-rate increases as function of time. The last test-case was a steady non-premixed co-flow flame, which is a lifted flame.

For each of the test cases, one-dimensional flamelet paths were reconstructed, along which the scaled individual contributions $\tilde{T}_{n,i}$ were evaluated. In general it can be concluded that of all the contributions to the species conservation equation, tangential diffusion is by far the smallest and neglecting it does not lead to significant inaccuracies. Furthermore, besides normal transport and chemistry, flame stretch and curvature can also be important in both premixed and non-premixed flames and should therefore be taken into account when constructing an FGM. From the two unsteady flame simulations it also follows that the unsteady contribution can be significant and in the next two chapters it will be studied whether or not this unsteady term should be explicitly be incorporated into a Flamelet-Generated Manifold.

Finally, for the laminar co-flow flame, two different principal controlling variables were chosen, resulting in two different coordinate transformations, i.e., a typical non-premixed flame-adapted coordinate system and a typical premixed one. Compared to the coordinate transformation based on the mixture fraction, there are not too many differences. The major difference is of course that the flamelet paths for the latter transformation are much more alike premixed flamelets, while the flamelet paths that were reconstructed using the mixture fraction, look like non-premixed flamelets. The fact that this is possible is a direct result of the unified nature of the flamelet model derived in chapter 2.

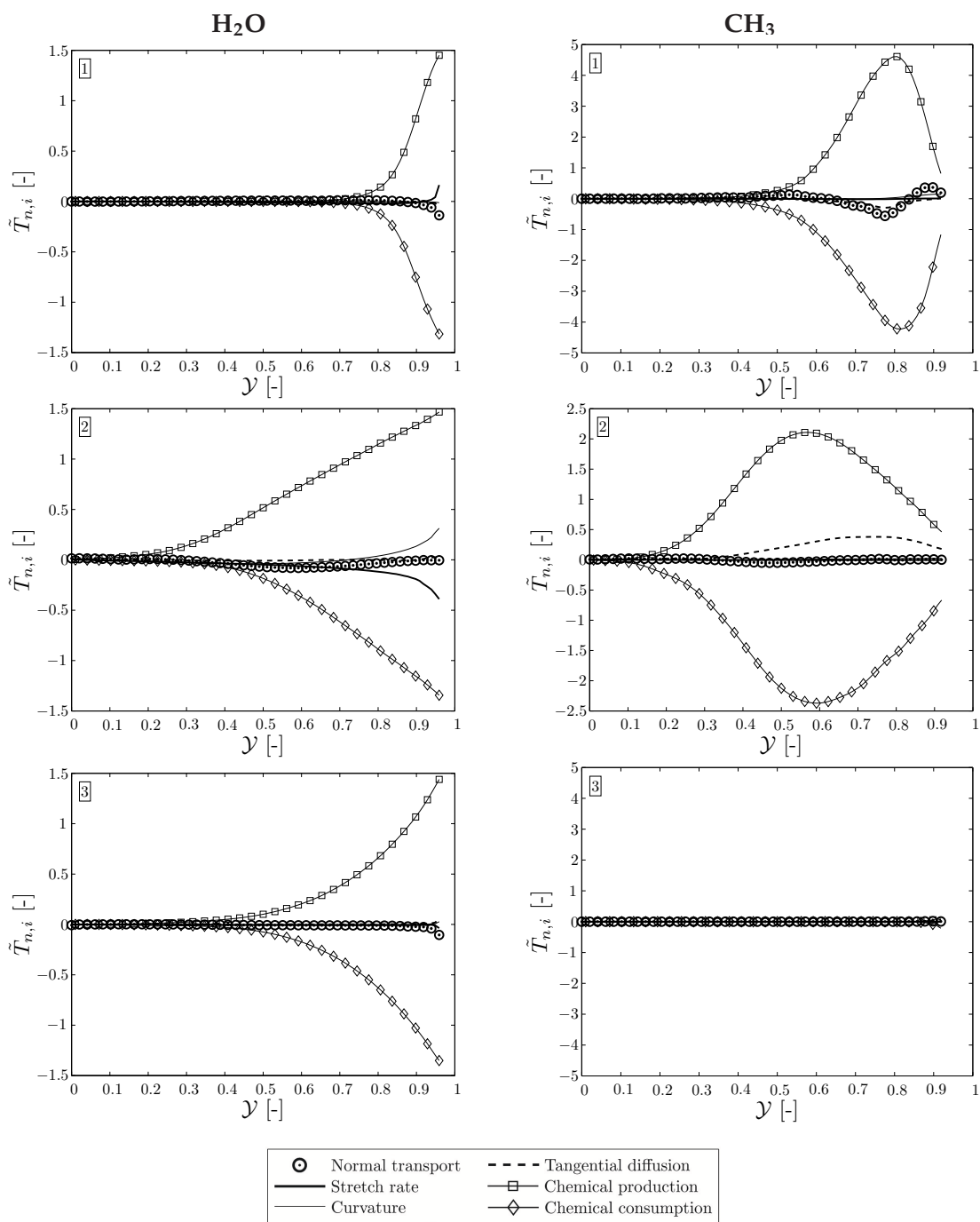


Figure 3.15: Scaled individual contributions $\tilde{T}_{n,i}$ along three flamelet trajectories for $Y_{\text{H}_2\text{O}}$ (left column) and Y_{CH_3} (right column). The top row corresponds to the flamelet labeled "1", the bottom left is flamelet "2" and the bottom right is flamelet "3" in figure 3.11.

CHAPTER FOUR

Incorporating unsteady flow-effects in Flamelet-Generated Manifolds

Detailed simulations are performed for a series of steady and unsteady non-premixed flames. A specific type of unsteady flamelet simulations is considered, i.e., flamelets subjected to (temporally) varying strain-rates. It is observed that the unsteady flame trajectories move closely along a 2D manifold, describing the set of steady diffusion flames in composition space. Using the 2D manifold, unsteady simulations are performed. It is shown that there is a phase-shift in the species mass-fractions between the detailed simulations and the 2D FGM simulations. This phase-shift can be avoided when an additional controlling variable is used. Using unsteady flamelet simulations, a 3D manifold is generated, which is parameterized using three controlling variables. Furthermore, this 3D FGM accurately predicts a broad range of the strain-rate parameters, i.e., mean strain-rate, the applied amplitude and the frequency of the sinusoidally varying strain-rate. Finally, it is shown that the aforementioned phase-shift between the detailed simulations and the 3D FGM simulations disappears.

Published in Combustion and Flame 155 (2008), pp 133-144 [22]

4.1 Introduction

Generally, there are two main streams of research to treat chemical kinetics in current modeling efforts of complex combustion processes: chemical reduction techniques and laminar flamelet models. Reduction techniques [47,52,70] reduce the number of equations that have to be solved during combustion calculations, without losing too much accuracy. These techniques are based on the assumption that only a handful of slow processes dominates the behavior of the flame. The remaining processes are assumed to be much faster and are taken to be in steady state. These steady-state species, or linear

combinations of species, then define a low-dimensional manifold in state space and the slow processes follow a path inside this manifold.

A drawback of most reduction methods is that they are based on chemistry only and transport processes are not taken into account when constructing a manifold. While this may not be a problem in areas where the temperature is high and hence chemistry is dominant, this may lead to increasingly large errors in regions where the temperature is relatively low and transport becomes as relevant as chemistry [28].

Laminar flamelet models are based on the observation that in most applications combustion occurs in thin regions. This means that a three-dimensional flame can be considered as an ensemble of one-dimensional flame structures, called flamelets. Note that laminar flamelet models take transport processes into account and lead to more accurate results in colder regions of the flame [61]. The major drawback of most flamelet models is that it is not straightforward to extend the model to include more time-scales.

The classical non-premixed flamelet method [69, 71] is often used to simulate turbulent non-premixed flames and a so-called flamelet library is constructed that parameterizes the local composition manifold. For quasi-steady flames a 2D database is usually based on the mixture fraction Z and the scalar dissipation rate χ . This model has been very successful [40, 51, 60]. However, recent research has shown that it is not capable to model unsteady effects with high accuracy. For that reason, the Eulerian Particle Flamelet Model [4, 5, 38, 39] has been introduced and successfully applied for a variety of DI Diesel engine problems.

In recent years, the Combustion Technology Group at the Eindhoven University of Technology has been investigating ways to "bridge the gap" between reduction techniques and flamelet models. This has resulted in the Flamelet-Generated Manifolds (FGM) [61], which is similar to flame prolongation of ILDM (FPI) [32], and the Phase-Space Intrinsic Low-Dimensional Manifold (PS-ILDM) [10] methods. Both are a combination of methods used in manifold methods applied to flamelet models.

In this work a database method that has similarities to both chemical reduction methods as well as the flamelet approach is proposed. The basic idea is that steady and unsteady diffusion flamelets are used to generate a 2D and a 3D database, respectively. This aspect is the same as in the classical flamelet approach. The implementation however, has more in common with reduction techniques. Besides the mixture fraction Z , the database is further parameterized by (linear combinations of) species mass fractions, like in the ILDM method [52]. This results in the following general parametrization: $c = (c_1, c_2, \dots, c_N)$, with $c_1 = Z$ and where N is the number of controlling variables, and thus the dimension of the manifold.

Recently a number of new ideas has been explored to capture unsteady effects in other ways, i.e., by introducing additional parameters that describe the time evolution in the flamelet composition [73, 74, 76]. For example, Tap et al. [88], introduced an integral progress variable that monitors the temporal evolution during ignition of non-premixed flames under engine-like conditions. More recently, a similar procedure was proposed by Lehtiniemi et al. [49], while Piffaretti et al. [72], introduced a flame age parameter and

posed a transport equation for the flame age to model ignition and slow processes like NO_x formation in flames.

Apart from these difficulties related to the ignition and very slow processes, it is also not clear how well the current steady flamelet method is able to capture the unsteady flame response to fast fluctuations related to the turbulence in the flame. In turbulent jet diffusion flames, flamelet-like structures are expected to encounter varying strain-rates as they travel away from the nozzle. By simulating flamelets subjected to an unsteady fluctuating strain-rate we believe that an important aspect of turbulent (non-premixed) flames can be represented, i.e., the unsteady flow-field behavior. Fast fluctuations of the flow-field result in an almost instantaneous variation of the local stretch rate, while the chemistry takes some time to adjust to the new flow-field situation. This was also studied by other authors, both numerically [2, 21, 29, 41, 57] as well as experimentally [24, 43]. Mauß et al. [57], found that flamelets respond to changes of the scalar dissipation rate much more slowly than previously assumed. Barlow and Chen [2] concluded that turbulent methane jet flames cannot be properly represented by a laminar flamelet library constructed from *steady* laminar flamelets. Extensive studies on the dependence between the flame response and the frequency [21, 29] revealed that for low frequency oscillations, the flame response can be considered quasi-steady, which was also reported by [2]. For higher frequencies, a phase-lag occurs between the sinusoidally oscillating flow-field and important flame characteristics like temperature, heat release rate and species mass fractions. This was also shown experimentally in [43] by Kistler et al. When even higher frequencies are imposed, the flame becomes insensitive to the oscillating flow-field and all properties merge asymptotically towards mean values [29, 41]. This latter was also shown experimentally by Donbar et al. [24]. They showed that the strain-field oscillates at frequencies as high as 5 to 10 kHz and that the flame does not respond anymore at these high frequencies.

In this paper the response of non-premixed flames to unsteady flow-field oscillations, characterized by a sinusoidally oscillating strain-rate, is studied. The main question that will be answered is if this unsteady phenomenon can be captured in a low-dimensional Flamelet-Generated Manifold and whether application of the 2D and 3D manifolds yield satisfactory results. In section 4.2, the flame geometry and the governing equations are presented. A 2D FGM, based on steady flamelet simulations, is shown in section 4.3 and the application of this 2D FGM in a one-dimensional non-premixed flame simulation is discussed in section 4.3.1. Following that, in section 4.4 unsteady flamelet simulations using detailed chemical kinetics, representing oscillating flow-fields are performed. Subsequently, in section 4.4.1 it is investigated whether or not the unsteady flamelet trajectories form a 3D manifold and in section 4.4.2 the one-dimensional, unsteady, non-premixed flames are simulated again, but now the 3D FGM is applied. Finally some conclusions are drawn in section 4.5.

4.2 Governing equations

Using a two-dimensional planar counterflow geometry, laminar non-premixed flames are simulated with CHEM1D [14]. Detailed chemistry is modeled using the GRI 3.0 reaction

mechanism [84]. All flame quantities are a function of x_1 and t only and two-dimensional flow-field effects are represented by the local stretch rate K_M , which was proposed by De Goey and Ten Thije Boonkkamp [33]. The boundaries are defined at $x_1 = -L$ and $x_1 = L$ and at $x_1 = 0$ a stagnation plane exists. Two types of simulations are performed; a series of steady flames with different constant strain-rates and a series of unsteady flames with a time-dependent sinusoidally varying strain-rate. Conservation equations of mass, enthalpy and species mass for the 1D flames are given by:

$$\frac{\partial \rho}{\partial t} + \frac{\partial \rho u_1}{\partial x_1} = -\rho K_M, \quad (4.1)$$

$$\frac{\partial \rho h}{\partial t} + \frac{\partial \rho u_1 h}{\partial x_1} - \frac{\partial}{\partial x_1} \left(\frac{\lambda}{c_p} \frac{\partial h}{\partial x_1} \right) = -\rho K_M h, \quad (4.2)$$

$$\frac{\partial \rho Y_n}{\partial t} + \frac{\partial \rho u_1 Y_n}{\partial x_1} - \frac{\partial}{\partial x_1} \left(\frac{\lambda}{c_p} \frac{\partial Y_n}{\partial x_1} \right) = \dot{\omega}_n - \rho K_M Y_n, \quad (4.3)$$

where ρ is the density, u_1 the velocity in x_1 -direction, h the specific enthalpy, Y_n the mass fraction of species n , λ the local thermal conductivity of the mixture, c_p the local constant pressure heat capacity of the mixture and $\dot{\omega}_n$ the chemical source-term of the n^{th} species. In order to compare with the classical $Z\chi$ diffusion flamelet method [69], where mostly $Le_n = 1$ is used, the Lewis numbers used here are also equal to unity. As a consequence, preferential diffusion effects are absent. The x_2 -component of the velocity is taken into account by introducing the local stretch rate K_M , which is governed by [87]:

$$\rho \frac{\partial K_M}{\partial t} + \rho u_1 \frac{\partial K_M}{\partial x_1} - \frac{\partial}{\partial x_1} \left(\mu \frac{\partial K_M}{\partial x_1} \right) = P(t) - \rho K_M^2, \quad (4.4)$$

where μ is the dynamic viscosity, P is the tangential pressure gradient, and is given by: cf. [15]:

$$P(t) = \rho_{\text{ox}} \left(\frac{\partial a(t)}{\partial t} + a(t)^2 \right), \quad (4.5)$$

with a the applied strain-rate (at $x_1 = L$), which can be a function of time t . If the oxidizer and fuel streams originate far away from the flame, then the flow-field can be assumed to behave as a potential flow, with a prescribed velocity gradient a :

$$\frac{\partial u_1}{\partial x_1} = -a \quad \text{and} \quad K_M = \frac{\partial u_2}{\partial x_2} = a. \quad (4.6)$$

The fuel (at $x_1 = -L$) and oxidizer (at $x_1 = L$) composition are chosen to be the same as in the Sandia Flames [3]. The fuel and oxidizer compositions, which are in mole fractions, are listed in table 4.1.

Table 4.1: The fuel and oxidizer compositions are chosen to be the same as in the Sandia Flames [3]. The applied boundary conditions are listed in mole-fractions.

	Fuel	Oxidizer
X_{CH_4}	0.2500	–
X_{O_2}	0.1575	0.2100
X_{N_2}	0.5925	0.7900

4.3 Steady flamelet simulations

A series of steady flames, with different, but constant strain-rates a is simulated. The strain-rate was varied from 0.1 s^{-1} , i.e., close to chemical equilibrium, to 1265 s^{-1} , which is near the extinction limit for these flames.

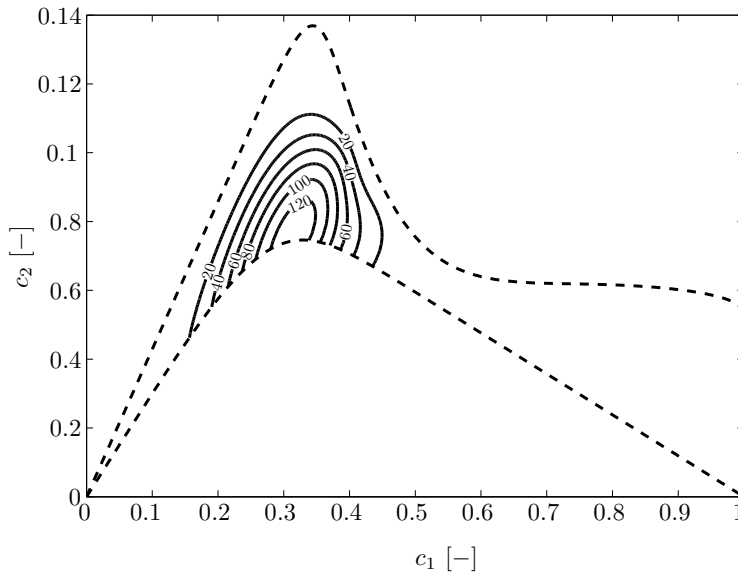


Figure 4.1: Contour-plot of the chemical source-term $\dot{\omega}_{c_2}$ [$\text{kg m}^{-3} \text{ s}$] as a function of the mixture fraction $c_1 = Z$ and the second controlling variable $c_2 = Y_{\text{CO}_2}$. The dashed lines represent boundaries dictated by the flamelets with $a = 0.1 \text{ s}^{-1}$ (top dashed line), which is near chemical equilibrium, and $a = 1265 \text{ s}^{-1}$ (bottom dashed line), which is near the extinction limit.

This set of steady flame compositions spans a two-dimensional manifold in composition space. An example of such a 2D FGM can be seen in figure 4.1, where a contour-plot of the chemical source-term $\dot{\omega}_{c_2}$ is shown as a function of both the mixture fraction $c_1 = Z$, i.e., the first controlling variable, and the second controlling variable c_2 . For the second controlling variable the mass-fraction of CO_2 was chosen, since it is monotonously increasing in the area of interest, i.e., around $a = 500 \text{ s}^{-1}$. The dashed lines represent flamelets with $a = 0.1 \text{ s}^{-1}$ (top dashed line) and $a = 1265 \text{ s}^{-1}$ (bottom dashed line). Note that because there is already oxygen present in the fuel stream, a premixed flame

structure exists near the boundary $Z = 1$, but only for very low strain-rates. Furthermore, the 2D FGM consists of 33 different flamelets.

4.3.1 Application of a 2D manifold

Flames with temporal strain variations are simulated using a reduced set of equations. Two different parameterizations are used and compared, i.e., the (Z, χ) parametrization and the (c_1, c_2) parametrization, with $c_1 = Z$ and $c_2 = Y_{\text{CO}_2}$. Note that the manifold used in both methods is the same, and that only the parametrization and the implementation is different. The first will be referred to as the $Z\chi$ – method. The scalar dissipation rate χ is defined as follows:

$$\chi = 2D (\nabla Z \cdot \nabla Z). \quad (4.7)$$

During run-time, a conservation equation for Z is solved and χ is determined by using the following analytical expression [71]:

$$\chi(Z) = \frac{a}{\pi} \exp \left(-2 \left[\text{erfc}^{-1}(2Z) \right]^2 \right), \quad (4.8)$$

where $\text{erfc}^{-1}(x)$ is the inverse of the complementary error function. Generally the database is then parameterized with Z and χ_{st} . During the simulation, the local values of the mixture fraction Z_{loc} and the scalar dissipation rate χ^{loc} are used to compute the stoichiometric value of the scalar dissipation rate χ_{st} by using the following expression:

$$\chi_{\text{st}} = \chi^{\text{loc}} \left(\frac{\chi(Z_{\text{st}})}{\chi(Z_{\text{loc}})} \right), \quad (4.9)$$

where $\chi(Z_{\text{st}})$ and $\chi(Z_{\text{loc}})$ are computed with (4.8) for Z_{st} and Z_{loc} , respectively.

In the second method, referred to as the Zc_2 – method, local values for Z and c_2 are used to retrieve data from the database. In contrast to the $Z\chi$ – method, now for the second controlling variable c_2 a transport equation is solved.

4.4 Unsteady flamelet simulations

To study whether unsteady flow-field effects can be captured in a low-dimensional FGM, flamelets subjected to sinusoidally varying strain-rates are simulated and analyzed, using the detailed GRI 3.0 reaction mechanism.

A series of flames with the same boundary conditions as for the steady case, but now with a sinusoidally varying strain-rate is simulated. The strain-rate in this case is given by:

$$a(t) = \bar{a} + \Delta a \cdot \cos(\omega t), \quad (4.10)$$

where Δa is the amplitude, \bar{a} the mean value of the strain-rate and $\omega = 2\pi f$, with f the frequency. The strain-rate a is varied at the boundaries, and although the flame is situated

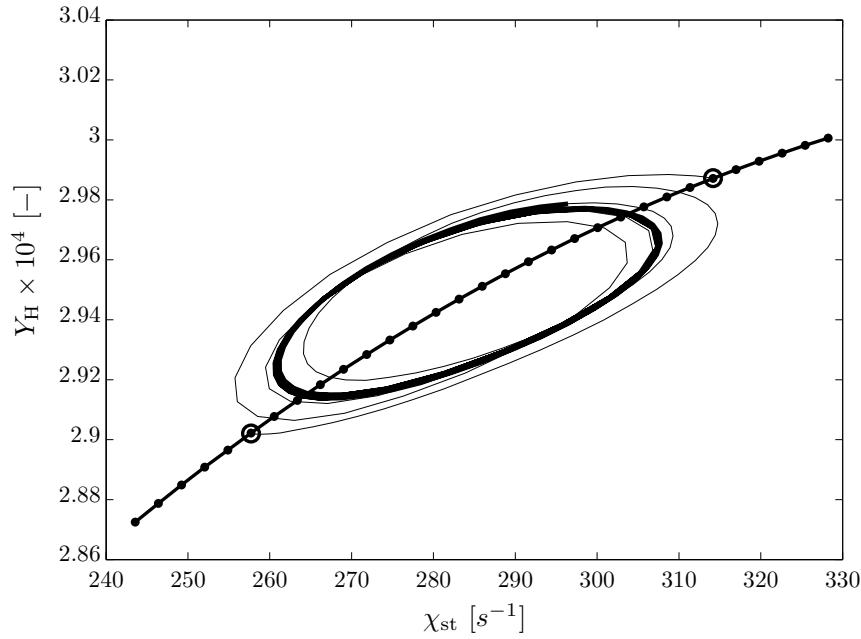
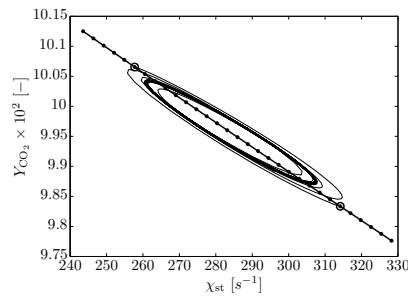
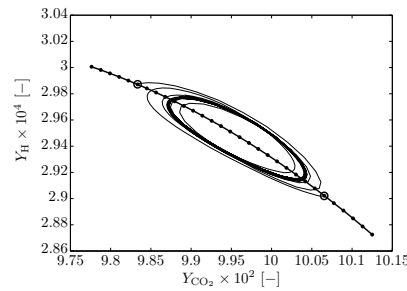
(a) Y_H as a function of χ_{st} (b) Y_{CO_2} as a function of χ_{st} (c) Y_H as a function of Y_{CO_2}

Figure 4.2: Typical example of unsteady trajectories in composition space, with $c_1 = Z_{st}$. The strain-rate parameters are $\Delta a = 50 \text{ s}^{-1}$, $\bar{a} = 500 \text{ s}^{-1}$ and $f = 1000 \text{ Hz}$. The solid line with the dots represents the steady flamelets simulations. The solid lines correspond to two unsteady flamelet simulations, where only the initial values of the strain-rate (indicated by the circles) differ. After initialization (thin solid line), the unsteady trajectories move along a so-called "limit cycle" (thick solid line).

at a certain distance from the boundaries, it will immediately feel the stretch effects K_M , because of the low-Mach number formulation, cf. equations (4.4) and (4.5).

Like in the constant strain-rate case, the mean strain-rate \bar{a} was varied from equilibrium to extinction. The amplitude Δa varies from 10 s^{-1} up to 300 s^{-1} , and the frequency ranges from 50 Hz to very high frequencies of up to 10^5 Hz . It was observed that for very high frequencies, the amplitude ratio between the flow-field oscillations and the response of the flame variables to the applied strain-rate decreases, which was also reported in [21].

A typical result of trajectories in composition space can be seen in figure 4.2, where a cut is made at $c_1 = Z_{st}$ with $\Delta a = 50 \text{ s}^{-1}$, $\bar{a} = 500 \text{ s}^{-1}$ and $f = 1000 \text{ Hz}$. Shown are three

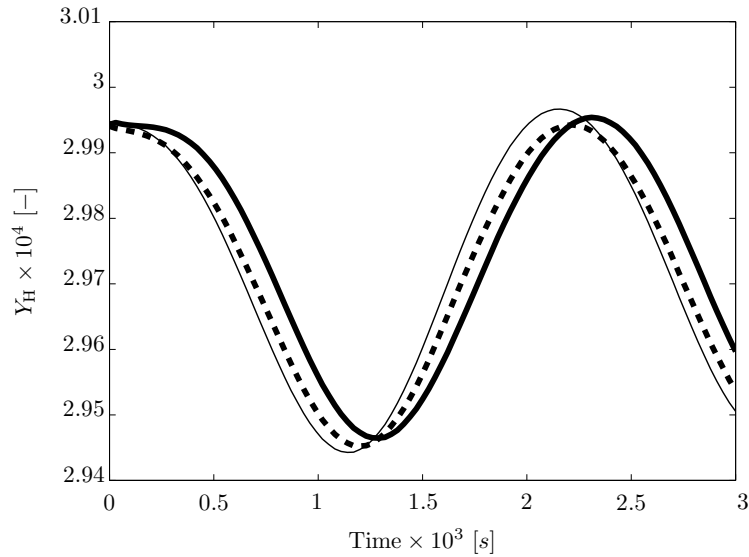


Figure 4.3: Mass-fraction of atomic hydrogen H as a function of time for $Z = Z_{st} = 0.3528$. The mean strain-rate is $\bar{a} = 500 \text{ s}^{-1}$, the amplitude is $\Delta a = 25 \text{ s}^{-1}$ and the frequency is $f = 500 \text{ Hz}$. Shown here are a detailed simulation (thick solid), the $Z\chi$ – method (thin solid) and the Zc_2 – method (dashed line).

different representations of the same simulations, i.e., Y_H as a function of χ_{st} (a), Y_{CO_2} as a function of χ_{st} (b) and Y_H as a function of Y_{CO_2} (c). The solid line with the dots represents the steady flamelets simulations, which span a 2D 'steady' manifold, while the grey solid lines correspond to two unsteady flamelet simulations, where only the initial values of the strain-rate (indicated by the circles) differ. It is apparent that after initialization (thin solid line), the unsteady trajectories move along a so-called "limit cycle" (thick solid line). Note that the initial composition (circles) are not a part of the unsteady "limit cycle". Furthermore, it can be concluded that although the initial values of the strain-rate are different, i.e., $a_{0,1} = 450$ and $a_{0,2} = 550$, both unsteady trajectories end up on the same "limit cycle".

For $\bar{a} = 500 \text{ s}^{-1}$, $\Delta a = 50 \text{ s}^{-1}$ and $f = 500 \text{ Hz}$, the results are compared with the detailed chemistry computations in figure 4.3. The thick solid line represents the detailed simulation, the thin solid line is the $Z\chi$ – method and the dashed line is the Zc_2 – method. As can be seen, the mass-fraction of H of the detailed simulation is predicted within reasonable accuracy by both the $Z\chi$ – method and the Zc_2 – method. Both the $Z\chi$ – method and the Zc_2 – method simulations however, show a slight phase-lag compared to the detailed simulation. The apparent non-sinusoidal behavior of the detailed chemistry simulation is due to initialization, as shown in figure 4.2.

4.4.1 Manifold dimensional analysis

In order to investigate the dimension of the higher-dimensional manifold spanned by all the unsteady flame trajectories and to study whether the 2D steady manifold is

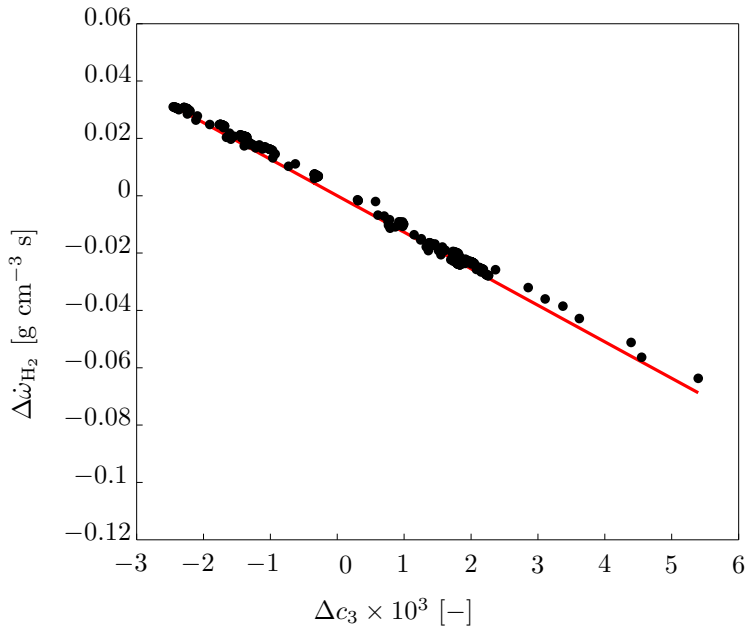


Figure 4.4: Chemical source-term of H_2 as a function of c_3 for $Z = Z_{st} = 0.3528$ and $c_2 = 0.1085$. The mean strain-rate is $\bar{a} = 175 \text{ s}^{-1}$ and the amplitude was varied between $\Delta a = 25 \text{ s}^{-1}$ and $\Delta a = 55 \text{ s}^{-1}$. Various frequencies were studied, ranging from 10^2 Hz to 10^5 Hz .

embedded in this manifold, the oscillating flamelet simulations are studied. A typical result was already shown in figure 4.2, where the trajectory of the flamelets subjected to a sinusoidally strain-rate clearly resembles a so-called Lissajous curve. This indicates that there is a phase-shift between Y_{CO_2} and Y_H (figure 4.2(c)). As mentioned, this was also reported by Darabiha [21], Egolfopoulos and Campbell [29] and Kistler et al. [43]. Consequently if $c_1 = Z$ and $c_2 = Y_{CO_2}$ are used to parameterize the 2D manifold, Y_H automatically will have the same phase as Y_{CO_2} . It is investigated whether this problem can be avoided by using an additional controlling variable, c_3 . A large number of oscillating flames with varying \bar{a} , Δa and f is used to generate a manifold. To determine whether the dimension of the generated manifold is 3, intersections of the trajectories for constant values of c_1 and c_2 are constructed and a scatter plot as a function of c_3 is obtained. This method was also applied by van Oijen et al. [62] to determine the dimension of the low-dimensional manifold present in a premixed turbulent flame. If the scatter is concentrated around a one-dimensional curve at constant c_1 and c_2 , the local dimensionality of the unsteady manifold is 3 and the flame characteristics can be stored and parameterized as functions of only three parameters, c_1 , c_2 and c_3 . If however, the scatter is not concentrated around a one-dimensional curve, the local dimension of the unsteady manifold is higher than 3 and more controlling variables may be needed. It should be noted that although methods like ILDM and CSP are excellent ways to determine the chemical time-scales of a system, both methods would not provide the dimensionality of the Flamelet-Generated Manifold. This is due to the fact that both ILDM and CSP only take chemistry into account, while the FGM method also includes transport time-scales.

For a mean strain-rate of $\bar{a} = 175 \text{ s}^{-1}$, a cross-section of $\Delta\dot{w}_{H_2}$, which is defined as

$(\dot{\omega}_{\text{H}_2} - \dot{\omega}_{\text{H}_2}^{2\text{D}})$, is shown in figure 4.4 as a function of Δc_3 , with $c_1 = Z = Z_{\text{st}}$ and $c_2 = Y_{\text{CO}_2} = 0.1085$, where $\Delta c_3 = (c_3 - c_3^{2\text{D}})$. This means that the steady manifold composition corresponding to $\bar{a} = 175 \text{ s}^{-1}$ is the point $(0, 0)$ and the values along the x_2 -axis represent the relative difference between $\dot{\omega}_{\text{H}_2}$ and $\dot{\omega}_{\text{H}_2}^{2\text{D}}$. The amplitude was varied between $\Delta a = 25 \text{ s}^{-1}$ and $\Delta a = 55 \text{ s}^{-1}$ and also various frequencies were studied, ranging from 10^2 Hz to 10^5 Hz . The dots represent all the encountered compositions during the unsteady flame simulations for which $c_1 = Z_{\text{st}}$ and $c_2 = 0.1085$. The solid line is a 1st order polynomial fit and as can be seen, it includes the point $(0, 0)$ indicating that the 2D manifold is embedded in the 3D manifold. So locally, the steady 2D manifold can be expanded (linearly in this case), by adding the unsteady effects, which results in a 3D manifold. This 3D manifold can be parameterized with c_1 , c_2 and c_3 . As mentioned, the 3D manifold was generated by performing a lot of different detailed simulations, where the strain-rate parameters, i.e., the initial strain-rate, the applied amplitude and the frequency, were varied, while the mean strain-rate was chosen constant. Hence, many different combinations of the strain-rate parameters are included in the 3D manifold. This can also be seen in figure 4.4, which shows that even when the initial strain-rate a_0 , the amplitude Δa and the frequency f are different for each simulation, the species source-terms $\dot{\omega}_i$ are still uniquely parameterized by c_1 , c_2 and c_3 . This means that a very broad range of the strain-rate parameters can be accurately predicted using this 3D FGM. Furthermore, it was also observed that once on the manifold, unsteady phenomena move along the manifold independent of time or initial conditions.

The source-term of H_2 is merely shown here to illustrate that even for very high frequencies, i.e., up to 10^5 Hz , large amplitudes and different initial strain-rates, the 2D FGM can be extended to a 3D FGM using polynomials. A more important quantity is the source-term of the second additional controlling variable, $\dot{\omega}_{c_3}$. In figures 4.5(a)-4.5(c), $\Delta \dot{\omega}_{c_3}$ is shown as a function of Δc_3 for a mean strain-rate of $\bar{a} = 500 \text{ s}^{-1}$. The amplitude was varied from $\Delta a = 10 \text{ s}^{-1}$ up to $\Delta a = 300 \text{ s}^{-1}$ and the frequency between 500 Hz and 10^5 Hz . Three cross-sections of the mixture fraction are shown, i.e., $c_1 = Z_{\text{st}}$ (figure 4.5(a)), $c_1 = 0.5Z_{\text{st}}$ (figure 4.5(b)) and $c_1 = 2Z_{\text{st}}$ (figure 4.5(c)). The dots represent the flamelets subject to the unsteady strain-rates. The 1st order polynomial fit is given by the solid lines, whereas in figure 4.5(c) the dashed line indicates a second order fit. Although it can be seen that the linearization is the most accurate around $c_1 = Z_{\text{st}}$, where chemistry is dominant, at $c_1 = 0.5Z_{\text{st}}$ the linearization is still quite reasonable. The accuracy can be improved by using a 2nd order fit (dashed line in figure 4.5(c)). Storage and retrieval will only be marginally more expensive. In this study however, only linear fits are used.

Figure 4.6 shows a typical example of a species whose chemical time-scales are of the same order, or even slower, than the flow-field time-scales, i.e., NO . It is immediately clear that the unsteady flamelet simulations performed here do not form a 3D FGM for such species.

It can be concluded that flamelets subjected to oscillating strain-rates, where the mean value of the strain-rate \bar{a} , the amplitude Δa and the frequency f were varied, form a 3D FGM for the majority of the species.

4.4.2 Application of a 3D manifold

In order to investigate the accuracy during unsteady simulations using the 3D FGM a transport equation for the additional controlling variable c_3 is solved. During an

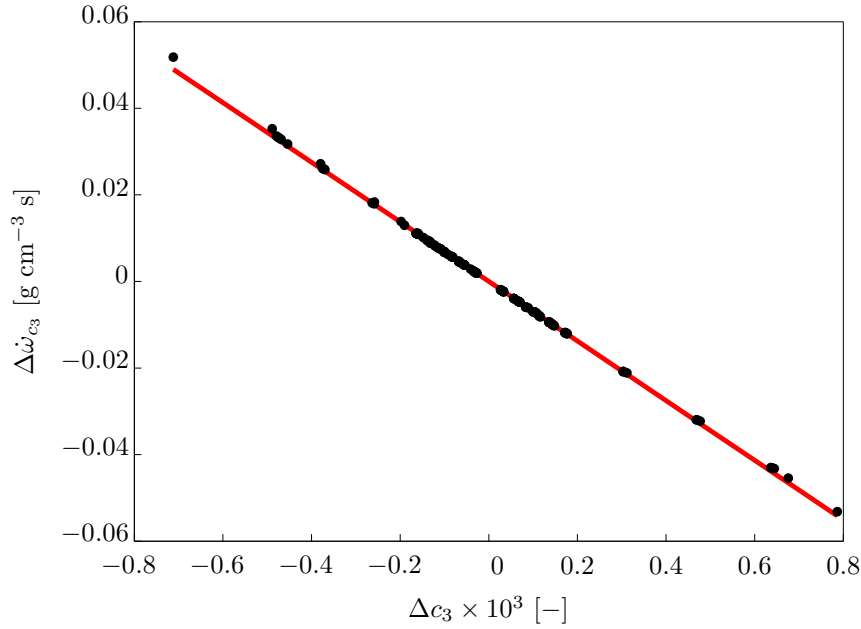
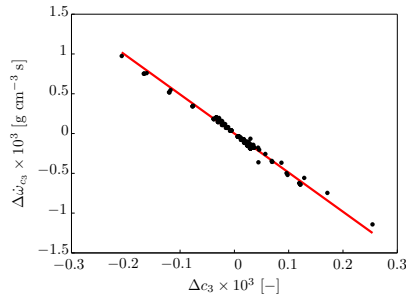
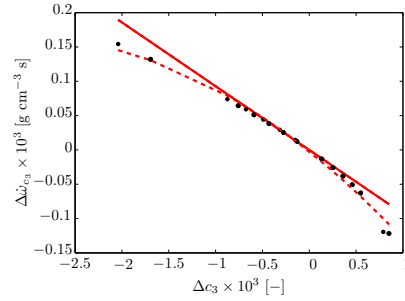
(a) $Z = Z_{st} = 0.3528$ and $c_2 = 0.0995$ (b) $Z = 0.5Z_{st}$ and $c_2 = 0.0653$ (c) $Z = 2Z_{st}$ and $c_2 = 0.0481$

Figure 4.5: Chemical source-term of c_3 as a function of Δc_3 for various values of c_1 and c_2 : (a) $Z = Z_{st} = 0.3528$, $c_2 = 0.0995$, (b) $Z = 0.5Z_{st} = 0.1764$, $c_2 = 0.0653$ and (c) $Z = 2Z_{st} = 0.7056$, $c_2 = 0.0481$. The mean strain-rate is $\bar{a} = 500 \text{ s}^{-1}$ and the amplitude was varied between $\Delta a = 10 \text{ s}^{-1}$ and $\Delta a = 300 \text{ s}^{-1}$. The frequency was varied between $f = 500 \text{ Hz}$ and $f = 10^5 \text{ Hz}$. The black dots represent the flamelets subjected to the sinusoidally varying strain-rate. The solid lines are a 1st order polynomial fit and the dashed line in Fig. 4.5(c) is a 2nd order fit.

unsteady simulation, the local values for c_1 , c_2 and c_3 are used to look-up the chemical source-term of c_3 for instance, in the following way:

$$\Delta \dot{w}_{c_3}(c_1, c_2, c_3) \approx \alpha(c_1, c_2) \cdot \Delta c_3(\mathbf{x}, t), \quad (4.11)$$

where the polynomial coefficient $\alpha(c_1, c_2)$ is computed in a preprocessing step by fitting a polynomial, a linear polynomial in this case, through the data points generated with the unsteady simulations (figures 4.4 and 4.5(a)). The data-points in this case are all flame compositions found during the unsteady flamelet simulations. By determining the local polynomial coefficient $\alpha(c_1, c_2)$ of the 1st order fit, a 3D manifold, including unsteady

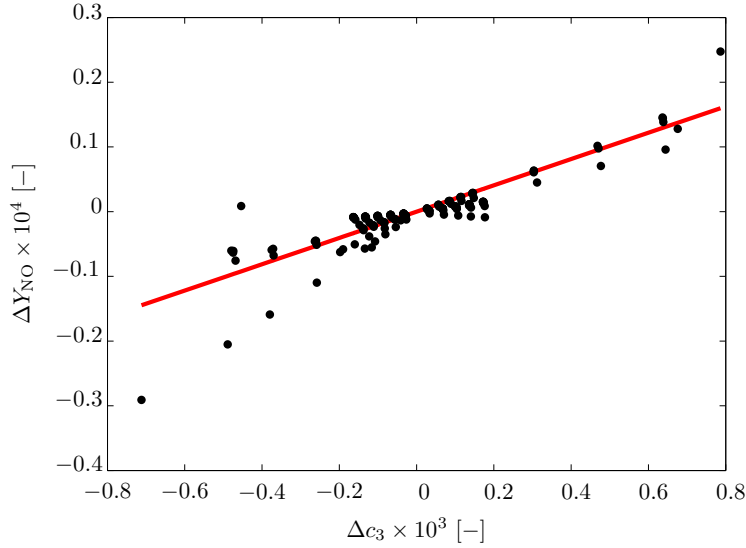


Figure 4.6: Mass-fraction of NO as a function of Δc_3 for constant values of c_1 and c_2 : $c_1 = Z_{st} = 0.3528$ and $c_2 = 0.0995$. The mean strain-rate is $\bar{a} = 500 \text{ s}^{-1}$ and the amplitude was varied between $\Delta a = 10 \text{ s}^{-1}$ and $\Delta a = 300 \text{ s}^{-1}$. The frequency was varied between $f = 500 \text{ Hz}$ and $f = 10^5 \text{ Hz}$. The black dots represent the flamelets subjected to the sinusoidally varying strain-rate. The solid line is a 2nd order polynomial fit.

effects can be constructed around the 2D manifold. This is done at constant values of c_1 and c_2 . This 3D linear extension results in moderate extra storage costs, typically the database will become twice as large. Instead of a linear polynomial, higher order polynomial fits can also be employed, which will result in additional storage costs. Here the linear fit was chosen, because the additional accuracy was negligible. Furthermore, the amplitude Δa , the mean strain-rate \bar{a} and the frequency f can be varied to capture the complete range of strain-rates, from equilibrium to extinction.

Concerning the third controlling variable, two important quality criteria have to be taken into account. These two criteria are:

1. Within the 3D manifold, the 2D manifold should be attracting.
2. The manifold should be well-conditioned.

The first criterion implies that when $\Delta c_3 = c_3 - c_3^{2D}$ is positive then $\Delta \dot{w}_{c_3} = \dot{w}_{c_3} - \dot{w}_{c_3}^{2D}$ should be negative during application of the 3D manifold. This means that:

$$J = \frac{\partial \Delta \dot{w}_{c_3}}{\partial \Delta c_3} < 0. \quad (4.12)$$

Regarding the second criterion, the condition number can be defined as follows:

$$C = \left\| \frac{x f'(x)}{f(x)} \right\| = \left\| \frac{\Delta c_3}{\Delta \dot{w}_{c_3}} \right\| \|J\|. \quad (4.13)$$

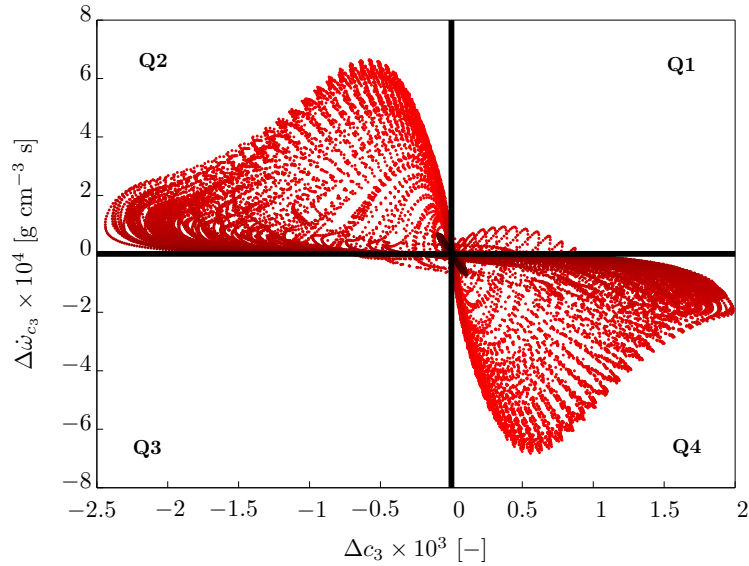


Figure 4.7: The chemical source-term of c_3 as a function of the mass fraction c_3 for all values of Z and c_2 , both with respect to the 2D FGM.

When the condition number is low, the problem is well-conditioned and in this case this means that absolute value of J should be smaller than some critical value J_{crit} :

$$\|J\| < J_{\text{crit}}. \quad (4.14)$$

Applying these criteria, the third controlling variable is defined as $c_3 = 4Y_{\text{O}_2} - 6Y_{\text{OH}} - 2Y_{\text{H}_2} - 2Y_{\text{CO}}$. It should be noted that c_3 has been tuned such that it obeys the two criteria. Furthermore, the procedure outlined here is not an automated procedure, which means that there may well be other (equally) successful choices. For a mean strain-rate of $\bar{a} = 500 \text{ s}^{-1}$, an amplitude of $\Delta a = 500 \text{ s}^{-1}$ and a frequency of $f = 500 \text{ Hz}$, figure 4.7 shows the chemical source-term $\Delta\dot{\omega}_{c_3}$ as a function of Δc_3 , both with respect to the 2D FGM. The lighter dots denote those values where the mixture fraction is equal to the stoichiometric value and darker dots indicate those values where the mixture fraction is either zero or one. As can be seen, $J < 0$ for the majority of the data-points. Several other choices for the third controlling variable, like $c_3 = Y_{\text{OH}}$, have also been applied but these did not result in a stable numerical procedure, since these choices did not obey the aforementioned two criteria.

A good indicator for stability of the method is N_G/N_T , where N_G is the total number of data-points in either the second or fourth quadrant and N_T is the total number of data-points. The quadrants are numbered from 1 to 4 beginning in the top-right corner of figure 4.7 and counting counter-clockwise. Ideally, all the data-points will be located in the second and fourth quadrants, i.e., $N_G/N_T = 1$. In the current case, with $c_3 = 4Y_{\text{O}_2} - 6Y_{\text{OH}} - 2Y_{\text{H}_2} - 2Y_{\text{CO}}$, N_G/N_T was equal to 0.92. Although some data-points are located in the "unstable" quadrants **Q1** and **Q3**, this does not necessarily lead to divergence, due to the rather compactness of these data-points compared to those located in quadrants **Q2** and **Q4**. This means that when during a 3D FGM application the composition is located in, for instance, the first quadrant, the chemical source-term

$\Delta\dot{\omega}_3$ is positive, which leads to an increase of c_3 itself. As a result, the solution is then forced to the fourth quadrant, which is again stable. Therefore, even though some data-points can be considered unstable, application of this 3D manifold will always result in a stable numerical procedure.

4.4.3 Results and discussion

As a test case, an unsteady flamelet simulation, using the 3D FGM, was performed. Furthermore, other values for the strain-rate parameters than those used when constructing the 3D manifold were chosen. For $\bar{a} = 500 \text{ s}^{-1}$, $\Delta a = 25 \text{ s}^{-1}$ and $f = 500 \text{ Hz}$ a cross-section at $c_1 = Z_{\text{st}}$ of the results of the application of the 3D manifold are compared with a detailed and 2D manifold simulations in figure 4.8. The solid line represents the detailed simulation, the dashed lines represent the simulations with the 2D manifold, i.e., the Z_{c_2} – method and the circles represent the 3D manifold. As can be seen, the 3D manifold simulation is in very good agreement with the detailed simulation. Also, the phase-shift has disappeared, as can be clearly seen in figure 4.8. Furthermore, in figure 4.8(b), c_3 can be seen as a function of c_2 . It is evident that both the trajectories of the detailed and the 3D manifold simulations resemble a Lissajous curve, indicating that there is a phase-shift between c_2 and c_3 in both those simulations. For Y_{H} , the phase-shift between the detailed and the 2D manifold simulations is even more prominent, while between the detailed and the 3D manifold simulations this phase-shift is almost gone.

When the 3D manifold presented here, is coupled to a turbulence model, a potential problem arises. Due to the fact that the controlling variables c_1 , c_2 and c_3 are not statistically independent of each other, the common assumption [71] that:

$$P(c_2, c_3) = P(c_2)P(c_3), \quad (4.15)$$

is not justified. A possible solution could be to introduce Δc_3 , as follows:

$$\Delta c_3 = c_3 - c_3^{2\text{D}}, \quad (4.16)$$

where $c_3^{2\text{D}}$ is the 2D FGM value. Henceforth, it can be assumed that c_2 and c_3 are statistically independent.

4.5 Conclusions

The primary goal was to investigate whether unsteady phenomena can be captured and parameterized using a flamelet database. It can be concluded that when using the FGM method, unsteady flow-field effects can indeed be included in the manifold, resulting in a 3D FGM that can be parameterized by c_1 , c_2 and c_3 .

Moreover, it is shown that the compositions found in steady laminar diffusion flames span a two-dimensional attracting manifold in composition space. Using this 2D FGM, flamelets subjected to an oscillating strain-rate were simulated with both the classical Z_{χ} – method as well as the Z_{c_2} – method method. As a direct result of using only two

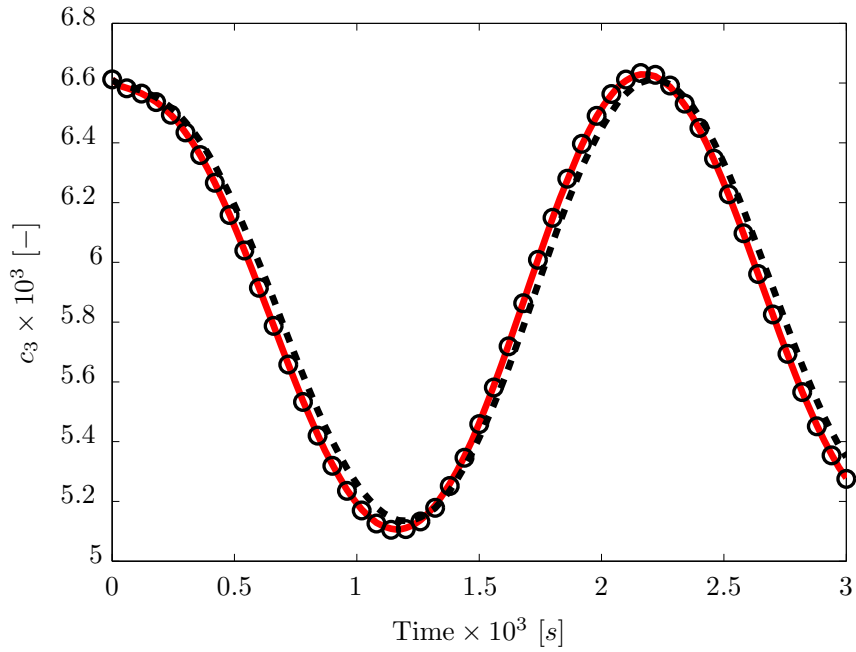
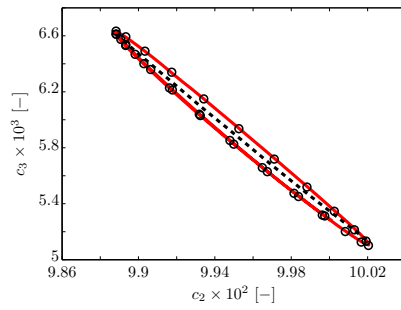
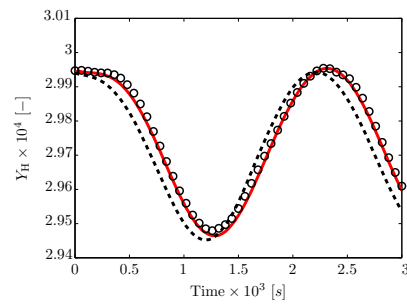
(a) c_3 as a function of time(b) c_3 as a function of c_2 (c) Y_H as a function of time

Figure 4.8: Comparison between the 2D manifold simulation (dashed line), the 3D manifold simulation (circles) and the detailed simulation (solid line), with $\bar{a} = 500 \text{ s}^{-1}$, $\Delta a = 25 \text{ s}^{-1}$ and $f = 500 \text{ Hz}$.

parameters, i.e., Z and χ or $c_1 = Z$ and $c_2 = Y_{\text{CO}_2}$, a phase-shift occurs between the detailed simulation and the $Z\chi$ – method and Zc_2 – method simulations.

In order to avoid the phase-shift, a 3D FGM is constructed and analyzed, using flamelets subjected to a (temporally) sinusoidally varying strain-rate. The trajectories of the unsteady laminar diffusion flames are situated close to the 2D manifold. It was shown that for the relevant manifold variables, i.e., the chemical source-terms of c_2 and c_3 , as well as the temperature, density and the specific heat, it was possible to linearly extend the 2D FGM to a 3D FGM, using polynomials. This provides an elegant method of generating a 3D FGM, which is able to reproduce unsteady effects.

The main conclusion that can be drawn is that a 2D FGM, based on steady flamelets, does not reproduce unsteady phenomena sufficiently. However, the unsteady flamelet simulations with sinusoidally varying strain-rates, can be used to generate a 3D FGM. Generating such a 3D FGM is relatively easy, because only very few simulations have to be performed, due to the found linear behavior (in this case) of the manifold to the amplitude, frequency or the mean value of the strain-rate. Please note that this linear behavior is not generally true and higher order polynomials may be needed.

It should be noted that in the presented research all Lewis numbers are equal to 1 as is the case for the classical diffusion flamelet approach and most flamelet applications in turbulent flame simulations. In the future, the impact of the transport model on the observations found here should be further studied. Furthermore, the possibility of incorporating other unsteady effects in the FGM should also be investigated.

CHAPTER FIVE

Incorporating extinction and re-ignition in Flamelet-Generated Manifolds

To study whether the effect of local flow fluctuations can be captured by the FGM approach, especially near the extinction limit, both steady and unsteady non-premixed flamelet simulations with a detailed chemistry model are studied. Two different Flamelet-Generated Manifolds are constructed in the vicinity and beyond the steady extinction limit. The first manifold is a 2D FGM that is primarily based on steady flamelet simulations, which means it is bounded by the steady extinction limit. Therefore an unsteady extinguishing flamelet simulation is used as a natural continuation of the 2D FGM. The second manifold is derived from a whole series of unsteady flamelets that are subjected to sinusoidally varying strain-rates. It is shown that these unsteady flamelet simulations form a 3D manifold in composition space, which is parameterized with c_1 , c_2 and c_3 . Furthermore, this 3D FGM accurately predicts a broad range of the strain-rate parameters.

Both manifolds are applied to simulate flames that are subjected to sinusoidally varying strain-rate. The results are compared to an unsteady simulation with a detailed chemistry model. Both local observables as well as flame-surface area properties are represented well with both manifolds. However, for species that are related to the slowest time-scales (e.g., NO_x) it is shown that a 3D manifold may result in less accurate predictions, and more controlling variables may be needed. It is shown that generating a 4D manifold is relatively easy and that the application of such a 4D manifold may lead to a significant improvement in the predictions of species related to the slowest time-scales.

Published in Proceedings of the Combustion Institute 32 (2009), pp 1051-1058 [23]

5.1 Introduction

Generally, there are two main streams of research to treat chemical kinetics in the modeling of complex combustion processes: chemical reduction techniques [13, 47, 52, 70, 80, 83] and laminar flamelet models [69, 71], which both reduce the number of equations that have to be solved during combustion calculations, without losing too much accuracy. Combining methods used in manifold approaches and flamelet models, has led to the development of Flamelet Generated Manifolds (FGM) [61], which is similar to flame prolongation of ILDM (FPI) [32], and the Phase-Space Intrinsic Low-Dimensional Manifold (PS-ILDM) [10] methods.

In many combustion applications time-dependent phenomena play an important role due to the presence of turbulence, which causes unsteady flow-fields, local extinction and re-ignition. There are several ways to take these unsteady phenomena into account by introducing additional parameters that describe the time evolution in the flamelet composition [4, 38, 73, 74, 76]. For example, Tap et al. [88], introduced an integral progress variable that monitors the temporal evolution during ignition of non-premixed flames under engine-like conditions. More recently, a similar procedure was proposed by Lehtiniemi et al. [49], while Piffaretti et al. [72], introduced a flame age parameter and posed a transport equation for the flame age to model ignition and slow processes like NO_x formation in flames.

Apart from the difficulties related to these inherently time-dependent processes, it is not clear how well the current steady flamelet method is able to capture the unsteady flame response to fast fluctuations related to the turbulence in the flame. In turbulent jet diffusion flames, flamelet-like structures are expected to encounter varying strain-rates as they travel away from the nozzle. Fast fluctuations of the flow-field result in an almost instantaneous variation of the local stretch rate, while transport processes and chemistry take some time to adjust to the new flow-field situation. This was also studied by other authors, both numerically [2, 21, 29, 57] as well as experimentally [24, 43].

In this paper it will be studied to what extent unsteady flow-effects can be captured and reproduced with an FGM approach, with a focus on high mean strain-rates, i.e., around, and even shortly beyond, the extinction limit. At these high strain-rates extinction and re-ignition occur, and although actual extinction is not pursued, the simulated flames will go along the extinction pathway. First, in section 5.2, the flame geometry and the governing equations are presented. The generation of Flamelet-Generated Manifolds, based on steady and unsteady flamelet simulations, is shown in sections 5.3.1 and 5.3.2, respectively. Following that, in section 5.4 unsteady flamelet simulations subjected to a sinusoidally oscillating strain-rate that exceeds the steady extinction limit considerably, are studied. The detailed chemical kinetics results are compared to both a 2D FGM and a 3D FGM application. Additionally a brief analysis regarding species with slow time-scales is given in section 5.4.1. Finally some conclusions are drawn in section 5.5.

5.2 Governing equations

Using a two-dimensional planar counterflow geometry, laminar non-premixed flames are simulated with CHEM1D [14]. Detailed chemistry is modeled using the GRI 3.0 reaction

Table 5.1: The applied boundary conditions in mole-fractions.

	X_{CH_4}	X_{O_2}	X_{N_2}
Fuel at $x_1 = -L$	0.2500	0.1575	0.5925
Oxidizer at $x_1 = L$	–	0.2100	0.7900

mechanism [84]. All flame quantities are a function of x_1 and t only and two-dimensional flow-field effects are represented by the local stretch rate K_M [33]. Conservation equations of mass, enthalpy and species mass can be written as:

$$\frac{\partial \rho}{\partial t} + \frac{\partial \rho u_1}{\partial x_1} = -\rho K_M, \quad (5.1)$$

$$\frac{\partial \rho h}{\partial t} + \frac{\partial \rho u_1 h}{\partial x_1} - \frac{\partial}{\partial x_1} \left(\frac{\lambda}{c_p} \frac{\partial h}{\partial x_1} \right) = -\rho K_M h, \quad (5.2)$$

$$\frac{\partial \rho Y_n}{\partial t} + \frac{\partial \rho u_1 Y_n}{\partial x_1} - \frac{\partial}{\partial x_1} \left(\frac{\lambda}{c_p} \frac{\partial Y_n}{\partial x_1} \right) = \dot{\omega}_n - \rho K_M Y_n, \quad (5.3)$$

where ρ is the density, u_1 the velocity in x_1 -direction, h the specific enthalpy, Y_n the mass-fraction of species n , λ the local thermal conductivity of the mixture, c_p the local constant pressure heat capacity of the mixture and $\dot{\omega}_n$ the chemical source-term of the n^{th} species. Furthermore, the Lewis numbers used here are also equal to unity, which is generally adopted when non-premixed flamelet models are used in a turbulent combustion application. As a consequence, preferential diffusion effects are absent. The local stretch rate K_M is governed by [87]:

$$\rho \frac{\partial K_M}{\partial t} + \rho u_1 \frac{\partial K_M}{\partial x_1} - \frac{\partial}{\partial x_1} \left(\mu \frac{\partial K_M}{\partial x_1} \right) = P(t) - \rho K_M^2, \quad (5.4)$$

where μ is the dynamic viscosity, P is the tangential pressure gradient, and is given by: cf. [15]:

$$P(t) = \rho_{\text{ox}} \left(\frac{\partial a(t)}{\partial t} + a(t)^2 \right), \quad (5.5)$$

with $a(t)$ the applied strain-rate, defined at the oxidizer boundary. If the oxidizer and fuel streams originate far away from the flame, then the flow-field can be assumed to behave as a potential flow, with a prescribed velocity gradient a :

$$\frac{\partial u_1}{\partial x_1} = -a \quad \text{and} \quad K_M = \frac{\partial u_2}{\partial x_2} = a \quad \text{at} \quad x_1 = L. \quad (5.6)$$

The boundaries are defined at $x_1 = -L$ and $x_1 = L$ and at $x_1 = 0$ a stagnation plane exists. The fuel (at $x_1 = -L$) and oxidizer (at $x_1 = L$) composition are chosen to be the same as in the Sandia flames [3] (see table 5.1).

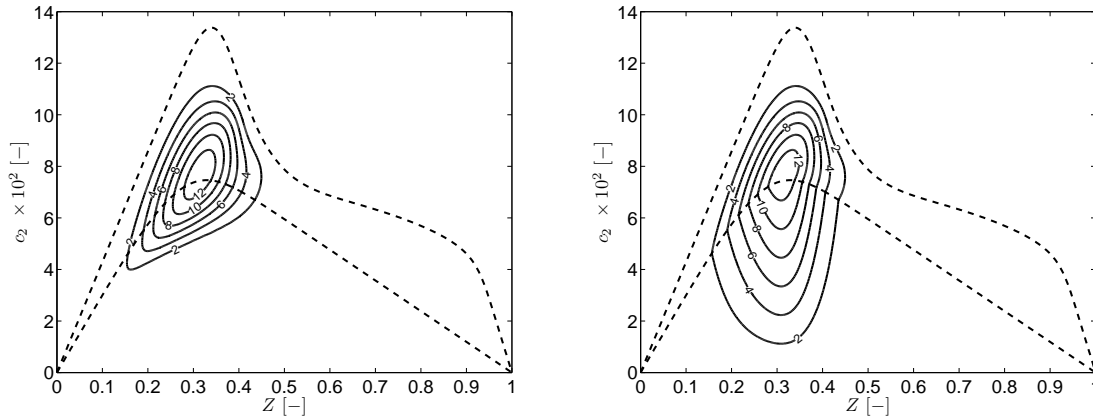


Figure 5.1: Two contour-plots of the chemical source-term $\dot{w}_{c_2}(c_1, c_2)$. The left figure shows a contour-plot of a 2D FGM that includes the extinction continuation, which is denoted as 2D FGM^{EC}, while the figure on the right shows a contour-plot of a 2D FGM where a straightforward linear interpolation was used to extend the manifold beyond the steady extinction limit, which is denoted as 2D FGM^{LI}. The upper dashed line represents the flamelet with $a = 0.1 \text{ s}^{-1}$, which is close to chemical equilibrium and the lower dashed line represents the flamelet with $a = 1265 \text{ s}^{-1}$, which is near the extinction limit.

5.3 Flamelet-Generated Manifolds construction

In this section the generation of two different manifolds is presented. The first manifold is a 2D FGM that is primarily based on *steady* flamelet simulations but which is extended with an *unsteady* extinguishing flamelet simulation. A similar technique was also used in [75]. This *unsteady* extension presents a natural continuation of the *steady* 2D FGM to cover the range beyond the steady extinction limit and is presented in subsection 5.3.1. The second manifold is a 3D FGM that is generated from *unsteady* flamelet simulations subjected to a sinusoidally varying strain-rate $a(t)$. The generation of this 3D FGM is discussed in subsection 5.3.2.

5.3.1 Constructing a 2D FGM beyond the steady extinction limit

A series of steady flames, with different strain-rates a is computed. The strain-rate was varied in gradual steps from 0.1 s^{-1} , i.e., close to chemical equilibrium, to 1265 s^{-1} , which is near the extinction limit for these flames. To extend the manifold beyond the steady extinction limit, the manifold is extended with an unsteady extinguishing flamelet. A step-change in the strain-rate to a value of $a = 1365 \text{ s}^{-1}$ is applied, which will cause the flamelet to extinguish. The large increase of the strain-rate, combined with the resulting decrease in temperature will cause all chemical source-terms to vanish and the remaining trajectory will correspond to extinction with simple cooling down. This extinction trajectory is subsequently used to extend the ‘steady’ manifold to also

include extinction. It was observed that in the state space, the trajectories of extinguishing flamelets are insensitive to the amplitude of the applied step in the initial strain-rate. The combination of the steady flamelet simulations and the unsteady extinguishing flamelet forms a two-dimensional Flamelet-Generated Manifold. An example of such a 2D FGM can be seen in figure 5.1, where two contour-plots of the chemical source-term $\dot{\omega}_{c_2}(c_1, c_2)$ are shown. Figure 5.1 (left) shows a contour-plot of a 2D FGM that includes the extinction continuation, which is denoted as 2D FGM^{EC}, while figure 5.1 (right) shows a contour-plot of a 2D FGM where a straightforward linear interpolation was used to extend the manifold beyond the steady extinction limit, which is denoted as 2D FGM^{LI}. The first controlling variable was chosen to be the mixture fraction $c_1 = Z$ and for the second controlling variable c_2 the mass-fraction of CO₂ was chosen, since it is monotonously increasing in the area of interest, i.e., around $a = 1250 \text{ s}^{-1}$. The *steady* part of the 2D FGM is bounded by two steady solutions, i.e., the upper dashed line represents a flamelet that is almost in chemical equilibrium and the lower dashed line is a flamelet very close to the steady extinction limit. Note that the contours of the chemical source-term of the 2D FGM^{EC} show a smooth transition between the *steady* part of the FGM and the *unsteady* part, which lies below the lower dashed line and is generated from an extinguishing flamelet, while the contours of the 2D FGM^{LI} show an obvious slope discontinuity. This can also be seen in figure 5.2, where a cross-section of the 2D FGM^{EC} and the 2D FGM^{LI} at $c_1 = Z_{\text{st}} = 0.3528$ are shown. Figure 5.2 shows the temperature and the chemical source-term of the second controlling variable as a function c_2 , viz., $T(c_2 | c_1 = Z_{\text{st}})$ and $\dot{\omega}_{c_2}(c_2 | c_1 = Z_{\text{st}})$. The curves consist of two parts; the solid lines with open markers represent the *steady* part and the solid line with filled markers represents the trajectory of the extinguishing flamelet, i.e., the 2D FGM^{EC} with $a = 1365 \text{ s}^{-1}$. Another extinguishing flamelet (open triangles) can also be seen, where a step-change in the strain-rate to a value of $a = 2000 \text{ s}^{-1}$ is applied. As can be seen, both extinguishing flamelets with $a = 1365 \text{ s}^{-1}$ and $a = 2000 \text{ s}^{-1}$ follow approximately the same trajectory. Also shown are straightforward linear interpolations that include the extinguished state (dashed lines), i.e., the 2D FGM^{LI}.

5.3.2 Constructing a 3D FGM

A series of unsteady flames with the same boundary conditions as for the steady case, but now with a sinusoidally varying strain-rate is computed. The strain-rate parameters which are varied are: the amplitude Δa , the mean value of the strain-rate \bar{a} , which is given as $\bar{a} = a_0 - \Delta a$ with a_0 the initial strain-rate value and the frequency f . During these unsteady flamelet simulations, the amplitude Δa was varied between $\Delta a = 10 \text{ s}^{-1}$ and $\Delta a = 50 \text{ s}^{-1}$, the frequency f varied between $f = 250 \text{ Hz}$ and $f = 1250 \text{ Hz}$, while the mean strain-rate remained constant at $\bar{a} = 1250 \text{ s}^{-1}$. These oscillating flames with varying \bar{a} , Δa and f are subsequently used to generate a manifold. The third controlling variable is chosen to be $c_3 = Y_{\text{H}_2\text{O}} - 8Y_{\text{H}_2} - 2Y_{\text{OH}}$. The reason behind this specific choice is given below.

The storage and retrieval can be done in a number of ways [16, 78, 90]. Here an approach is employed that is very similar to the one Turányi introduced in [90], where polynomials are used to describe the dependent manifold variables as functions of the controlling

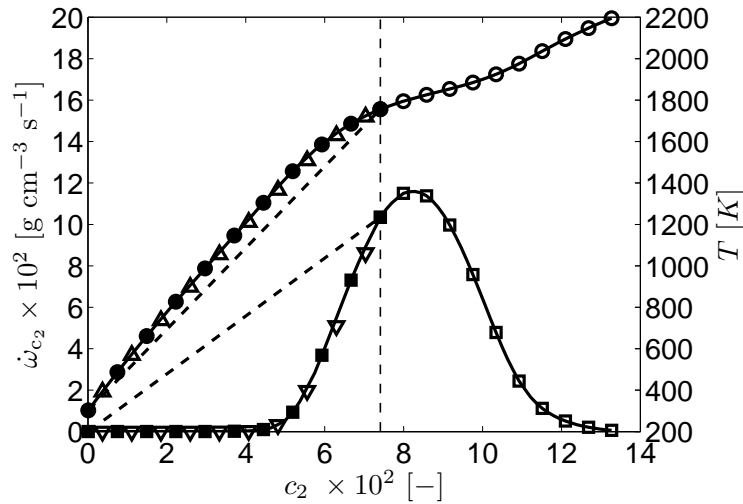


Figure 5.2: Temperature $T(c_2 | c_1 = Z_{st})$ and chemical source-term of the second controlling variable $\dot{\omega}_{c_2}(c_2 | c_1 = Z_{st})$. Shown are: the *steady* part of the 2D FGM (T : solid line with open squares, $\dot{\omega}_{c_2}$: solid line with open circles), the *unsteady* extinguishing flamelet trajectory with $a = 1365 \text{ s}^{-1}$, i.e., the 2D FGM^{EC} (T : solid line with filled squares, $\dot{\omega}_{c_2}$: solid line with filled circles) and the linear interpolation (dashed lines), i.e., the 2D FGM^{LI}. Another extinguishing flamelet (open triangles) can also be seen, where a step-change in the strain-rate to a value of $a = 2000 \text{ s}^{-1}$ is applied. The vertical thin dashed line signifies the steady extinction limit.

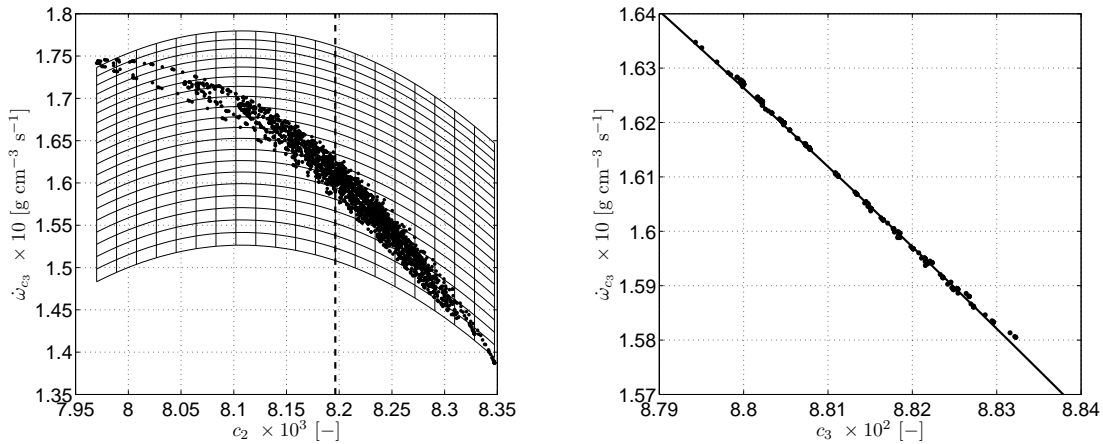


Figure 5.3: The chemical source-term of the third controlling variable $\dot{\omega}_{c_3}(c_2, c_3 | c_1 = Z_{st})$ (left) and $\dot{\omega}_{c_3}(c_3 | c_1 = Z_{st}, c_2 = 8.2 \times 10^{-3})$ (right). The mean strain-rate is $\bar{a} = 1250 \text{ s}^{-1}$ and the amplitude was varied between $\Delta a = 10 \text{ s}^{-1}$ and $\Delta a = 50 \text{ s}^{-1}$. Various frequencies were studied, ranging from 250 Hz to 1250 Hz.

variables. A least squares fitting approach is used here to determine the polynomial coefficients, which are stored for the dependent manifold variables. Because it is very

difficult to describe all the data at once, a piecewise least squares fit is performed for discrete c_1 values. In chapter 4, a different approach to store and retrieve the 3D manifold data was employed. All the data was stored in a 2D array, at discrete c_1 and c_2 values, and a linear extrapolation was used to retrieve the full 3D data. In this chapter however, the polynomial data is stored only at discrete c_1 values, which results in a database that is approximately 10 times smaller than the one used in chapter 4. Furthermore, as a direct result of this trimmed down database, the look-up process is also significantly faster. A typical example can be seen in figure 5.3, where the chemical source-term of the third controlling variable $\dot{\omega}_{c_3}(c_2, c_3 | c_1 = Z_{st})$ (left) and $\dot{\omega}_{c_3}(c_3 | c_1 = Z_{st}, c_2 = 8.2 \times 10^{-3})$ (right) are shown. In the left figure, the dots represent all the encountered compositions during all the unsteady flame simulations for which $c_1 = Z_{st}$ and the mesh represents a piecewise least squares fitted curved surface. In the right figure, an cross-section with $c_1 = Z_{st}$ and $c_2 = 8.2 \times 10^{-3}$ is shown, where the dots represent all the encountered compositions during all the unsteady flame simulations for which $c_1 = Z_{st}$ and $c_2 = 8.2 \times 10^{-3}$, which corresponds to the vertical dashed line in figure 5.3 (left). The solid line is an cross-section of a curved surface fit, which is second order in both c_2 and c_3 . As said, the 3D manifold was generated by performing a lot of different detailed simulations, where the strain-rate parameters, i.e., the initial strain-rate, the applied amplitude and the frequency, were varied, while the mean strain-rate was chosen constant. Therefore, many different combinations of the strain-rate parameters are included in the 3D manifold. This can also be seen in figure 5.3 (left), which shows that even when the initial strain-rate a_0 , the amplitude Δa and the frequency f are different for each simulation, the chemical source-term of the third controlling variable $\dot{\omega}_{c_3}$ is still uniquely parameterized by c_1 , c_2 and c_3 . Hence, a broad range of the strain-rate parameters can be accurately predicted using this 3D FGM.

Concerning the third controlling variable, two important quality criteria have to be taken into account. These two criteria are:

1. Application of the 3D manifold should be numerically stable.
2. The manifold should be well-conditioned.

The first criterion implies that when $\Delta c_3 = c_3 - c_3^{2D}$ is positive then $\Delta \dot{\omega}_{c_3} = \dot{\omega}_{c_3} - \dot{\omega}_{c_3}^{2D}$ should be negative during application of the 3D manifold. This means that:

$$J = \frac{\partial \Delta \dot{\omega}_{c_3}}{\partial \Delta c_3} < 0. \quad (5.7)$$

Regarding the second criterion, the condition number can be defined as follows:

$$C = \left\| \frac{xf'(x)}{f(x)} \right\| = \left\| \frac{\Delta c_3}{\Delta \dot{\omega}_{c_3}} \right\| \|J\|. \quad (5.8)$$

When the condition number is low, the problem is well-conditioned and in this case this means that absolute value of J should be smaller than some critical value J_{crit} :

$$\|J\| < J_{crit}. \quad (5.9)$$

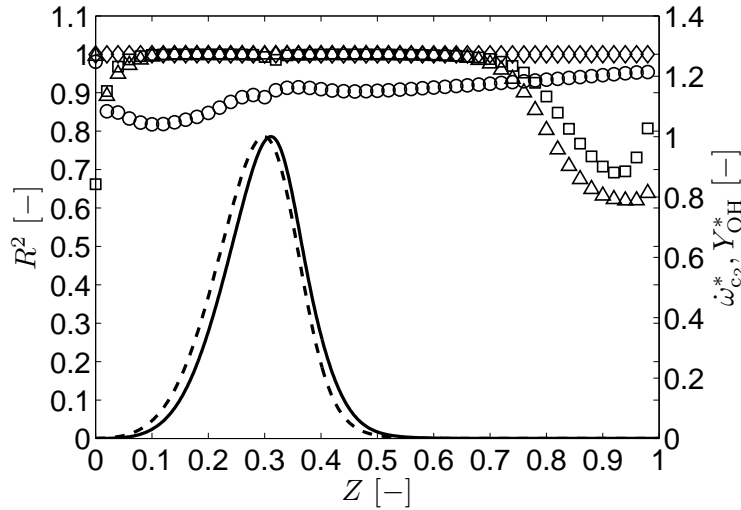


Figure 5.4: Coefficient of determination for the chemical source-term $\dot{\omega}_{c_2}$ (squares), the temperature T (diamonds), the mass-fraction of OH (triangles) and the mass-fraction of NO (circles). Also shown are the chemical source-term of c_2 (solid line) and the mass fraction of OH (dashed line). Both are scaled with their maximum values, respectively.

Applying these two criteria, the third controlling variable is chosen here as $c_3 = Y_{\text{H}_2\text{O}} - 8Y_{\text{H}_2} - 2Y_{\text{OH}}$. It should be noted that c_3 has been tuned such that it obeys the two aforementioned criteria. As a result, since this method is not an automated procedure, there may well be other (equally) successful choices.

The coefficient of determination R^2 , gives an indication, albeit a global one, on how well the data is represented by the least squares fit. The accuracy of the fit is related to the sum of squares of residuals:

$$R^2 = 1 - \frac{\text{RSS}}{\text{TSS}} = 1 - \frac{\sum_{k=1}^{N_d} (\varphi_k - \hat{\varphi})^2}{\sum_{k=1}^{N_d} (\varphi_k - \bar{\varphi})^2}, \quad (5.10)$$

where N_d is the total number of data-points φ_k , $\hat{\varphi}$ is the least squares estimate and $\bar{\varphi}$ is the mean of all points φ_k . Generally, R^2 lies between 0 and 1, where 0 indicates no correlation between the FGM variables and the least squares fit and 1 means a perfect correlation. For most of the dependent variables, except for Y_{NO} , there appears to be a near perfect correlation between the data and the least squares fit, i.e., $R^2 > 0.99$ at $c_1 = Z_{\text{st}}$. This is shown in figure 5.4, where $R^2(c_1)$ is shown for the chemical source-term $\dot{\omega}_{c_2}$ (squares), the temperature T (diamonds), and the mass-fractions of OH (triangles) and NO (circles), respectively. As can be seen, the coefficient of determination is very close to 1 for most of the manifold variables for most of the domain. However, near the boundaries, i.e., close to $c_1 = 0$ and $c_1 = 1$, R^2 drops to values significantly lower than 1 for two of the manifold variables, i.e., for the chemical source-term of c_2 (solid line) and the mass-fraction of OH (dashed line). Both $\dot{\omega}_{c_2}$ and Y_{OH} are also shown in figure 5.4 and are scaled with their maximum values, respectively. It is clear that both $\dot{\omega}_{c_2}$ and Y_{OH} have very small values near the boundaries $c_1 = 0$ and $c_1 = 1$. This is probably the reason why the coefficient of determination becomes worse for these two variables near

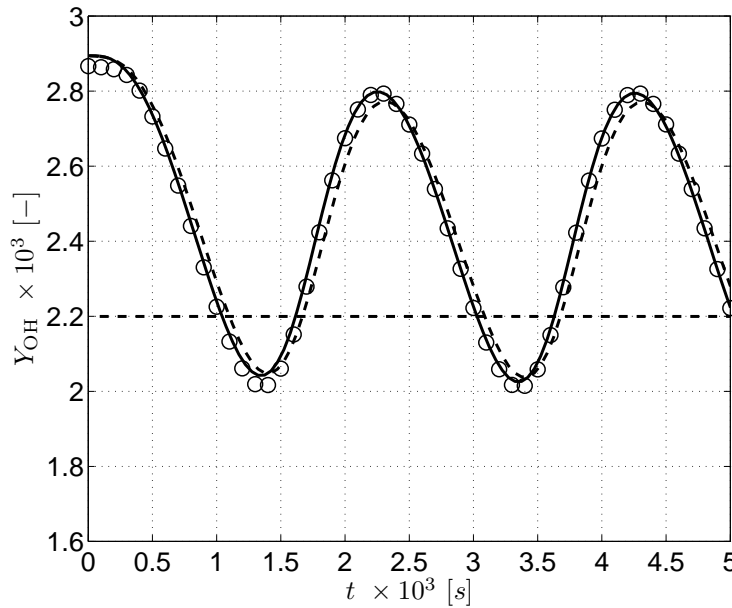


Figure 5.5: Comparison of Y_{OH} between the 2D manifold simulation (dashed line), the 3D manifold simulation (solid line with open circles) and the detailed simulation (solid line), with $\bar{a} = 1250 \text{ s}^{-1}$, $\Delta a = 40 \text{ s}^{-1}$ and $f = 500 \text{ Hz}$. Shown is $Y_{\text{OH}}(t | c_1 = Z_{\text{st}})$. The horizontal dashed line is the OH mass-fraction at the steady extinction limit for this flame.

the boundaries. Therefore a weighted average of R^2 is introduced:

$$R_{\phi,w}^2 = \frac{\int_0^1 R_{\phi}^2(c_1) \phi(c_1) dc_1}{\int_0^1 \phi(c_1) dc_1}. \quad (5.11)$$

In general it was found that $R_w^2 > 0.99$ for all of the dependent variables, except for Y_{NO} .

Because the compositions encountered during all the unsteady flame simulations lie close to the 3D fit, it can be concluded that it is indeed a 3D manifold. This is not the case with the mass-fraction of NO, where $R_w^2 = 0.90$ when a 3D FGM is used. Improving the accuracy of the NO predictions, is discussed in section 5.4.1.

5.4 FGM application and discussion

In this section results will be presented of an unsteady one-dimensional non-premixed counterflow flame. Detailed chemistry model simulations are compared with both the 2D FGM^{EC} and 3D FGM simulations. Simulations where the 2D FGM^{LI} was used were also performed. However, all unsteady 2D FGM^{LI} simulations resulted in almost immediate extinction and therefore these results are not taken into account in the following.

The flame is subjected to a sinusoidally varying strain-rate with a frequency of $f = 500 \text{ Hz}$, an amplitude of $\Delta a = 40 \text{ s}^{-1}$ and a mean strain-rate of $\bar{a} = 1250 \text{ s}^{-1}$. Both the 2D

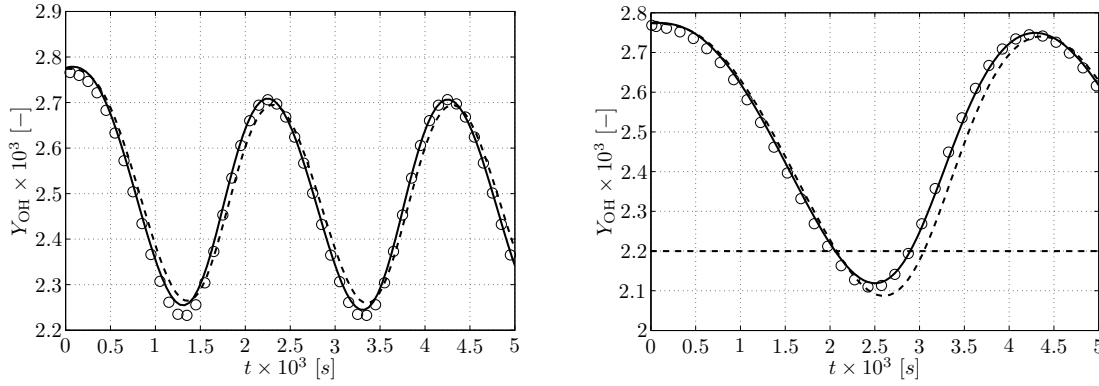


Figure 5.6: Comparison of Y_{OH} between the 2D manifold simulation (dashed line), the 3D manifold simulation (solid line with open circles) and the detailed simulation (solid line), with $\bar{a} = 1250 \text{ s}^{-1}$, $\Delta a = 25 \text{ s}^{-1}$ and $f = 500 \text{ Hz}$ (left) and $\bar{a} = 1250 \text{ s}^{-1}$, $\Delta a = 25 \text{ s}^{-1}$ and $f = 250 \text{ Hz}$ (right). Shown is $Y_{OH}(t | c_1 = Z_{st})$. The horizontal dashed line is the OH mass-fraction at the steady extinction limit for this flame.

FGM^{EC} and the 3D FGM are applied and compared to a detailed chemistry simulation. A typical result can be seen in figure 5.5, where the mass-fraction $Y_{OH}(t | c_1 = Z_{st})$ is shown. The solid line is the detailed chemistry simulation, the dashed line the 2D FGM^{EC} simulation and the circles the 3D FGM simulation. As can be seen, the 2D FGM^{EC} simulation shows a slight phase-shift compared to both the 3D FGM and the detailed chemistry simulations. Nonetheless, both the 2D FGM^{EC} and the 3D FGM simulations show good agreement with the detailed chemistry simulation, even at very high strain-rates. Note that the steady extinction limit is exceeded for all three simulations and that both the FGM simulations are able to capture this behavior well. Figure 5.6 shows the results of another two simulations, where different strain-rate parameters were used, i.e., $\bar{a} = 1250 \text{ s}^{-1}$, $\Delta a = 25 \text{ s}^{-1}$ and $f = 500 \text{ Hz}$ (left) and $\bar{a} = 1250 \text{ s}^{-1}$, $\Delta a = 25 \text{ s}^{-1}$ and $f = 250 \text{ Hz}$ (right) and the same trends as in figure 5.5 can be seen. Note that the analysis until so far, is done for only one value of c_1 . In order to avoid repeating this analysis for each discrete value of c_1 , the integral source-term Ω_{c_2} is introduced, which is defined as:

$$\Omega_{c_2}(t) = \int_{-L}^L \dot{\omega}_{c_2}(x_1, t) dx_1, \quad (5.12)$$

and indicates the global net production of c_2 throughout the flamelet. Figure 5.7 shows the integral chemical source-term $\Omega_{c_2}(t)$. The solid line is the detailed chemistry simulation, the dashed line the 2D FGM^{EC} simulation and the circles the 3D FGM simulation. It can be seen that the 3D FGM simulation predicts the detailed chemistry case better than the 2D FGM^{EC} simulation does. Specifically, the phase-shift between the detailed chemistry case and the 2D FGM^{EC} simulation does not exist between the detailed chemistry case and the 3D FGM simulation. And apart from the initial response, the 3D FGM simulation follows the detailed chemistry case very well.

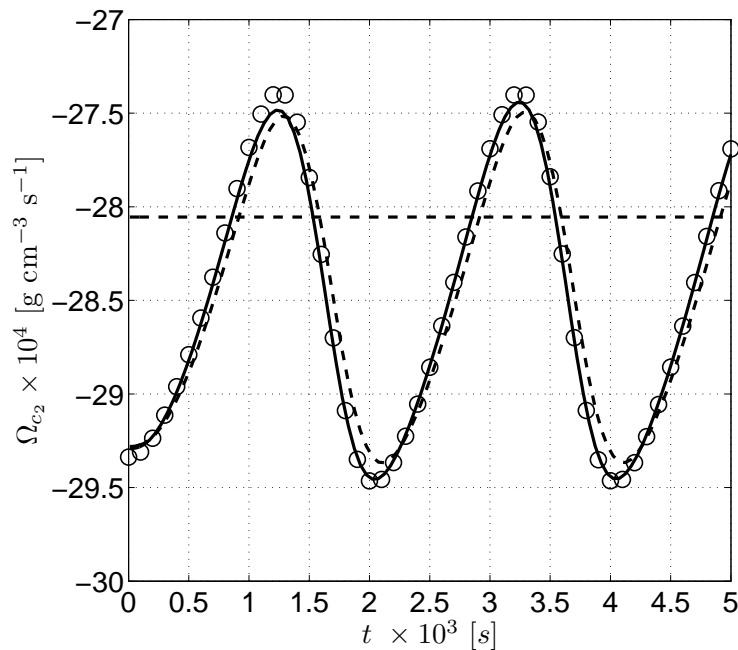


Figure 5.7: Comparison of the integral source-term Ω_{c_2} between the 2D manifold simulation (dashed line), the 3D manifold simulation (circles) and the detailed simulation (solid line), with $\bar{a} = 1250 \text{ s}^{-1}$, $\Delta a = 40 \text{ s}^{-1}$ and $f = 500 \text{ Hz}$. The horizontal dashed line denotes the steady extinction limit for this flame.

5.4.1 Prediction of species with slow chemical time-scales

A more challenging group of species to predict using a manifold method is the group of species related to the slowest processes occurring in combustion, e.g., NO. Because of the slow chemical time-scales, the mass-fraction of NO does not relax towards a low-dimensional manifold as fast as most of the other species do. This results in an increase of the manifold dimension regarding NO. One way of predicting the mass-fraction of NO is by using a post-processing method [28], but here it is shown that it is also possible to retrieve the mass-fraction of NO directly from a low-dimensional FGM.

Both a 2D FGM^{EC} as well as a 3D FGM have been applied to predict the NO mass-fraction and the results were compared with a simulation using a detailed chemistry model. The methodology used here is the same as explained in section 5.3. Figure 5.8 shows $Y_{\text{NO}}(t | c_1 = Z_{\text{st}})$, with $\bar{a} = 1250 \text{ s}^{-1}$, $\Delta a = -25 \text{ s}^{-1}$ and $f = 500 \text{ Hz}$. The solid line is the detailed chemistry simulation, the dashed line the 2D FGM^{EC} simulation and the circles the 3D FGM simulation. Now, both the 2D FGM^{EC} and the 3D FGM simulations show a phase-shift compared to the detailed chemistry simulation. Furthermore, the accuracy of the 2D FGM^{EC} and the 3D FGM simulations are comparable, the undershoot of the 3D FGM simulation is even larger than the undershoot of the 2D FGM^{EC} simulation. The accuracy might be improved by adding a fourth controlling variable c_4 . In order to introduce another controlling variable, the methodology of the least squares method is employed again.

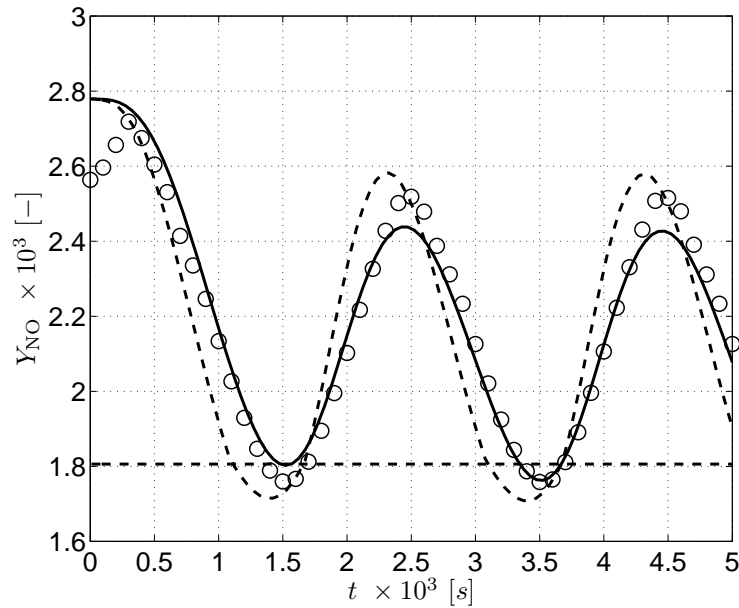


Figure 5.8: Comparison of Y_{NO} between the 2D manifold simulation (dashed line), the 3D manifold simulation (circles) and the detailed simulation (solid line), with $\bar{a} = 1250 \text{ s}^{-1}$, $\Delta a = 40 \text{ s}^{-1}$ and $f = 500 \text{ Hz}$. Shown is $Y_{\text{NO}}(t \mid c_1 = Z_{\text{st}})$.

The coefficient of determination for Y_{NO} when a 3D FGM is used is $R_w^2 = 0.90$. If however, one additional controlling variable $c_4 = Y_{\text{H}_2\text{O}}$ is added, the fit improves significantly, i.e., $R_w^2 = 0.98$. This means that when using a 4D FGM instead of a 3D FGM to predict NO mass-fractions, this may lead to a significant improvement. This will be the subject of further study.

5.5 Conclusions

The primary goal was to investigate whether local extinction and re-ignition can be captured and parameterized using Flamelet-Generated Manifolds. It was shown that both a 2D and a 3D FGM exist and that the manifold variables can be described using only two or three controlling variables.

Moreover, it was shown that it is possible to extend the 'steady' 2D FGM to also capture (a part of) the unsteady extinction trajectory, which resulted in a 2D FGM^{EC}. Additionally, a 3D FGM was constructed, based on flamelets subjected to a (temporally) sinusoidally varying strain-rate. The 3D manifold was subsequently generated, using polynomials. This provides an elegant method to generate a 3D FGM, which is able to reproduce unsteady effects, specifically close to and even beyond the steady extinction limit. It was shown that the generated 3D FGM includes a broad range of the strain-rate parameters, i.e., the amplitude, frequency and initial value of the strain-rate.

Two different Flamelet-Generated Manifolds were applied, i.e., a 2D FGM^{EC} that is primarily based on steady flamelets but was extended with an unsteady extinguishing flamelet and a 3D FGM that was generated from unsteady flamelet simulations subjected to sinusoidally varying strain-rates.

Concerning species related to the slowest chemical time-scales, e.g., NO, it can be concluded that using a 3D FGM does not lead to a significant improvement over using a 2D FGM^{EC}. However, due to the flexibility of the approach, it is relatively easy to improve this. Indeed, a preliminary analysis has shown that adding a fourth controlling variable, improved the coefficient of determination to a value that is comparable to that of the other manifold variables.

It can be concluded that the application of both manifolds yields similar results and that although the 3D FGM is a bit more accurate than the 2D FGM^{EC} the difference is not very large. The analysis and application of the manifold generated from unsteady flamelet simulations subjected to sinusoidally varying strain-rates does show however, that the major benefit lies in the potential to include more time-scales if needed.

In the current research all Lewis numbers are chosen equal to 1 as is the case for the classical diffusion flamelet approach and most flamelet applications in turbulent flame simulations. In the future, the impact of the transport model on the observations found here should be further studied. Furthermore, generation and application of a 4D FGM in order to predict NO mass-fractions more accurately should also be investigated.

Concluding remarks

In this thesis the Flamelet-Generated Manifolds method, initially developed for and successfully applied to premixed flames, is extended to non-premixed flames. In order to do so, in chapter 2 the laminar, premixed flamelet model of de Goeij and ten Thije Boonkkamp is introduced. The major difference between the flamelet model presented in chapter 2 and the flamelet model of de Goeij and ten Thije Boonkkamp is that the flamelet model presented in this thesis is a unified flamelet model, which is capable of describing both (partially) premixed flames as well as non-premixed flames. Analogous to the work of de Goeij and ten Thije Boonkkamp, the combustion problem is divided into three sub-problems; 1) fluid motion and mixing of enthalpy and elements, 2) the dynamics of the flame-front (described by a so-called principal controlling variable) and 3) the dynamics of the internal flame structure (described by a small number of additional controlling variables), which is attached to the flame-front. Furthermore, the set of equations has been decomposed in a natural way into normal and tangential contributions, of which the latter is often assumed to be negligible. Subsequently, it is explained how this unified flamelet model can be employed within the FGM concept. By simulating one-dimensional flames, a manifold can be constructed, and by adding more controlling variables, the number of time-scales that is incorporated in the manifold can also be increased. In that respect, the application of the FGM method is very similar to the ILDM approach.

In chapter 3 the individual contributions of the species conservation equation $T_{n,i}$ are analyzed numerically. Aside from stretching and curvature, which have been the subject of previous studies, tangential diffusion is also explicitly considered. By applying a flamelet analysis to three different detailed flame simulations, each of the individual contributions of the species conservation equation was numerically verified. These contributions consist of 1) an unsteady term, 2) normal transport, 3) stretch-rate effects, 4) curvature effects, 5) tangential diffusion and 6) a chemical source-term, which may be split in a production and a consumption term, respectively. Due to the unified nature of the flamelet model that was presented in chapter 2, the postprocessing procedure can be applied to both premixed flames, as well as to non-premixed flames. The only difference between the premixed case and the non-premixed flames is the choice of the principal controlling variable. In the premixed case, a product species was chosen, i.e.,

$\mathcal{Y} = Y_{\text{CO}_2}/Y_{\text{CO}_2}^{\text{burnt}}$, while in the non-premixed case the mixture fraction was chosen as primary controlling variable, i.e., $\mathcal{Y} = Z$. Apart from this, the rest of the postprocessing procedure is identical. The first test case is a freely expanding premixed flame embedded in a decaying turbulent flow-field. As a second test-case a so-called non-premixed reacting mixing layer was used and the final test-case was a steady non-premixed co-flow flame. For each of the test cases, one-dimensional flamelet paths were reconstructed, along which the individual contributions $T_{n,i}$ were evaluated. From the numerical results, it can be concluded that tangential diffusion is indeed very small, and neglecting this contribution does not lead to significant inaccuracies. Furthermore, besides normal transport and chemistry, flame stretch and curvature can also be important in both premixed and non-premixed flames and should therefore be taken into account when constructing an FGM. Finally, for the laminar co-flow flame, two different principal controlling variables were chosen, resulting in two different coordinate transformations, i.e., a typical non-premixed flame-adapted coordinate system and a typical premixed one. Compared to the coordinate transformation based on the mixture fraction, there are not too many differences. The major difference is of course that the flamelet paths for the latter transformation are much more like premixed flamelets, while the flamelet paths that were reconstructed using the mixture fraction, look like non-premixed flamelets. From the two unsteady flame simulations presented in chapter 3 it was concluded that the unsteady contribution can be significant. Therefore in chapters 4 and 5 it is studied whether unsteady flow-field effects can be incorporated and parameterized using Flamelet-Generated Manifolds.

In chapter 4 detailed simulations are performed for a series of steady and unsteady non-premixed flames. For each of the steady flamelet simulations, the strain-rate was different but constant. It was shown that the set of steady flamelet simulations span a two-dimensional attracting manifold in composition space that can be parameterized by $c_1 = Z$ and $c_2 = Y_{\text{CO}_2}$ or alternatively $c_1 = Z$ and $c_2 = \chi$, which is common for the classical flamelet approach. Using this 2D FGM, flamelets subjected to an oscillating strain-rate were simulated with both the classical $Z\chi$ – method as well as the Zc_2 – method. As a direct result of using only two parameters, a phase-shift occurs between the detailed simulation and the $Z\chi$ – method and Zc_2 – method simulations. Unsteady flamelet simulations were performed by subjecting each transient flamelet to a (temporally) sinusoidally varying strain-rate. By varying the strain-rate parameters, i.e., the initial strain-rate, the applied amplitude and the frequency, the influence of these strain-rate parameters on the dimensionality of the manifold is studied. It was concluded that the trajectories of the unsteady laminar diffusion flames are situated close to the 2D manifold. Furthermore, it was shown that for the relevant manifold variables, i.e., the chemical source-terms of c_2 and c_3 , as well as the temperature, density and the specific heat, it was possible to linearly extend the 2D FGM to a 3D FGM, using polynomials. This provides an elegant method of generating a 3D FGM, which is able to reproduce unsteady effects. Furthermore, it was concluded that when using a 3D FGM, the phase-lag that occurs when using a 2D FGM disappears.

The primary goal of chapter 5 was to investigate whether local extinction and re-ignition can be captured and parameterized using Flamelet-Generated Manifolds. It was concluded that both a 2D and a 3D FGM exist and that the manifold variables can be described using only two or three controlling variables. Furthermore, it was shown that it is possible to extend the ‘steady’ 2D FGM to also capture (a part of) the

unsteady extinction trajectory, which resulted in a 2D FGM^{EC}. Additionally, a 3D FGM was constructed, based on flamelets subjected to a (temporally) sinusoidally varying strain-rate. The 3D manifold was subsequently generated, using polynomials. This provides an elegant method to generate a 3D FGM, which is able to reproduce unsteady effects, specifically close to and even beyond the steady extinction limit. It was shown that the generated 3D FGM includes a broad range of the strain-rate parameters, i.e., the amplitude, frequency and initial value of the strain-rate. Unsteady one-dimensional flame simulations were performed, using detailed chemistry, a 2D FGM^{EC} and a 3D FGM that was generated from unsteady flamelet simulations subjected to sinusoidally varying strain-rates. Concerning species related to the slowest chemical time-scales, e.g., NO, it was concluded that using a 3D FGM does not lead to a significant improvement over using a 2D FGM^{EC}. However, due to the flexibility of the approach, it is relatively easy to improve this. Indeed, a preliminary analysis shows that adding a fourth controlling variable, improved the coefficient of determination to a value that is comparable to that of the other manifold variables where only three controlling variables were needed. Finally, it was concluded that the application of both manifolds yields similar results and that although the 3D FGM is a bit more accurate than the 2D FGM^{EC}, the difference is not very large. The analysis and application of the manifold generated from unsteady flamelet simulations subjected to sinusoidally varying strain-rates does show however, that the major benefit lies in the potential to include more time-scales if needed.

Transformation relations

When flames are considered, it is often useful to use a so-called flame adapted coordinate system, where coordinate surfaces correspond to flame surfaces. A flame can be defined as the region in the spatial domain, where $\mathcal{Y}_1 \leq \mathcal{Y} \leq \mathcal{Y}_2$ for a certain scalar variable \mathcal{Y} . The subscripts 1 and 2 indicate the two boundaries of the flame that are separated by the flame, i.e., for premixed flames these two sides correspond to the unburnt and the burnt side, respectively and for non-premixed flames these two sides would be the fuel and oxidizer side, respectively. Often, species mass fractions, or linear combinations of species mass fractions, are chosen as suitable controlling variable \mathcal{Y} for which $\nabla \mathcal{Y} \neq 0$ holds in the entire domain. Note that for premixed flames often product species are used as principal controlling variable, for instance the mass fraction of carbon dioxide $\mathcal{Y} = Y_{\text{CO}_2}$, while for non-premixed flames it is more common to use the mixture fraction as principal controlling variable, i.e., $\mathcal{Y} = Z$. Flame surfaces can now be defined as iso-surfaces of \mathcal{Y} where $\mathcal{Y}(x, t) = \mathcal{Y}_0$ for some constant \mathcal{Y}_0 . In general, flame surfaces are curved and wrinkled surfaces moving through Cartesian space. Therefore, fundamental transformation relations [89] from Cartesian coordinates to a general curvilinear system are developed in this section. Where needed, concepts of tensor analysis are introduced.

A.1 Covariant and contravariant base

Using the chain rule, the partial derivatives with respect to Cartesian coordinates can be related to the partial derivatives with respect to curvilinear coordinates, and may be written in either two ways:

$$\frac{\partial A}{\partial x_i} = \frac{\partial A}{\partial \xi^j} \frac{\partial \xi^j}{\partial x_i} \quad (i = 1, 2, 3) \quad (j = 1, 2, 3), \quad (\text{A.1})$$

or:

$$\frac{\partial A}{\partial \xi^i} = \frac{\partial A}{\partial x_j} \frac{\partial x_j}{\partial \xi^i} \quad (i = 1, 2, 3) \quad (j = 1, 2, 3). \quad (\text{A.2})$$

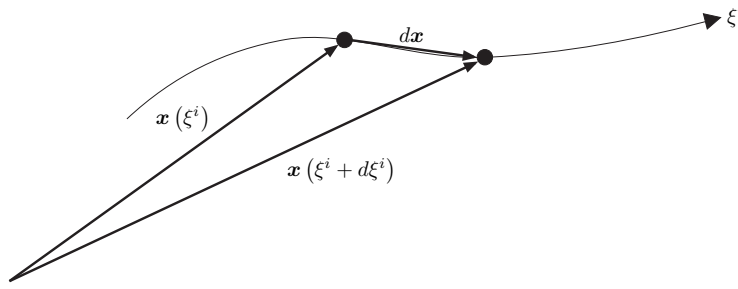


Figure A.1: Covariant basevectors.

Both formulations can be used to relate the Cartesian and curvilinear derivatives of a certain quantity A . In the first case, the derivative of ξ^i with respect to x has to be evaluated, being the normal of the surface with $\xi^i = \text{constant}$, i.e., $\nabla \xi^i$. In the second case, the derivative of x with respect to ξ^i has to be known, which is tangent to a ξ^i -line, i.e., $\frac{\partial x}{\partial \xi^i}$. In other words, transformation relations may be based on either of these two sets of vectors.

Curvilinear coordinate lines are curves formed by the intersection of surfaces on which one coordinate is constant. This means that one coordinate varies along this curve, while the two others remain constant. The **normals** to the coordinate surfaces define the so-called **contravariant basis vectors**, while the **tangents** to the coordinate lines are used to define the so-called **covariant basis vectors** of the curvilinear system.

Figure A.1 shows a coordinate line of increasing ξ^i . The tangent vector to this coordinate line is given by:

$$\lim_{d\xi^i \rightarrow 0} \frac{x(\xi^i + d\xi^i) - x(\xi^i)}{d\xi^i} = \frac{\partial x}{\partial \xi^i}, \quad (\text{A.3})$$

which defines the three **covariant** basis vectors:

$$\mathbf{a}_i = \frac{\partial x_j}{\partial \xi^i} \quad (i = 1, 2, 3) \quad (j = 1, 2, 3). \quad (\text{A.4})$$

The subscript i indicates the basis vector tangent to the line along which ξ^i varies. Figure A.2 shows the normal vector to the coordinate surface on which ξ^i is constant, which is given by $\nabla \xi^i$. The three normal vectors to the coordinate surfaces define the **contravariant** basis vectors as follows:

$$\mathbf{a}^i = \frac{\partial \xi^i}{\partial x_j} \quad (i = 1, 2, 3) \quad (j = 1, 2, 3), \quad (\text{A.5})$$

where the superscript i indicates the basis vector normal to the surface of constant ξ^i .

Both the covariant and contravariant basis vectors are illustrated in figure A.3, which shows a volume element where the six sides correspond to coordinate surfaces. Note that the covariant and contravariant basis vectors are not necessarily parallel to each other. For orthogonal systems however, the two sets of basis vectors will be parallel.

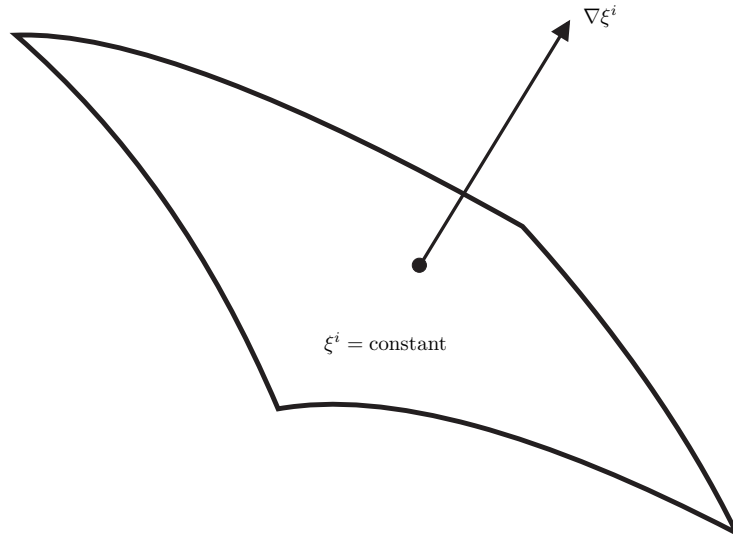


Figure A.2: Contravariant basevectors.

Furthermore, the so-called covariant metric tensor is a 3×3 matrix and is given by:

$$\mathbf{g}_{ij} = \begin{pmatrix} g_{11} & g_{12} & g_{13} \\ g_{21} & g_{22} & g_{23} \\ g_{31} & g_{32} & g_{33} \end{pmatrix}, \quad (\text{A.6})$$

where the components are defined as:

$$g_{ij} = \mathbf{a}_i \cdot \mathbf{a}_j = g_{ji}, \quad (i = 1, 2, 3), (j = 1, 2, 3). \quad (\text{A.7})$$

For orthogonal systems, the three basis vectors of each type are mutually perpendicular, which means that g_{ij} only has non-zero components along its diagonal. The components for the contravariant metric tensor can likewise be written as:

$$g^{ij} = \mathbf{a}^i \cdot \mathbf{a}^j = g^{ji}, \quad (i = 1, 2, 3), (j = 1, 2, 3). \quad (\text{A.8})$$

A.1.1 Line increment

The general differential increment of a position vector, not necessarily on a coordinate line, can be written as:

$$\begin{aligned} d\mathbf{x} &= \frac{\partial \mathbf{x}}{\partial \xi^1} d\xi^1 + \frac{\partial \mathbf{x}}{\partial \xi^2} d\xi^2 + \frac{\partial \mathbf{x}}{\partial \xi^3} d\xi^3, \\ &= \sum_{i=1}^3 \frac{\partial \mathbf{x}}{\partial \xi^i} d\xi^i = \sum_{i=1}^3 \mathbf{a}_i d\xi^i, \end{aligned} \quad (\text{A.9})$$

On a coordinate line along which only ξ^i varies, i.e., ξ^j and ξ^k are constant, the increment of arc length is given by:

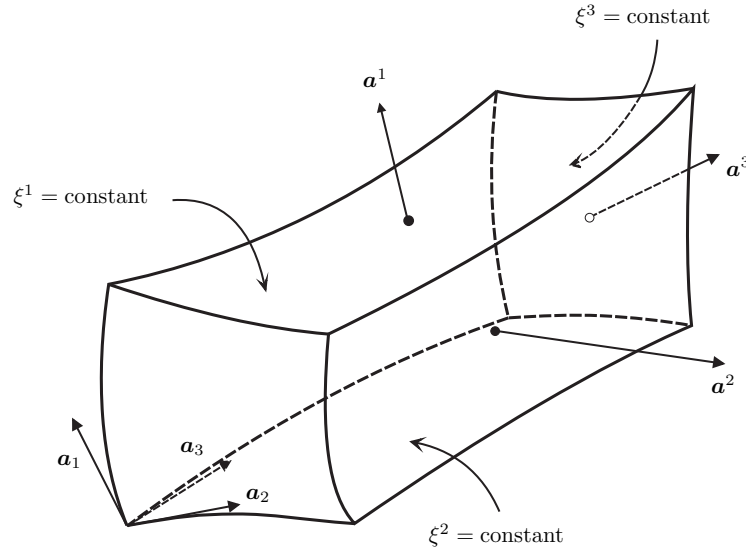


Figure A.3: Volume element showing the relations between covariant and contravariant basis vectors.

$$\begin{aligned}
 |ds^i| &= \left| \frac{\partial \mathbf{x}}{\partial \xi^i} \right| d\xi^i, \\
 &= |\mathbf{a}_i| d\xi^i, \\
 &= \sqrt{g_{ii}} d\xi^i,
 \end{aligned} \tag{A.10}$$

with

$$|\mathbf{a}_i| = \sqrt{\mathbf{a}_i \cdot \mathbf{a}_i} = \sqrt{g_{ii}}. \tag{A.11}$$

A.1.2 Surface increment

An increment of area on a coordinate surface with constant ξ^i is then given by:

$$\begin{aligned}
 |dS^i| &= |ds^j \times ds^k|, \\
 &= |\mathbf{a}_j \times \mathbf{a}_k| d\xi^j d\xi^k.
 \end{aligned} \tag{A.12}$$

Using:

$$\begin{aligned}
 |\mathbf{a}_j \times \mathbf{a}_k|^2 &= (\mathbf{a}_j \times \mathbf{a}_k) \cdot (\mathbf{a}_j \times \mathbf{a}_k), \\
 &= (\mathbf{a}_j \cdot \mathbf{a}_j)(\mathbf{a}_k \cdot \mathbf{a}_k) - (\mathbf{a}_j \cdot \mathbf{a}_k)(\mathbf{a}_k \cdot \mathbf{a}_j), \\
 &= (\mathbf{a}_j \cdot \mathbf{a}_j)(\mathbf{a}_k \cdot \mathbf{a}_k) - (\mathbf{a}_j \cdot \mathbf{a}_k)^2, \\
 &= g_{jj}g_{kk} - g_{jk}^2,
 \end{aligned} \tag{A.13}$$

where the following vector identity was applied:

$$(\mathbf{A} \times \mathbf{B}) \cdot (\mathbf{C} \times \mathbf{D}) = (\mathbf{A} \cdot \mathbf{C})(\mathbf{B} \cdot \mathbf{D}) - (\mathbf{A} \cdot \mathbf{D})(\mathbf{B} \cdot \mathbf{C}), \quad (\text{A.14})$$

means that (A.12) can finally be written as follows:

$$\left| dS^i \right| = \sqrt{g_{jj}g_{kk} - g_{jk}^2} d\xi^j d\xi^k, \quad (i = 1, 2, 3), (i, j, k) \text{ cyclic.} \quad (\text{A.15})$$

The normal vector \mathbf{n}^i is perpendicular to the plane with constant ξ^i , i.e., it is perpendicular to the plane spanned by the two vectors \mathbf{a}_j and \mathbf{a}_k , and it is defined as:

$$\mathbf{n}^i = \pm \frac{\mathbf{a}_j \times \mathbf{a}_k}{|\mathbf{a}_j \times \mathbf{a}_k|}. \quad (\text{A.16})$$

This leads to:

$$\mathbf{n}^i \left| dS^i \right| = \pm \mathbf{a}_j \times \mathbf{a}_k d\xi^j d\xi^k. \quad (\text{A.17})$$

The choice of the sign depends on the location of the volume relative to the surface.

A.1.3 Volume increment

The Jacobian of the transformation, $\sqrt{g} = \det |g_{ij}|$ can be found by considering the volume of an element like the one shown in figure A.3, as follows:

$$\begin{aligned} dV &= \mathbf{r}_{\xi^i} \cdot (\mathbf{r}_{\xi^j} \times \mathbf{r}_{\xi^k}) d\xi^i d\xi^j d\xi^k, \quad (i, j, k) \text{ cyclic} \\ &= \mathbf{a}_1 \cdot (\mathbf{a}_2 \times \mathbf{a}_3) d\xi^1 d\xi^2 d\xi^3. \end{aligned} \quad (\text{A.18})$$

Consider the vector identities:

$$(\mathbf{A} \times \mathbf{B}) \cdot (\mathbf{C} \times \mathbf{D}) = (\mathbf{A} \cdot \mathbf{C})(\mathbf{B} \cdot \mathbf{D}) - (\mathbf{A} \cdot \mathbf{D})(\mathbf{B} \cdot \mathbf{C}), \quad (\text{A.19})$$

which is a scalar, and:

$$\mathbf{A} \times (\mathbf{B} \times \mathbf{C}) = (\mathbf{A} \cdot \mathbf{C})\mathbf{B} - (\mathbf{A} \cdot \mathbf{B})\mathbf{C}, \quad (\text{A.20})$$

which is a vector. These identities can be used to rewrite square of $\mathbf{a}_1 \cdot (\mathbf{a}_2 \times \mathbf{a}_3)$ as follows:

$$[\mathbf{a}_1 \cdot (\mathbf{a}_2 \times \mathbf{a}_3)]^2 = -|\mathbf{a}_1 \times (\mathbf{a}_2 \times \mathbf{a}_3)|^2 + (\mathbf{a}_1 \cdot \mathbf{a}_1) \{(\mathbf{a}_2 \times \mathbf{a}_3) \cdot (\mathbf{a}_2 \times \mathbf{a}_3)\}, \quad (\text{A.21})$$

where (A.19) was applied, with:

$$\begin{aligned} \mathbf{A} &= \mathbf{C} = \mathbf{a}_1, \\ \mathbf{B} &= \mathbf{D} = \mathbf{a}_2 \times \mathbf{a}_3. \end{aligned}$$

When (A.19) is applied again, as well as (A.20), this leads to:

$$\begin{aligned}
[\mathbf{a}_1 \cdot (\mathbf{a}_2 \times \mathbf{a}_3)]^2 &= - |(\mathbf{a}_1 \cdot \mathbf{a}_2)\mathbf{a}_3 - (\mathbf{a}_1 \cdot \mathbf{a}_3)\mathbf{a}_2|^2 + \\
&\quad (\mathbf{a}_1 \cdot \mathbf{a}_1) \left\{ (\mathbf{a}_2 \cdot \mathbf{a}_2)(\mathbf{a}_3 \cdot \mathbf{a}_3) - (\mathbf{a}_2 \cdot \mathbf{a}_3)^2 \right\}, \\
&= -(g_{12}\mathbf{a}_3 - g_{13}\mathbf{a}_2) \cdot (g_{12}\mathbf{a}_3 - g_{13}\mathbf{a}_2) + g_{11}(g_{22}g_{33} - g_{23}^2), \\
&= g_{11}(g_{22}g_{33} - g_{23}^2) - g_{12}(g_{12}g_{33} - g_{13}g_{23}) + g_{13}(g_{12}g_{23} - g_{13}g_{22}), \tag{A.22}
\end{aligned}$$

which happens to be the determinant of the covariant metric tensor g_{ij} . This means that the Jacobian of the transformation can be written as:

$$\sqrt{g} = \sqrt{\det |g_{ij}|} = \mathbf{a}_1 \cdot (\mathbf{a}_2 \times \mathbf{a}_3). \tag{A.23}$$

Relation (A.18) now becomes:

$$dV = \sqrt{g} d\xi^1 d\xi^2 d\xi^3. \tag{A.24}$$

A.2 Differential operators in a generalized curvilinear space

Various derivative operators can be derived by applying the divergence theorem [46]:

$$\iiint_V \nabla \cdot \mathbf{A} dV = \iint_S \mathbf{A} \cdot \mathbf{n} dS, \tag{A.25}$$

where $\mathbf{n}^i |dS^i|$ is given by (A.17). This leads to the following expression:

$$\begin{aligned}
\iiint_{dV} \nabla \cdot \mathbf{A} \sqrt{g} d\xi^1 d\xi^2 d\xi^3 &= \sum_{i=1}^3 \left\{ \iint_{dS^i_+} \mathbf{A} \cdot (\mathbf{a}_j \times \mathbf{a}_k) d\xi^j d\xi^k - \right. \\
&\quad \left. \iint_{dS^i_-} \mathbf{A} \cdot (\mathbf{a}_j \times \mathbf{a}_k) d\xi^j d\xi^k \right\}, \quad (i, j, k) \text{ cyclic.} \tag{A.26}
\end{aligned}$$

For the limit that $d\xi^1 d\xi^2 d\xi^3 \rightarrow 0$, this becomes:

$$\nabla \cdot \mathbf{A} = \frac{1}{\sqrt{g}} \sum_{i=1}^3 [(\mathbf{a}_j \times \mathbf{a}_k) \cdot \mathbf{A}]_{\xi^i}, \quad (i, j, k) \text{ cyclic}, \tag{A.27}$$

where $[\dots]_{\xi^i}$ indicates the derivative with respect to ξ^i . The same applies to a scalar A :

$$\nabla A = \frac{1}{\sqrt{g}} \sum_{i=1}^3 [(\mathbf{a}_j \times \mathbf{a}_k) A]_{\xi^i}, \quad (i, j, k) \text{ cyclic.} \tag{A.28}$$

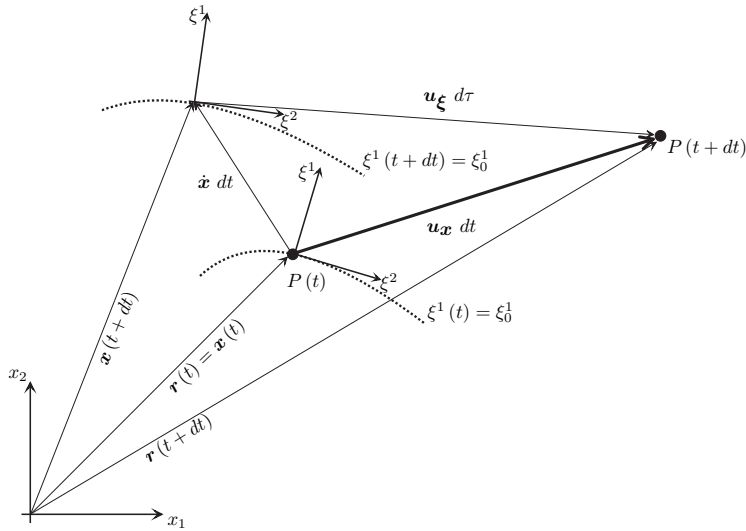


Figure A.4: Schematic representation of a displacement vector $u_x dt$, indicating the displacement of a particle P from initial position $x(t)$ to position $x(t+dt)$. Also shown are the displacement vector of the curvilinear coordinate system $\dot{x} dt$ and the displacement vector of particle P with respect to the curvilinear coordinate system $u_\xi d\tau$. From the laws of vector addition it follows that $u_\xi = u_x - \dot{x}$.

The Laplacian can now also be derived:

$$\begin{aligned} \nabla \cdot (b \nabla A) &= \nabla \cdot \left(\frac{b}{\sqrt{g}} \sum_{l=1}^3 [(a_m \times a_n) A]_{\xi^l} \right), \\ &= \frac{b}{\sqrt{g}} \sum_{i=1}^3 \left[(a_j \times a_k) \cdot \left(\frac{1}{\sqrt{g}} \sum_{l=1}^3 [(a_m \times a_n) A]_{\xi^l} \right) \right]_{\xi^i}, \end{aligned} \quad (\text{A.29})$$

$(i, j, k), (l, m, n)$ cyclic.

It has to be noted that the identity:

$$\sum_{i=1}^3 [a_j \times a_k]_{\xi^i} = 0, \quad (i, j, k) \text{ cyclic}, \quad (\text{A.30})$$

can be used, which leads to the so-called non-conservative derivative operators.

A.2.1 Time derivative

Since a material derivative is independent from the coordinate system, the time-derivative with respect to the Cartesian coordinate system is related to the time-derivative with respect to the curvilinear coordinate system via the material derivative. The material derivative can be expressed as a function of the Cartesian coordinate

system [46] and for a scalar quantity A this leads to:

$$\frac{DA}{Dt} = \frac{\partial A}{\partial t} + \mathbf{u}_x \cdot \nabla A, \quad (\text{A.31})$$

where the first part represents the local rate of change at a fixed position in Cartesian space. The second part is the so-called advective derivative, which results from the fact that when an element is advected from one position to the other with velocity \mathbf{u}_x , the local value of A changes. Similarly, the material derivative can also be defined with respect to a (curvilinear) coordinate system that moves with velocity $\dot{\mathbf{x}}$. For the scalar quantity A this becomes:

$$\frac{DA}{Dt} = \frac{\partial A}{\partial \tau} + \mathbf{u}_\xi \cdot \nabla A, \quad (\text{A.32})$$

where the first part again represents the local rate of change, only now at a fixed position in the transformed space. Figure A.4 shows the relation between \mathbf{u}_x and \mathbf{u}_ξ . Shown are a particle P and an iso-line ξ_0^1 at two different time instances, i.e., at t and $t + dt$ respectively. Initially the particle P coincides with the origin of the curvilinear coordinate system, i.e., $\xi^1 = 0$ and $\xi^2 = 0$. A short time later, the curvilinear coordinate system has traveled with velocity $\dot{\mathbf{x}}$ to a different position than the particle P did. Particle P has moved from $\mathbf{x}(t)$ to $\mathbf{x}(t + dt)$ with velocity \mathbf{u}_x . This means that the velocity of particle P with respect to the moving coordinate system, can be written as follows:

$$\mathbf{u}_\xi = \mathbf{u}_x - \dot{\mathbf{x}}. \quad (\text{A.33})$$

Combining the right-hand-sides of equations (A.31) and (A.32) with equation (A.33), leads to the following relation between the time-derivative in Cartesian space and the time derivative in transformed space:

$$\frac{\partial A}{\partial t} = \frac{\partial A}{\partial \tau} - \dot{\mathbf{x}} \cdot \nabla A, \quad (\text{A.34})$$

where $\dot{\mathbf{x}} \cdot \nabla A$, can be written as:

$$\begin{aligned} \dot{\mathbf{x}} \cdot \nabla A &= \dot{\mathbf{x}} \cdot \frac{1}{\sqrt{g}} \sum_{i=1}^3 [(\mathbf{a}_j \times \mathbf{a}_k) A]_{\xi^i}, \\ &= \frac{1}{\sqrt{g}} \sum_{i=1}^3 [(\mathbf{a}_j \times \mathbf{a}_k) \cdot \dot{\mathbf{x}} A]_{\xi^i} - A \frac{1}{\sqrt{g}} \sum_{i=1}^3 [(\mathbf{a}_j \times \mathbf{a}_k) \cdot \dot{\mathbf{x}}]_{\xi^i}, \quad (i, j, k) \text{ cyclic.} \end{aligned} \quad (\text{A.35})$$

Using (A.30), equation (A.35) reduces to:

$$\dot{\mathbf{x}} \cdot \nabla A = \frac{1}{\sqrt{g}} \sum_{i=1}^3 [(\mathbf{a}_j \times \mathbf{a}_k) \cdot \dot{\mathbf{x}} A]_{\xi^i} - A \frac{1}{\sqrt{g}} \sum_{i=1}^3 (\mathbf{a}_j \times \mathbf{a}_k) \cdot \dot{\mathbf{x}}_{\xi^i}. \quad (\text{A.36})$$

Following (A.4), $\dot{\mathbf{x}}_{\xi^i}$ of the last term of equation (A.36) becomes:

$$\dot{\mathbf{x}}_{\xi^i} = [x_{\xi^i}]_t = [\mathbf{a}_i]_t, \quad (\text{A.37})$$

where $[\dots]_t$ indicates the derivative with respect to t . This leads to:

$$\begin{aligned} \dot{\mathbf{x}} \cdot \nabla A &= \frac{1}{\sqrt{g}} \sum_{i=1}^3 [(\mathbf{a}_j \times \mathbf{a}_k) \cdot \dot{\mathbf{x}} A]_{\xi^i} - A \frac{1}{\sqrt{g}} \sum_{i=1}^3 (\mathbf{a}_j \times \mathbf{a}_k) \cdot [\mathbf{a}_i]_t \cdot \\ &\quad (i = 1, 2, 3), (i, j, k), \text{ cyclic} \end{aligned} \quad (\text{A.38})$$

Furthermore, taking the time derivative of equation (A.23), leads to:

$$\begin{aligned} [\sqrt{g}]_t &= [\mathbf{a}_1 \cdot (\mathbf{a}_2 \times \mathbf{a}_3)]_t, \\ &= [\mathbf{a}_1]_t \cdot (\mathbf{a}_2 \times \mathbf{a}_3) + \mathbf{a}_1 \cdot ([\mathbf{a}_2]_t \times \mathbf{a}_3) + \mathbf{a}_1 \cdot (\mathbf{a}_2 \times [\mathbf{a}_3]_t), \\ &= [\mathbf{a}_1]_t \cdot (\mathbf{a}_2 \times \mathbf{a}_3) + [\mathbf{a}_2]_t \cdot (\mathbf{a}_3 \times \mathbf{a}_1) + [\mathbf{a}_3]_t \cdot (\mathbf{a}_1 \times \mathbf{a}_2), \end{aligned} \quad (\text{A.39})$$

where the following vector identity has been applied:

$$\mathbf{A} \cdot (\mathbf{B} \times \mathbf{C}) = \mathbf{B} \cdot (\mathbf{C} \times \mathbf{A}) = \mathbf{C} \cdot (\mathbf{A} \times \mathbf{B}). \quad (\text{A.40})$$

Finally:

$$\begin{aligned} [\sqrt{g}]_t &= [\mathbf{a}_1]_t \cdot (\mathbf{a}_2 \times \mathbf{a}_3) + [\mathbf{a}_2]_t \cdot (\mathbf{a}_3 \times \mathbf{a}_1) + [\mathbf{a}_3]_t \cdot (\mathbf{a}_1 \times \mathbf{a}_2), \\ &= \sum_{i=1}^3 (\mathbf{a}_j \times \mathbf{a}_k) \cdot [\mathbf{a}_i]_t, \quad (i, j, k) \text{ cyclic}, \end{aligned} \quad (\text{A.41})$$

which is equal to the last term of (A.38), so that equation (A.34), can now be written as:

$$\frac{\partial A}{\partial t} = \frac{\partial A}{\partial \tau} - \frac{1}{\sqrt{g}} \sum_{i=1}^3 [(\mathbf{a}_j \times \mathbf{a}_k) \cdot \dot{\mathbf{x}} A]_{\xi^i} + A \frac{[\sqrt{g}]_t}{\sqrt{g}}. \quad (\text{A.42})$$

Note that it might be easier to use (A.34) directly, instead of (A.42).

A.2.2 Relation between covariant and contravariant basis vectors

When (A.28) is applied to ξ^m , this leads to:

$$\begin{aligned} \nabla \xi^m &= \frac{1}{\sqrt{g}} \sum_{i=1}^3 [(\mathbf{a}_j \times \mathbf{a}_k) \xi^m]_{\xi^i}, \\ &= \frac{1}{\sqrt{g}} \sum_{i=1}^3 (\mathbf{a}_j \times \mathbf{a}_k) \frac{\partial \xi^m}{\partial \xi^i}, \end{aligned} \quad (\text{A.43})$$

where (A.30) was again applied. Because the three curvilinear coordinates are independent, $\frac{\partial \xi^m}{\partial \xi^i}$ can be replaced by δ_m^i , leading to:

$$\nabla \xi^i = \mathbf{a}^i = \frac{1}{\sqrt{g}} (\mathbf{a}_j \times \mathbf{a}_k), \quad (i = 1, 2, 3), (i, j, k) \text{ cyclic}, \quad (\text{A.44})$$

which can be used to relate the covariant basis vectors to the contravariant basis vectors. The identity (A.30) can now also be written as:

$$\sum_{i=1}^3 \left[\sqrt{g} a^i \right]_{\xi^i} = 0. \quad (\text{A.45})$$

A.2.3 Derivative operators

Using the Einstein summation convention, the transformed derivative operators can finally be written as:

$$\nabla A = a^i A_{\xi^i}, \quad (\text{A.46})$$

$$\nabla \cdot \mathbf{u} = \frac{1}{\sqrt{g}} \left[\sqrt{g} u^i \right]_{\xi^i}, \quad u^i = a^i \cdot \mathbf{u}, \quad (\text{A.47})$$

$$\nabla \cdot (b \nabla A) = \frac{1}{\sqrt{g}} \left[b \sqrt{g} g^{ij} A_{\xi^j} \right]_{\xi^i}, \quad (\text{A.48})$$

$$\frac{\partial A}{\partial t} = \frac{\partial A}{\partial \tau} - \dot{\mathbf{x}} \cdot \nabla A. \quad (\text{A.49})$$

Physical interpretation of the mass consumption rate

In equations (2.39)-(2.42), the mass consumption rate m was introduced as $m = \rho U$, where U is the absolute value of the relative displacement velocity of the flame \mathbf{U} . In the case of a premixed flame, \mathbf{U} is equal to the so-called laminar burning velocity $S_L \mathbf{n}$. It is generally associated with the velocity at which a premixed flame will propagate into the unburnt mixture when the fluid velocity is absent. Figure B.1 shows an example of a flat, premixed flame. The unburnt mixture, which consists of fuel and oxidizer, flows out of a tube, with velocity u_1 . The flame front velocity v_f is equal to zero, which means that the burning velocity $S_L \mathbf{n}$ is exactly compensating the flow velocity u_1 . This can be seen in figure B.1. The laminar burning velocity is also a measure of the amount of fuel and oxidizer that is converted into products, by means of the mass consumption rate, which is defined as $m = \rho S_L$.

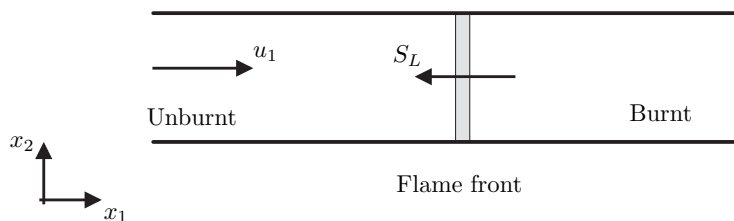


Figure B.1: Premixed flame.

Analogous to premixed flames, for non-premixed flames, the mass consumption rate $m = \rho U$ can be considered to represent the amount of mass per unit area that is converted by the flame each second. Figure B.2 shows a two-dimensional counterflow geometry, where two streams are shown, stream 1 consists of fuel and stream 2 consists of oxidizer. The two streams are separated by the stagnation surface. The x_1 and x_2 -components of the velocity vectors \mathbf{u} are shown as well as U . As can be seen, the

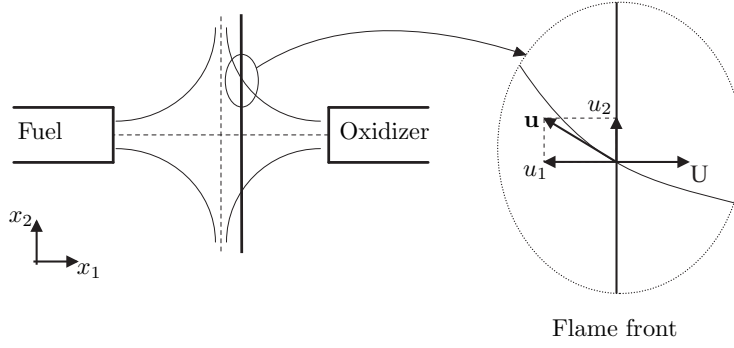


Figure B.2: Counterflow diffusion flame.

x_2 -component, u_2 accounts for the local stretch and since the flame-surface velocity v_f is zero, the x_1 -component, u_1 is balanced by the relative displacement velocity U . Even though a non-premixed flame does not propagate into the mixture, and thus it does not have a burning velocity, the mass consumption rate can be considered to represent the amount of mass per unit area that is converted by the flame each second. Due to the counterflow geometry, there exists a local stretch rate that can be considered as a negative source-term, as can be seen in equations (2.39)-(2.42). This means that the mass consumption rate is not only dependent on the local composition and enthalpy (through the chemical source-term), but it also depends strongly on the local stretching of the flow. This becomes also clear when (2.41) is integrated through the flame. For the fuel in a steady flame this becomes:

$$m_{F,1} = - \int_{-L}^L (\dot{\omega}_F - \rho K_M Y_F) dx_1, \quad (\text{B.1})$$

where the subscript $F, 1$ indicates the fuel present in stream 1. Note that $m_{F,2} = 0$, because $Y_{F,2} = 0$, i.e., stream 2 only contains oxidizer and no fuel at all. The contribution due to diffusion disappears because the computational domain is chosen such that all gradients are equal to zero on the boundaries. This means that the amount of mass of the fuel $m_{F,1} = m Y_{F,1}$ that enters the domain through the inlet at $x_1 = -L$, is partially converted into products and partially it leaks away due to flame stretching. The mass consumption rate can now be defined as follows:

$$m = \frac{1}{Y_{F,1}} \int_{-L}^L (\dot{\omega}_F - \rho K_M Y_F) dx_1. \quad (\text{B.2})$$

Individual contributions of the species conservation equation

The individual contributions $T_{n,i}$ are computed in a postprocessing step. Instead of actually computing the various derivatives of equations (3.2)-(3.5) with respect to the transformed coordinate system, the curvilinear derivatives are reformulated in terms of the Cartesian coordinates, by applying the chain-rule as follows:

$$\frac{\partial A}{\partial \xi^i} = \frac{\partial x_j}{\partial \xi^i} \frac{\partial A}{\partial x_j} = a_i \cdot \frac{\partial A}{\partial \mathbf{x}}. \quad (\text{C.1})$$

The normal transport contribution $T_{n,1}$ is rather straightforward and can be reformulated as:

$$T_{n,1} = -\mathbf{e}_1 \cdot \frac{\partial}{\partial \mathbf{x}} \left(mY_n - \rho D_n \mathbf{e}_1 \cdot \frac{\partial Y_n}{\partial \mathbf{x}} \right). \quad (\text{C.2})$$

In order to reformulate the stretch rate contribution, (2.39) is used, which results in:

$$T_{n,2} = -m\kappa Y_n + \mathbf{e}_1 \cdot \frac{\partial m}{\partial \mathbf{x}} Y_n. \quad (\text{C.3})$$

The curvature contribution is again fairly straightforward:

$$T_{n,3} = \left(mY_n - \rho D_n \mathbf{e}_1 \cdot \frac{\partial Y_n}{\partial \mathbf{x}} \right) \kappa. \quad (\text{C.4})$$

Reformulating the tangential diffusion term (2.43) requires a few more steps. The components of the contravariant metric tensor are given by (A.8), which means that:

$$g^{22} = \mathbf{a}^2 \cdot \mathbf{a}^2 = \frac{1}{h_{\xi^2}^2} \mathbf{e}_2 \cdot \mathbf{e}_2 = \frac{1}{h_{\xi^2}^2}. \quad (\text{C.5})$$

This means that (2.43) can be written as:

$$T_{n,4} = \frac{1}{h_{\xi^1} h_{\xi^2}} \frac{\partial}{\partial \xi^2} \left(\rho D_n h_{\xi^1} h_{\xi^2} \frac{1}{h_{\xi^2}^2} \frac{\partial Y_n}{\partial \xi^2} \right), \quad (\text{C.6})$$

and subsequently as:

$$T_{n,4} = \rho D_n \frac{1}{h_{\xi^2}} \frac{\partial Y_n}{\partial \xi^2} \frac{1}{h_{\xi^1} h_{\xi^2}} \frac{\partial h_{\xi^1}}{\partial \xi^2} + \frac{1}{h_{\xi^2}} \frac{\partial}{\partial \xi^2} \left(\rho D_n \frac{1}{h_{\xi^2}} \frac{\partial Y_n}{\partial \xi^2} \right). \quad (\text{C.7})$$

Analogous to the normal vector \mathbf{n} a tangential vector \mathbf{t} is defined as follows:

$$\mathbf{t} = -\frac{\mathbf{a}^2}{|\mathbf{a}^2|}. \quad (\text{C.8})$$

The divergence of the tangential vector $\nabla \cdot \mathbf{t}$ can be considered as a curvature contribution due to local variations in flame front thickness [55] and it can be shown that the following holds as well:

$$\nabla \cdot \mathbf{t} = -\frac{1}{h_{\xi^1}} \frac{\partial h_{\xi^1}}{h_{\xi^2} \partial \xi^2}, \quad (\text{C.9})$$

which finally leads to:

$$T_{n,4} = \mathbf{e}_2 \cdot \frac{\partial}{\partial \mathbf{x}} \left(\rho D_n \mathbf{e}_2 \cdot \frac{\partial Y_n}{\partial \mathbf{x}} \right) - \rho D_n \mathbf{e}_2 \cdot \frac{\partial Y_n}{\partial \mathbf{x}} \nabla \cdot \mathbf{t}, \quad (\text{C.10})$$

where (C.1) was also applied. This means that the individual contributions $T_{n,i}$ can be written as follows:

$$T_{n,1} = -\mathbf{e}_1 \cdot \frac{\partial}{\partial \mathbf{x}} \left(m Y_n - \rho D_n \mathbf{e}_1 \cdot \frac{\partial Y_n}{\partial \mathbf{x}} \right), \quad (\text{C.11})$$

$$T_{n,2} = -m \kappa Y_n + \mathbf{e}_1 \cdot \frac{\partial m}{\partial \mathbf{x}} Y_n, \quad (\text{C.12})$$

$$T_{n,3} = \left(m Y_n - \rho D_n \mathbf{e}_1 \cdot \frac{\partial Y_n}{\partial \mathbf{x}} \right) \kappa, \quad (\text{C.13})$$

$$T_{n,4} = \mathbf{e}_2 \cdot \frac{\partial}{\partial \mathbf{x}} \left(\rho D_n \mathbf{e}_2 \cdot \frac{\partial Y_n}{\partial \mathbf{x}} \right) - \rho D_n \mathbf{e}_2 \cdot \frac{\partial Y_n}{\partial \mathbf{x}} \nabla \cdot \mathbf{t}, \quad (\text{C.14})$$

$$T_{n,5} = \dot{\omega}_n^+, \quad (\text{C.15})$$

$$T_{n,6} = \dot{\omega}_n^-, \quad (\text{C.16})$$

Similarly, the mass consumption rate m is also reformulated. First, by recognizing that:

$$|\nabla \mathcal{Y}| = |\nabla \mathbf{a}^1| = \frac{1}{h_{\xi^1}}, \quad (\text{C.17})$$

and by applying (2.22), equation (2.11) is written as follows:

$$m = \rho U = h_{\xi^1} \dot{\omega}_y + h_{\xi^1} \frac{1}{\sqrt{g}} \frac{\partial}{\partial \xi^1} \left(\rho D_y \sqrt{g} g^{11} \frac{\partial \mathcal{Y}}{\partial \xi^1} \right). \quad (\text{C.18})$$

The components of the contravariant metric tensor are given by (A.8), which means that:

$$g^{11} = \mathbf{a}^1 \cdot \mathbf{a}^1 = \frac{1}{h_{\xi^1}^2} \mathbf{e}_1 \cdot \mathbf{e}_1 = \frac{1}{h_{\xi^1}^2}, \quad (\text{C.19})$$

which means that (C.18) can be written as:

$$m = h_{\xi^1} \dot{\omega}_y + \frac{1}{h_{\xi^2}} \frac{\partial}{\partial \xi^1} (\rho D_y h_{\xi^2} |\nabla \mathcal{Y}|), \quad (\text{C.20})$$

where (C.17) was also used to substitute the reciprocal of h_{ξ^1} with $|\nabla \mathcal{Y}|$. This subsequently leads to:

$$m = h_{\xi^1} \dot{\omega}_y + \rho D_y \frac{1}{h_{\xi^2}} \frac{\partial h_{\xi^2}}{h_{\xi^1} \partial \xi^1} + \frac{\partial}{\partial \xi^1} (\rho D_y |\nabla \mathcal{Y}|), \quad (\text{C.21})$$

where (C.17) was again used to substitute $|\nabla \mathcal{Y}|$ with the reciprocal of h_{ξ^1} . Finally using (2.32) and (3.8) leads to¹:

$$m = h_{\xi^1} \dot{\omega}_y - \rho D_y \kappa + h_{\xi^1} \mathbf{e}_1 \cdot \frac{\partial}{\partial \mathbf{x}} (\rho D_y |\nabla \mathcal{Y}|). \quad (\text{C.22})$$

¹Note that:

$$\kappa = -\frac{1}{\sigma} \frac{\partial \sigma}{\partial s} = -\frac{1}{h_{\xi^2}} \frac{\partial h_{\xi^2}}{h_{\xi^1} \partial \xi^1}.$$

Non-premixed reacting mixing Layer - simulation and reaction rate parameters

The various parameters that characterize the flow are listed in table D.1.

Table D.1: The simulation parameters that characterize the flow.

Parameter	Value		Parameter	Value	
Pr	0.72	–	ρ_∞	1.2	kg m ⁻³
Re _δ	0.50	–	p_∞	5.16×10^5	N m ⁻²
Ma	0.20	–	μ_∞	5.26×10^{-5}	kg m ⁻¹ s ⁻¹
T _∞	1500	K	U _∞	155.27	m s ⁻¹

The fuel consumption is computed by way of the following Arrhenius-type expression:

$$\dot{\omega}_{\text{CH}_4} = -A\rho^{\alpha+\beta}Y_{\text{CH}_4}^\alpha Y_{\text{O}_2}^\beta \exp\left(-\frac{E_a}{RT}\right), \quad (\text{D.1})$$

where the reaction rate parameters are chosen to be the same as in [7] and are listed in table D.2. Since there is only one reaction involved, it is clear that there is also only one chemical time-scale. This means that the production and consumption rates of all species involved are closely related to each other. In this context, the production and consumption rates of the other species are related to the fuel consumption rate as follows:

$$\dot{\omega}_n = \pm \nu_n \dot{\omega}_{\text{CH}_4} \frac{M_n}{M_{\text{CH}_4}}, \quad (\text{D.2})$$

with ν_n the stoichiometric coefficients of the global reaction, as given by equation (3.29).

Table D.2: The reaction rate parameters as taken from [7].

Parameter	Value	
A	4.3×10^{14}	$\text{m}^6 \text{kg}^{-2} \text{s}^{-1}$
E_a	210×10^3	J mole^{-1}
α	1	—
β	2	—

References

- [1] Andrews, G. E., Bradley, D. The burning velocity of methane-air mixtures. *Combust. Flame*, 19:275–288, 1972.
- [2] Barlow, R. S., Chen, J.-Y. On transient flamelets and their relationship to turbulent methane-air jet flames. *Proc. Combust. Inst.*, 24:231–237, 1992.
- [3] Barlow, R. S., Frank, J. H. Effects of turbulence on species mass fractions in methane/air jet flames. *Proc. Combust. Inst.*, 27:1087–1095, 1998.
- [4] Barths, H., Peters, N., Brehm, N., Mack, A., Pfitzner, M., Smiljanovski, V. Simulation of pollutant formation in a gas-turbine combustor using unsteady flamelets. *Proc. Combust. Inst.*, 27:1841–1847, 1998.
- [5] Barths, H., Pitsch, H., Peters, N. 3D simulation of DI diesel combustion and pollutant formation using a two-component reference fuel. *Oil & Gas Sci. Technol.*, 54:233–244, 1999.
- [6] Bastiaans, R. J. M., Somers, L. M. T., de Lange, H. C. DNS of non-premixed combustion in a compressible mixing layer. *Ercoftac Bull.*, 48:43–46, 2001.
- [7] Bédard, B., Egolfopoulos, F. N., Poinsot, T. J. Direct numerical simulation of heat release and NO_x formation in turbulent non-premixed flames. *Combust. Flame*, 119:69–83, 1999.
- [8] Bennett, B. A. V., McEnally, C. S., Pfefferle, L. D., Smooke, M. D. Computational and experimental study of axisymmetric coflow partially premixed methane/air flames. *Combust. Flame*, 123:522–546, 2000.
- [9] Bilger, R. W. The structure of turbulent non-premixed flames. *Proc. Combust. Inst.*, 22:475–488, 1988.
- [10] Bongers, H. *Analysis of flamelet-based methods to reduce chemical kinetics in flame computations*. PhD thesis, Eindhoven University of Technology, <http://www.combustion.tue.nl>, 2005.
- [11] Bongers, H., van Oijen, J. A., Somers, L. M. T., de Goey, L. P. H. The Flamelet-Generated Manifolds method applied to steady planar partially premixed counterflow flames. *Combust. Sci. Technol.*, 177:2373–2393, 2005.
- [12] Bowman, C. T., Hanson, R. K., Davidson, D. F., Gardiner Jr., W. C., Lissianski, V., Smith, G. P., Golden, D. M., Frenklach, M., Goldenberg, M. www.me.berkeley.edu/gri_mech/.
- [13] Bykov, V., Maas, U. The extension of the ILDM concept to reaction-diffusion manifolds. *Combust. Theory and Modelling*, 11:839–862, 2007.

- [14] CHEM1D. *a package for the simulation of one-dimensional flames*. Eindhoven University of Technology, 2002. <http://www.combustion.tue.nl>.
- [15] Chen, J.-Y., Liu, Y., Rogg, B. CO-H₂-N₂/air flames: Thermal radiation and transient effects. In Peters, N., Rogg, B., editors, *Reduced Kinetic Mechanisms for Application in Combustion Systems*, pages 196–223. Springer-Verlag, Berlin, 1993.
- [16] Christo, F. C., Masri, A. R., Nebot, E. M. Artificial neural network implementation of chemistry with PDF simulation of H₂/CO₂ flames. *Combust. Flame*, 106:406–427, 1996.
- [17] Claramunt, K., Cònsul, R., Pérez-Segarra, C. D., Oliva, B. Multidimensional mathematical modeling and numerical investigation of co-flow partially premixed methane/air laminar flames. *Combust. Flame*, 137:444–457, 2004.
- [18] Cònsul, R., Oliva, A., Pérez-Segarra, C. D., de Goey, L. P. H. Analysis of the flamelet concept in numerical simulation of laminar partially premixed flame. *Combust. Flame*, 153:71–83, 2008.
- [19] Cònsul, R., Pérez-Segarra, C. D., Claramunt, K., Cadafalch, J., Oliva, A. Detailed numerical simulation of laminar flames by a parallel multiblock algorithm using loosely coupled computers. *Combust. Theory Modelling*, 7:525–544, 2003.
- [20] Coppens, F. H. V., De Ruyck, J., Konnov, A. A. Effects of hydrogen enrichment on adiabatic burning velocity and NO formation in methane + air flames. *Exp. Therm. Fluid Sci.*, 31:437–444, 2007.
- [21] Darabiha, N. Transient behaviour of laminar counterflow hydrogen-air diffusion flames with complex chemistry. *Combust. Sci. Technol.*, 86:163–181, 1992.
- [22] Delhaye, S., Somers, L. M. T., van Oijen, J. A., de Goey, L. P. H. Incorporating unsteady flow-effects in Flamelet-Generated Manifolds. *Combust. Flame*, 155:133–144, 2008. doi:10.1016/j.combustflame.2008.03.023.
- [23] Delhaye, S., Somers, L. M. T., van Oijen, J. A., de Goey, L. P. H. Incorporating unsteady flow-effects beyond the extinction limit in Flamelet-Generated Manifolds. *Proc. Combust. Inst.*, 32:1051–1058, 2009. doi:10.1016/j.proci.2008.06.111.
- [24] Donbar, J. M., Driscoll, J. F., Carter, C. D. Strain rates measured along the wrinkled flame contour within turbulent non-premixed jet flames. *Combust. Flame*, 125:1239–1257, 2001.
- [25] Dugger, G. L. Effect of initial mixture temperature on flame speed of methane-air, propane-air and ethylene-air mixtures. *NACA report of investigations 1061, Lewis Flight Propulsion Laboratory, Cleveland, Ohio*, 1952.
- [26] Echekki, T., Chen, J. H. Unsteady strain rate and curvature effects in turbulent premixed methane-air flames. *Combust. Flame*, 106:184–202, 1996.
- [27] Echekki, T., Chen, J. H. Analysis of the contribution of curvature to premixed flame propagation. *Combust. Flame*, 118:308–311, 1999.
- [28] Eggels, R. L. G. M., de Goey, L. P. H. Mathematically reduced reaction mechanisms applied to adiabatic flat hydrogen/air flames. *Combust. Flame*, 100:559–570, 1995.
- [29] Egolfopoulos, F. N., Campbell, C. S. Unsteady counterflowing strained diffusion flames: Diffusion-limited frequency response. *J. Fluid Mech.*, 318:1–29, 1996.
- [30] Fiorina, B., Baron, R., Gicquel, O., Thévenin, D., Carpentier, S., Darabiha, N. Modelling non-adiabatic partially premixed flames using Flame-Prolongation of ILDM. *Combust. Theory Modelling*, 7:449–470, 2003.
- [31] Fiorina, B., Gicquel, O., Vervisch, L., Carpentier, S., Darabiha, N. Approximating the chemical structure of partially premixed and diffusion counterflow flames using FPI flamelet tabulation. *Combust. Flame*, 140:147–160, 2005.

- [32] Gicquel, O., Darabiha, N., Thévenin, D. Laminar premixed hydrogen/air counterflow flame simulations using Flame-Propagation of ILDM with preferential diffusion. *Proc. Combust. Inst.*, 28:1901–1908, 2000.
- [33] de Goey, L. P. H., ten Thijsse Boonkkamp, J. H. M. A mass-based definition of flame stretch with finite thickness. *Combust. Sci. Technol.*, 122:399–405, 1997.
- [34] de Goey, L. P. H., ten Thijsse Boonkkamp, J. H. M. A flamelet description of premixed laminar flames and the relation with flame stretch. *Combust. Flame*, 119:253–271, 1999.
- [35] de Goey, L. P. H., ten Thijsse Boonkkamp, J. H. M. Mass burning rate of premixed stretched flames: Integral analysis versus large-activation-energy asymptotics. *J. Eng. Math*, 62:67–84, 2008.
- [36] Goldemberg, J. World energy assessment: Energy and the challenge of sustainability. *United Nations Development Programme*, 2000.
- [37] Groot, G. R. A. *Modelling of Propagating Spherical and Cylindrical Premixed Flames*. PhD thesis, Eindhoven University of Technology, <http://www.combustion.tue.nl>, 2004.
- [38] Hergart, C. A., Barths, H., Peters, N. Modeling the combustion in a small-bore diesel engine using a method based on representative interactive flamelets. *Paper No. SAE 1999-01-3550*, 1999.
- [39] Hergart, C. A., Barths, H., Peters, N. Using representative interactive flamelets in the three-dimensional modeling of diesel combustion including effects of heat transfer. *Tenth International Multidimensional Engine Modeling User's Group Meeting*, 2000.
- [40] Hollman, C., Gutheil, E. Modeling of turbulent spray diffusion flames including detailed chemistry. *Proc. Combust. Inst.*, 26:1731–1738, 1996.
- [41] Im, H. G., Chen, J. H., Chen, J.-Y. Chemical response of methane/air diffusion flames to unsteady strain rate. *Combust. Flame*, 118:204–212, 1999.
- [42] Kee, R., Miller, J. A structured approach to the computational modeling of chemical kinetics and molecular transport in flowing systems. *Springer Series in Chemical Physics*, 47:196, 1986.
- [43] Kistler, J. S., Sung, C. J., Kreutz, T. G., Law, C. K. Extinction of counterflow diffusion flames under velocity oscillations. *Proc. Combust. Inst.*, 26:113–120, 1996.
- [44] Konnov, A. A. *Detailed reaction mechanism for small hydrocarbons combustion. Release 0.4*, 1998. <http://homepages.vub.ac.be/~akonnov/>.
- [45] Kozachenko, L. S., Kuznetsov, I. L. Burning velocity in a turbulent stream of a homogeneous mixture. *Combustion Explosion and Shock Waves*, 1:31–34, 1965.
- [46] Kundu, P. K., Cohen, I. M. *Fluid Mechanics*. Academic Press, Inc., 1990.
- [47] Lam, S. H., Goussis, D. A. Conventional asymptotics and computational singular perturbation for simplified kinetics modeling. In Smooke, M. D., editor, *Reduced kinetic mechanisms for asymptotic approximations for methane-air flames*, Lecture Notes in Physics 384, pages 227–242. Springer-Verlag, Berlin, 1991.
- [48] Law, C. K. Dynamics of stretched flames. *Proc. Combust. Inst.*, 22:1381, 1988.
- [49] Lehtiniemi, H., Mauß, F., Balthasar, M., Magnusson, I. Using a progress variable approach to model diesel spray ignition with detailed chemistry. *ECCOMAS Thematic Conference on Computational Combustion, Lisbon, Portugal 2005*, 2005.
- [50] Lele, S. K. Compact finite difference schemes with spectral-like resolution. *J. Comp. Phys.*, 103:16–42, 1992.
- [51] Liew, S. K., Bray, K. N. C., Moss, J. B. A stretched laminar flamelet model of turbulent non-premixed combustion. *Combust. Flame*, 56:199–213, 1984.

- [52] Maas, U., Pope, S. B. Simplifying chemical kinetics: Intrinsic low-dimensional manifolds in composition space. *Combust. Flame*, 88:239–264, 1992.
- [53] Maas, U., Pope, S. B. Laminar flame calculations using simplified chemical kinetics based on intrinsic low-dimensional manifolds. *Proc. Combust. Inst.*, 117:685–708, 1994.
- [54] Majda, A., Lamb, K. Simplified equations for low mach number combustion with strong heat release. *The IMA Volumes in Mathematics and its Applications*, 35:167–211, 1991.
- [55] Mallens, R. M. M. *Stabilisation of Laminar Premixed Methane/Air Flames*. PhD thesis, Eindhoven University of Technology, <http://www.combustion.tue.nl>, 1996.
- [56] Markstein, G. H. *Nonsteady Flame Propagation*. Pergamon Press, 1964.
- [57] Mauß, F., Keller, D., Peters, N. A lagrangian simulation of flamelet extinction and re-ignition in turbulent jet diffusion flames. *Proc. Combust. Inst.*, 23:693–698, 1990.
- [58] Metghalchi, M., Keck, J. C. Laminar burning velocity of propane-air mixtures at high temperature and pressures. *Combust. Flame*, 38:143–154, 1980.
- [59] Moore, G. E. Cramming more components onto integrated circuits. *Electronics*, 38(8), 1965.
- [60] Muller, C. M., Breitbach, H., Peters, N. Partially premixed turbulent flame propagation in jet flames. *Proc. Combust. Inst.*, 25:1099–1106, 1994.
- [61] van Oijen, J. A. *Flamelet-Generated Manifolds: Development and Application to Premixed Laminar Flames*. PhD thesis, Eindhoven University of Technology, <http://www.combustion.tue.nl>, 2002.
- [62] van Oijen, J. A., Bastiaans, R. J. M., de Goey, L. P. H. Low-dimensional manifolds in direct numerical simulations of premixed turbulent flames. *Proc. Combust. Inst.*, 31:1377–1384, 2007.
- [63] van Oijen, J. A., Bastiaans, R. J. M., Groot, G. R. A., de Goey, L. P. H. Direct numerical simulations of premixed turbulent flames with reduced chemistry: Validation and flamelet analysis. *Flow, Turbulence and Combustion*, 75:67–84, 2005.
- [64] van Oijen, J. A., de Goey, L. P. H. Modelling of premixed laminar flames using Flamelet-Generated Manifolds. *Combust. Sci. Technol.*, 161:113–137, 2000.
- [65] van Oijen, J. A., de Goey, L. P. H. Modelling of premixed counterflow flames using the Flamelet-Generated Manifolds method. *Combust. Theory and Modelling*, 6:463–478, 2002.
- [66] van Oijen, J. A., de Goey, L. P. H. A numerical study of confined triple flames using a Flamelet-Generated Manifold. *Combust. Theory and Modelling*, 8:141–163, 2004.
- [67] van Oijen, J. A., Groot, G. R. A., Bastiaans, R. J. M., de Goey, L. P. H. A flamelet analysis of the burning velocity of premixed turbulent expanding flames. *Proc. Combust. Inst.*, 30:657–664, 2005.
- [68] van Oijen, J. A., Lammers, F. A., de Goey, L. P. H. Modeling of complex premixed burner systems by using Flamelet-Generated Manifolds. *Combust. Flame*, 127:2124–2134, 2001.
- [69] Peters, N. Laminar diffusion flamelet models in non-premixed turbulent combustion. *Prog. Energy Combust. Sci.*, 10:319–339, 1984.
- [70] Peters, N. Reducing mechanisms. In Smooke, M. D., editor, *Reduced kinetic mechanisms for asymptotic approximations for methane-air flames*, Lecture Notes in Physics 384, pages 48–85. Springer-Verlag, Berlin, 1991.
- [71] Peters, N. *Turbulent Combustion*. Cambridge University Press, 2000.

- [72] Piffaretti, S., Gass, J., Poulidakos, D. Transient flamelet modelling of diffusion and partially premixed flames. *ECCOMAS Thematic Conference on Computational Combustion, Lisbon, Portugal 2005*, 2005.
- [73] Pitsch, H. Unsteady flamelet modeling of differential diffusion in turbulent jet diffusion flames. *Combust. Flame*, 123:358–374, 2000.
- [74] Pitsch, H., Chen, M., Peters, N. Unsteady flamelet modeling of turbulent hydrogen-air diffusion flames. *Proc. Combust. Inst.*, 27:1057–1064, 1998.
- [75] Pitsch, H., Ihme, M. An unsteady / flamelet progress variable method for LES of non-premixed turbulent combustion. *AIAA Aerospace Sciences Meeting and Exhibit*, 2005.
- [76] Pitsch, H., Steiner, H. Scalar mixing and dissipation rate in large-eddy simulations of non-premixed turbulent combustion. *Proc. Combust. Inst.*, 28:41–49, 2000.
- [77] Poinso, T. J., Lele, S. K. Boundary conditions for direct simulations of compressible viscous flows. *J. Comp. Phys.*, 101:104–129, 1992.
- [78] Pope, S. B. Computationally efficient implementation of combustion chemistry using *in situ* adaptive tabulation. *Combust. Theory and Modelling*, 1:41–63, 1997.
- [79] Pope, S. B., Maas, U. Simplifying chemical kinetics: Trajectory-generated low-dimensional manifolds. *Technical Report FDA 93-11, Cornell University*, 1993.
- [80] Ren, Z., Pope, S. B., Vladimirov, A., Guckenheimer, J. M. The invariant constrained equilibrium edge preimage curve method for the dimension reduction of chemical kinetics. *J. Chem. Phys.*, 124:114111, 2006.
- [81] Ribert, G., Champion, M., Gicquel, O., Darabiha, N., Veynante, D. Modeling nonadiabatic turbulent premixed reactive flows including tabulated chemistry. *Combust. Flame*, 141:271–280, 2005.
- [82] Richter, H., Granata, S., Green, W. H., Howard, J. B. Detailed modeling of PAH and soot formation in a laminar premixed benzene/oxygen/argon low-pressure flame. *Proc. Combust. Inst.*, 30:1397–1405, 2005.
- [83] Singh, S., Powers, J. M., Paolucci, S. On slow manifolds of chemically reactive systems. *J. Chem. Phys.*, 117:1482–1496, 2002.
- [84] Smith, G. P., Golden, D. M., Frenklach, M., Moriarty, N. W., Eiteneer, B., Goldenberg, M., Bowman, C. T., Hanson, R. K., Song, S., Gardiner Jr., W. C., Lissianski, V. V., Qin, Z. www.me.berkeley.edu/gri_mech/.
- [85] Smooke, M. D., Giovangigli, V. Formulation of the premixed and non-premixed test problems. In Smooke, M. D., editor, *Reduced kinetic mechanisms for asymptotic approximations for methane-air flames*, Lecture Notes in Physics 384, pages 1–28. Springer-Verlag, Berlin, 1991.
- [86] Somers, L. M. T. *The Simulation of Flat Flames with Detailed and Reduced Chemical Models*. PhD thesis, Eindhoven University of Technology, <http://www.combustion.tue.nl>, 1994.
- [87] Stahl, G., Warnatz, J. Numerical investigation of time-dependent properties and extinction of strained methane- and propane-air flamelets. *Combust. Flame*, 85:285–299, 1991.
- [88] Tap, F. A., Hilbert, R., Thévenin, D., Veynante, D. A generalized flame surface density modeling approach for the auto-ignition of a turbulent non-premixed system. *Combust. Theory and Modelling*, 8:165–193, 2004.
- [89] Thompson, J. F., Warsi, Z. U. A., Mastin, C. W. *Numerical grid generation: foundations and applications*. Elsevier Science Publishing Co., Inc., 1985. also available online at: <http://www.hpc.msstate.edu/publications/gridbook/>.

-
- [90] Turányi, T. Parameterization of reaction mechanisms using orthonormal polynomials. *Comp. Chem.*, 18:45–54, 1994.
- [91] Vreman, A. W., Albrecht, B. A., van Oijen, J. A., de Goey, L. P. H., Bastiaans, R. J. M. Premixed and non-premixed generated manifolds in large-eddy simulations of sandia flame d and f. *Combust. Flame*, 153:394–416, 2008.
- [92] Vreman, B., Geurts, B., Kuerten, H. Large-eddy simulation of the turbulent mixing layer. *J. Fluid Mech.*, 339:357–390, 1997.
- [93] Williams, F. A. Turbulent combustion. In *The Mathematics of Combustion*, pages 97–131. Society for Industrial and Applied Mathematics, 1985.
- [94] Wray, A. A. Minimal storage time-advancement schemes for spectral methods. *Technical Report, NASA Ames Research Center*, 1990.

Dankwoord

En toen was het ineens klaar. Na (iets) meer dan 4 jaar hard werken, en soms wat minder hard (European Combustion Meeting 2007 in Chania), is mijn proefschrift gedrukt en wel. En dat niet alleen, maar ook nog eens goedgekeurd door een commissie van wijze heren. Dit alles was natuurlijk nooit mogelijk geweest zonder de steun van een aantal mensen die ik allemaal dank verschuldigd ben.

Allereerst wil ik mijn promotor Philip de Goey hartelijk danken voor het vertrouwen dat hij 4 jaar geleden in mij had om dit project tot een goed einde te brengen. Verder zijn de vele 'korte' niet-geplande discussies ("Philip, heb je even 5 minuutjes?") zeer waardevol en leuk geweest. Ik kan je vertellen dat het enthousiasme van Philip zeer aanstekelijk kan werken! Op de tweede plaats wil ik Bart Somers bedanken voor de goede begeleiding die hij me gegeven heeft. Zijn ontspannen en flexibele houding, zowel op professioneel als op persoonlijk vlak, zorgden voor een fijne samenwerking. Ook Jeroen van Oijen ben ik zeer dankbaar. Zijn toewijding kent volgens mij geen grenzen; Jeroen is altijd bereid geweest om me te helpen, ook al had hij eigenlijk (te) weinig tijd. Furthermore, I would like to thank professor Mattheij, professor Roekaerts and professor Thévenin for reading a draft of my thesis and supplying me with valuable comments and suggestions.

Verder wil ik alle mensen van de sectie bedanken voor de gezelligheid tijdens de lunches, borrels, sport-middagen, divisie-uitjes, vrijdagmiddag borrels. Daar bleef het echter niet bij; er was ook altijd wel tijd voor een praatje links en rechts op de gang. Ook wil ik mijn kamergenoot Joost bedanken voor de onvergetelijke jaren in ons 'aquarium'. De ontelbare discussies die we hebben gevoerd waren misschien niet altijd zinvol, maar wel altijd leuk. In het bijzonder wil ik Marjan bedanken voor de lieverd die ze is en natuurlijk ook voor alle activiteiten die ze samen met Martin georganiseerd heeft.

And last but certainly not least, wil ik mijn (schoon-) familie en vrienden bedanken. Vooral mijn ouders en mijn broer Roy voor de steun die ik altijd heb gekregen. Natuurlijk mag Sam niet in dit dankwoord ontbreken; hij geeft me zoveel lol en mooie momenten waardoor elke dag wel weer iets nieuws met zich meebrengt. En de aller-, allerlaatste speciale vermelding is voor mijn liefke Alice, die ik wil bedanken voor al haar steun en liefde.

Curriculum Vitae

- June 30th, 1978 : Born in Helmond, the Netherlands
- Aug. 1990 - June 1996 : Pre-university education (V.W.O.),
Jan van Brabant, Helmond
- Sept. 1996 - Jan. 1997 : Physics,
University Utrecht,
Department of Physics and Astronomy
- Sept. 1997 - June 2004 : Mechanical Engineering,
Eindhoven University of Technology,
Department of Mechanical Engineering,
M.Sc. degree (With Great Appreciation)
- Sept. 2004 - Sept. 2008 : Ph.D. student,
Eindhoven University of Technology,
Department of Mechanical Engineering,
Combustion Technology Group